

The author(s) shown below used Federal funds provided by the U.S. Department of Justice and prepared the following final report:

Document Title: Day and Night Real Time Signature Enhanced Crime Scene Survey Camera

Author(s): Milind Mahajan, Karen Zachery, Weiya Zhang, Andrew Brackley, Xindian Long

Document No.: 240693

Date Received: January 2013

Award Number: 2010-DN-BX-K144

This report has not been published by the U.S. Department of Justice. To provide better customer service, NCJRS has made this Federally-funded grant report available electronically.

Opinions or points of view expressed are those of the author(s) and do not necessarily reflect the official position or policies of the U.S. Department of Justice.

FINAL REPORT

Submitted to
U.S. Department of Justice
Danielle McLeod-Henning, Program Manager
General Forensics R&D Program
Office of Investigative and Forensic Sciences
National Institute of Justice

GRANT NO: 2010-DN-BX-K144

TS&I GO# 71357

DAY AND NIGHT REAL TIME SIGNATURE ENHANCED CRIME SCENE SURVEY CAMERA

Submitted by
Technical PI: Milind Mahajan
805-373-4888 (phone); 805-373-4105 (fax)
Email: mmahajan@teledyne.com

Contributors: Milind Mahajan, Karen Zachery, Weiya Zhang
Andrew Brackley, Xindian Long

Submission Date: August 4th, 2012

DUNS 96-795-3613
EIN 52-231-4487

Recipient Organization
Teledyne Scientific & Imaging, LLC
1049 Camino Dos Rios
Thousand Oaks, CA 91360

Grant Period: October 18th, 2010 - May 31th 2012

Reporting Period End Date: May 31st 2012
Report Term or Frequency: Final

Abstract

The goal of this work is to lay down the foundations of an integrated day and night forensic survey camera capable of real time enhancement of targets of forensic interest. The camera collects and analyzes different wavelength and polarization channels using multiple wavelength illumination, including ultraviolet (UV) for fluorescence.

Contrast enhancement techniques that use alternate light sources (ALS) with multiple wavelength filters, off-axis illumination for prints, and fluorescence imaging for bio-fluids, are powerful tools already in use by the forensic community. However the majority of current instruments and procedures require a darkened environment, and pose significant logistical challenges. Our concept of a stand-off multi-spectral camera combined with a compact strobed and gated illuminator can provide:

- 1) Multiple detection capabilities in a single camera system
- 2) Ability to operate in presence of ambient light
- 3) Ability to enhance detection using advanced image processing algorithms
- 4) Intuitive, nearly real time presentation of the results, overlaid on the scene imagery.

The results will be increased speed of crime scene investigation, and reduced contamination of crime scenes. It will assist planning and prioritization of further investigation, and significantly reduce labor-intensive non real-time image processing.

Under the currently funded proof-of-concept trade study, we fabricated a breadboard prototype imaging system using strictly commercial off-the-shelf (COTS) components. We tested and demonstrated the functionality in laboratory environment using simulated targets that would be of interest to forensic investigators (e.g. blood and saliva stains, latent prints, chemical stains, powder residue etc.) We refer to these markers as “targets” through this report. The illuminator unit of our breadboard has six different illumination channels (one UV, three visible and 2 near-infrared (NIR) set by emission bands of light emitting diodes (LEDs). For the camera unit, we employ a monochrome camera with a multi-spectral lens that can selectively image the targets within the pass-band of six spectral filters matched to LED wavelengths. We can also control the polarization of transmit and receive paths.

During the trade study, we acquired target images in different modes, namely multi-spectral, polarization, and fluorescence. We applied various contrast enhancement, filtering and image rendering algorithms to the collected imagery. Our contrast enhancement algorithms are inspired by biological principles of signal interaction in the retinal circuits. Our multispectral processing is similar to the techniques used for remote sensing surveys. We also applied frequency domain filtering in numerous cases. We often used false color rendering when needed to combine and present information in various imaging channels for human viewing.

We demonstrated contrast enhancement and improved detection threshold across a wide range of targets. In several cases, our camera was able to capture target imagery (e.g. prints, stains etc.) that was invisible to naked eye as well as conventional color digital camera. Adaptive dynamic range compression and false color rendering were effective in directing viewer’s attention to the enhanced target.

The report describes the hardware fabrication, presents the trade study results in detail, provides a description of various contrast enhancement algorithms, and recommends the path forward to a field portable brass board.

Table of Contents

Abstract	2
Table of Contents	3
Executive Summary	5
I. Introduction	7
I.1. Background	7
I.2. Research Rationale	8
II. Methods	8
II.1. Hardware Description	8
II.2. Hardware Integration	10
II.3. Experimental Procedure	11
III. Results	13
III.1. First Multi-spectral Images	13
III.2. Multispectral Analysis of Ink Samples	14
III.3. Multispectral Analysis of Blood Stains on Cloth	17
III.4. Evaporated Solvents	20
III.5. Imaging Latent Prints	21
III.6. Solvents that Leave Residue	24
III.7. Polarization Analysis of Prints	26
III.8. UV/Fluorescence Imaging of Blood Stains	27
III.9. UV/Fluorescence Imaging of Saliva	28
III.10. Soot Damaged Paper	30
III.11. Experiments in Outdoor Environment	31
IV. Description of Image Processing Algorithms	34
IV.1. Contrast Enhancement	34
IV.2. Color Opponent Processing	35
IV.3. Three Channel False Color	39
IV.4. Spectral Measurements	41
IV.4.1. TM14 and TM41	41
IV.4.2. ARVI and ASVI	42
IV.4.3. GEMI and MSAVI	43
IV.5. Multispectral Analysis	43
IV.5.1. Data Cube and Spectral Vectors	44
IV.5.2. Spectral Target Samples	44
IV.5.3. Anomaly Detection Algorithms	45
IV.5.3.1. Constrained Energy Minimization (CEM)	46
IV.5.3.2. Generalized Likelihood Ratio Test (GLRT)	46
IV.5.3.3. Adaptive Coherence Estimator (ACE)	47
IV.5.3.4. Hybrid Unstructured Detector (HUD)	48
IV.6. Frequency Subband Filtering	49
IV.7. Steerable Filter	53
IV.8. Fusion via Multi-scale, Multi-orientation Steerable Pyramid	56
IV.8.1. Steerable Pyramid	57
IV.8.2. Image Fusion	59
IV.9. Gabor Filter Based Fingerprint Enhancement	59
IV.10. Polarization Analysis	61

IV.10.1.	Stokes Parameter Images	61
IV.10.2.	Contrast Enhancement via Virtual Polarizer.....	62
IV.10.3.	Degree of Linear Polarization and Angle of Polarization.....	65
IV.11.	Contextual Rank Ordering.....	65
IV.11.1.	Rank Order Metric	66
IV.12.	A Note on Processing Platform Requirement.....	67
V.	LED Pulsed Illumination and Radiometric Considerations.....	68
V.1.	Optical Characteristics as Specified by the Manufacture.....	68
V.2.	Overdriving	68
V.3.	Typical Lighting Conditions	70
VI.	Conclusions.....	73
VII.	Dissemination of Research Findings	74
VIII.	References	75

Executive Summary

The forensic community employs numerous contrast enhancement techniques that use alternate light sources (ALS) with multiple wavelength filters, off-axis illumination for prints, and fluorescence imaging for bio-fluids. However, all of these techniques require a darkened environment, limiting the utility of the laborious and time consuming visualization methods and posing significant logistical challenges. Furthermore, there are scenarios where logistics (e.g. a closed highway) or available resources (e.g. crimes of less serious nature) restrict the amount of time spent by an expert at the crime scene. There is need for a camera that can collect and process information beyond what a conventional digital camera can do. There is a need for tools that can rapidly survey a crime scene and provide nearly real time (~1 second processing time, not video rate) information to help plan and prioritize the investigation. Under the grant from the Department of Justice, Teledyne Scientific and Imaging Company conducted a proof of concept trade study for such a camera and related software processes.

Recent advances and improving availability of high brightness LEDs spanning the entire UV through visible and NIR wavelength spectrum, sensitive monochrome cameras, multi-spectral lenses and tunable band-pass filters enable development of a single camera system with multiple detection capabilities. Background rejection is achieved through spectral filtering and temporal gating to enable operation in the presence of ambient light. Modern image processing and rendering algorithms allow the user to view multiple image modalities and exploit the results immediately in the field by making informed decisions on next steps.

The goal of this effort was to validate the concept at proof of concept level through an affordable hardware build based on integration of commercial off-the-shelf COTS components followed by a trade study on simulated targets. The issues of field portability and user interface were also not addressed at this stage.

The building blocks of the breadboard imaging system are a scientific grade, high dynamic range monochrome camera with a specialized lens that is in focus throughout the UV-Vis-NIR spectral range, COTS LEDs and strobe drivers, COTS bandpass filters mounted on a computer controlled filter wheel, polarizers, and a laptop computer. The hardware is compact though not field portable. Control software and a barebones graphical user interface are written in visual C++. We stored raw image files in 16 bit format and digital image processing and enhancements were performed using MATLAB.

The camera and controller electronics were laid out on a compact 2 feet by 3 feet optical breadboard. We mounted illuminator LEDs on an aluminum plate tethered to the controllers via long electrical cords to provide sufficient flexibility in varying the illumination and imaging geometry. We prepared various test articles of interest (simulated targets) and attached them against a black cloth as the background.

The targets analyzed include inks, chemicals, blood, saliva, latent prints. We imaged stains left behind by pure solvents (through texture changes on the substrate) as well as by solvents that leave behind a solid residue. The imaging modalities included multispectral, fluorescence and polarization imaging. We tested an array of contrast enhancement algorithms against collected imagery that exploit multi-spectral color, texture, and polarization signatures of the targets, and use adaptive dynamic range compression and false coloring to optimally render the (processed or unprocessed) images. Our contrast enhancement algorithms are inspired by biological principles of signal interaction in the retinal circuits. Our multispectral processing is analogous to the

techniques commonly used for remote sensing surveys. Texture enhancement is achieved using frequency domain filtering.

The breadboard camera collected a significantly greater amount of information than just the three color bands collected by a conventional digital camera. The breadboard camera could detect targets that were invisible to naked eye and color digital camera. In many cases where the targets were barely visible, certain wavelength channels of the breadboard captured it with significantly higher contrast. While hardware enhancements compared to a conventional color digital image were generally very obvious, the software enhancements when compared to the highest contrast channel of the breadboard at optimum brightness and contrast setting were often more subtle and related to finer detail like edges. The effect of adaptive dynamic range compression and false color rendering to direct viewer's attention to the target was substantial.

We also explored the radiometric considerations for a field portable camera system. We analyzed through measurements the ability to overdrive LEDs of different wavelengths. This overdrive factor is related to the material set that is used to design LEDs of a specific color. Among the tested units, the red (630 nm) LED showed the least capability of overdriving (~2.8X). The IR (740 nm and 870 nm) showed the greatest potential of overdriving, with no sign of leveling off even at 10X output. We compared the LED outputs with typical background measurements (performed using a calibrated radiometer) and found that with a single LED per wavelength it is possible to produce illumination comparable with direct sunlight (within filter pass band) at 2 m, and in shadow, that distance will extend to well beyond 5 meters. Using multiple LEDs (particularly at blue and green wavelengths) and using background subtraction, the breadboard camera range can be further extended. Actual performance limit is also dependent on target reflectivity and the imaging mode e.g., fluorescence mode has shorter range than multispectral mode.

The dissemination activities include a briefing at NIJ which was also attended by personnel from department of homeland security (DHS), and a teleconference (web based briefing) to Stockton police department. We participated in a panel presentation at 2012 NIJ conference and also presented a poster on the work. We plan to present at a later date in a suitable conference meeting in the field of optics/ optical engineering and forensic science.

Looking beyond the current proof of concept stage, we need to focus on size, weight and power considerations for a field portable unit. Hardware improvements will likely involve custom LED illumination optics, custom agile filter, and custom integrated hardware packaging. The testing so far has been in clutter free controlled laboratory setting, and extension of the trade study to cluttered environments similar to operational scenarios is required. Finally, a software user interface that maximizes the utility to the target end-user needs to be developed and tested.

The proposed concept can have an overreaching impact on the practice and policy of criminal justice, both at local and national level. It will fill the need for rapid crime scene scanning using multiple imaging channels to identify targets of interest. Furthermore, it will do so without restricting the first investigators on the scene to operate in a darkened environment. It will provide, in a small, rugged, affordable, and portable device, some of the extensive capability currently available primarily in the laboratory. This will result in enhanced documentation, and improved onsite presumptive analysis of forensic evidence at the crime scene. The non-labor-intensive capability to detect forensic evidence at standoff distance can also prevent evidence contamination.

Main Body of the Final Technical Report

I. Introduction

I.1. Background

Crime scene investigators are interested in detecting several types of evidence present at the scene e.g. body fluids, latent prints, chemical and drug stains, hair and fiber, gunshot residue, explosive residue, glass and metal shards and so on. These are often difficult to distinguish from the background and present a formidable challenge to detect and identify. There can be scenarios where the logistics (e.g. highway closed for accident investigation) or the available resources (e.g. crimes of low seriousness) restrict the amount of time spent by an expert at the crime scene. There is a need for tools that can rapidly survey a crime scene and provide real time information that will help plan and prioritize the investigation.

Digital single lens reflex (DSLR) cameras (e.g. Nikon D700, or Kodak 760) along with powerful image processing tools (e.g. Adobe Photoshop) have proven extremely valuable in the field [1]. However, a significant amount of manual post-processing work is required for image enhancement. Conventional DSLRs do not capture image signatures outside the visible spectrum. Recently, specialized monochrome forensic SLR cameras have become available for detection of ultra-violet (UV) and near infrared (NIR) wavelengths [2]. These are used in conjunction with various optical filters. NIR capability has been shown to be useful in enhancing the visibility of blood stains, document-forgery, and gunpowder residue [2,3].

Another tool popular among forensic investigators is the use of alternate light source (ALS). ALS are based on arc lamps [4], LEDs [5], or even lasers [6] typically used with a matching set of filters, or simply colored eyewear [4]. Imaging with an ALS is particularly sensitive to background illumination and requires a darkened environment. UV reflectance has been shown to be useful for fingerprint, bite mark, bruise, and shoeprint identification [7]. A large class of materials (e.g. body fluids) exhibits fluorescence, which is also exploited [8, 9].

Extreme oblique angle illumination with ALS is often used to examine light scattered by shoeprints, fingerprints etc. [10] Polarization signatures have also been shown to be useful in certain scenarios [11].

A review of the literature on established techniques and forensic products reveals some major operational deficiencies. Sunlight is an overwhelming interference for nearly all ALS imaging techniques and the resultant requirement of darkening the area imposes logistical constraints. There is a critical need for real time analysis that is not sensitive to ambient illumination and requiring minimal scene conditioning (e.g., use a screen to cast a shadow on the target). Specific imaging geometry requirements (e.g., extreme oblique incidence) are undesirable.

Furthermore, there is no single, integrated device that incorporates a multitude of these techniques. There is a lack of sensors that can survey a wide crime scene area in a short period of time while maintaining sufficient distance from the crime scene to minimize the potential for contamination of the scene. Finally, manual data collection with multiple sensors and laborious post processing in the lab, while extremely powerful, does not allow on the spot location, identification, or quantitative analysis.

I.2. Research Rationale

Recent advances and improving availability of high brightness LEDs spanning the entire UV through visible and NIR wavelength spectrum, sensitive monochrome cameras and tunable bandpass filters enable development of a single camera system with multiple detection capabilities. Background rejection through spectral filtering and temporal gating enables operation in the presence of ambient light. Modern image processing and rendering algorithms allow the user to view multiple image modalities and exploit the results immediately in the field by making informed decisions on next steps.

The focus of this effort was to validate the concept through an affordable hardware build based on integration of COTS components followed by a trade study on simulated targets. The issues of field portability and user interface were not addressed in this effort. The intent of this research is not to match performance of existing laboratory systems and techniques in every respect but to develop an easy to use field camera (in a multi-step process) that possesses a substantial fraction of current laboratory capabilities.

II. Methods

II.1. Hardware Description

The breadboard imaging system consists of a camera and electronics mounted on a 2' x 3' optical breadboard and a separate illuminator unit. Illuminator is an array of high brightness LEDs (with Fresnel optics to create a uniform spot) mounted to an aluminum base plate. This allows easy variation of imaging geometry e.g. on axis, and various degrees of off-axis illumination.

Camera: True monochrome SLRs are no longer easily available. We were left with two choices for the camera 1) An SLR with IR-UV cut filters removed by a third party vendor (RGB filters cannot be removed) or 2) a true scientific grade monochrome camera (no RGB filters). We selected a 2MP scientific grade camera from Point Grey research, Inc. (Grasshopper GRAS-20S4M) featuring 14 bit dynamic range, global shutter and an external trigger for ease of synchronization with the strobed illuminator. We used a familiar camera model with smaller number of pixels compared to a modern SLR for convenience (ease of integration, smaller amount of data to manage and process). The number of pixels does not impact the phenomenology or performance of algorithms. We later appreciated the benefits of using a large format camera for demonstration purposes as well as to cover substantially wider FOV with high resolution. We plan to upgrade to a 12 MP camera for future work.

Conventional lenses do not transmit well outside the visible band. They also need focus adjustment. Manual focus will disturb image capture and automatic focus between shots is time consuming. We selected CoastalOpt® UV-VIS-IR 60 mm lens from Jenoptic. This high performance lens eliminated the need to change image focus during imaging. The camera and lens combination provides 8.5° FOV, which is significantly smaller than the COTS illuminator FOV (~50°) producing acceptable uniformity of illumination.

We used 1" aperture 6 position motorized filter wheel from Thorlabs to select the receive wavelength for the camera. In a field portable device we will replace this by a tunable liquid crystal based band pass filter.

Illumination and Filters: The criteria for selection of illumination wavelengths were: 1) sufficient number of spectral samples across the UV through NIR spectrum with reasonable spacing between them, and 2) availability of COTS LEDs with optics to produce a uniform spot 3) Availability of matching COTS band pass filters.

We used LED illuminator modules from ProPhotonix, and selected optical band pass filters from Semrock, Inc. A high pass filter could be used for the longest wavelength of 870 nm since the quantum efficiency of a silicon based camera is negligible beyond 950 nm and background noise from wavelengths beyond 950 is insignificant. Figure 1 shows the measured LED emission spectra along with corresponding filter transmission. Since the intensity of short wavelength LEDs is less than the longer wavelength LEDs, we ultimately upgraded the system to two UV and Blue LEDs and one each for all the other wavelengths.

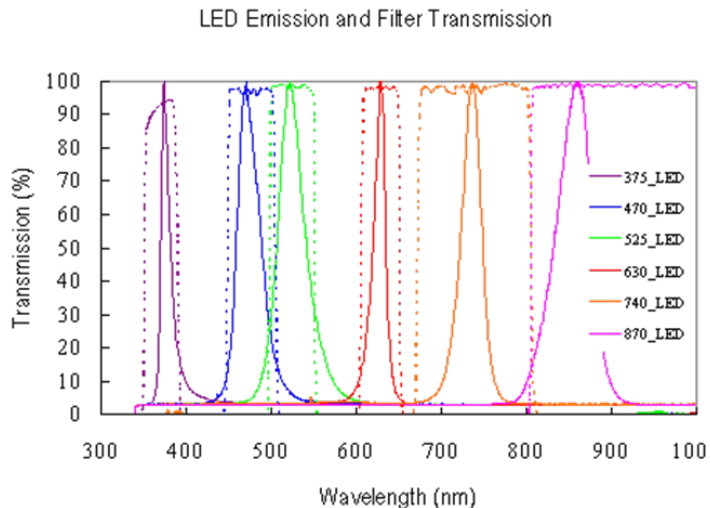


Figure 1 LED emission (solid lines) and filter transmission (dotted lines) spectra

The UV illumination is restricted to UV-A region which is known to cause minimal UV damage to DNA. When compared to the other sources of UV exposures in the field, including fluorescent lighting, sun, and “black lights” commonly used by forensic investigators, our approach results in negligible UV exposure. Table 1 shows summary of LED and filter characteristics.

Table 1 Summary of LED and filter characteristics

Channel	Wavelength (nm, nominal)	CW Illumination (W/m^2) at 0.25 m	Maximum overdrive factor in pulsed mode	LED bandwidth (nm)	Filter bandwidth (nm)
UV	375	13	4X	13	36
Blue	470	30	6X	25	55.7
Green	525	11	4.5X	34	50
Red	630	38	2.5X	15	46.5
NIR1	740	18	10X	27	137
NIR2	870	20	12X	31	150

II.2. Hardware Integration

We used a 24V, 240 W power supply from Stocker Yale and two four-channel LED strobe drivers from Gardasoft Visio, Ltd. We used a data acquisition (DAQ) module (miniLAB 1008) from Measurement Computing for trigger generation. This DAQ module has 28 two-way digital I/O lines that can be controlled through a USB port. A laptop computer was used to operate the illuminator and the camera in a synchronized fashion and to collect and store resultant imagery. The system layout is shown in Figure 2.

The control software and graphical user interface (GUI) are written in Visual C++ environment and uses libraries provided by different hardware vendors. The LED drive currents and exposure times are programmed into the strobe drivers via Ethernet. The software sends a string to the DAQ over USB to set up the appropriate trigger outputs. During acquisition, the software sets up the receive filter in place, and then commands the DAQ to simultaneously trigger the selected LED strobe, and the camera. The image data is received over an IEEE 1394

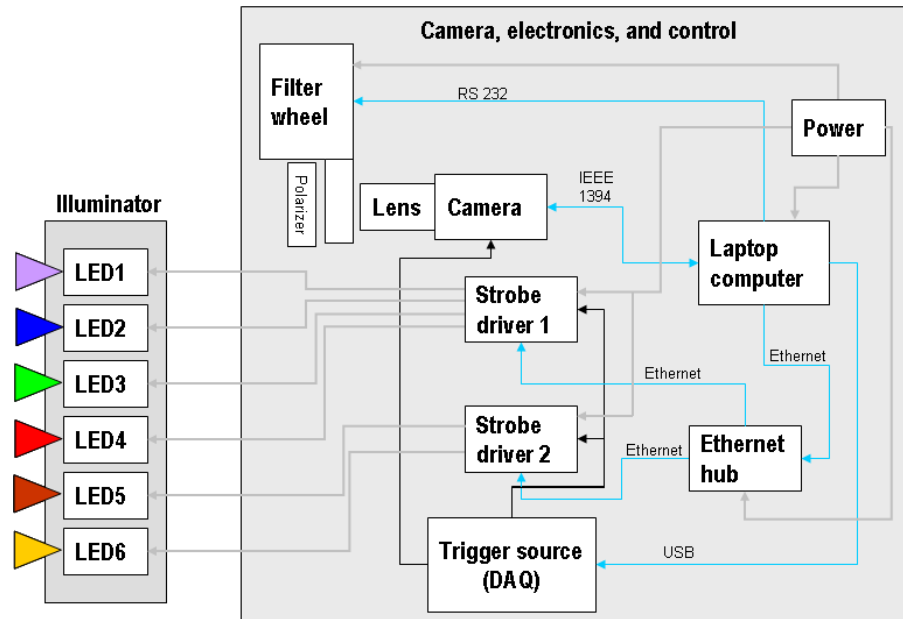


Figure 2 Breadboard imaging system components and interfaces

bus (Firewire) into the Laptop. A set of images can be acquired either manually or as a pre-selected sequence (“recipe”). For example a multi-spectral recipe will go through a sequential image acquisition where each LED and the corresponding band-pass filter are used. A fluorescence recipe will repeatedly illuminate with a single wavelength (typically UV, but longer wavelengths can be used) and sequentially acquire images at the same or longer receive wavelengths. Polarization control is currently through manual stages but can ultimately be controlled through TS&I’s agile liquid crystal based polarization controller for portability.

Figure 3 shows photographs of the breadboard camera system and the illuminator.

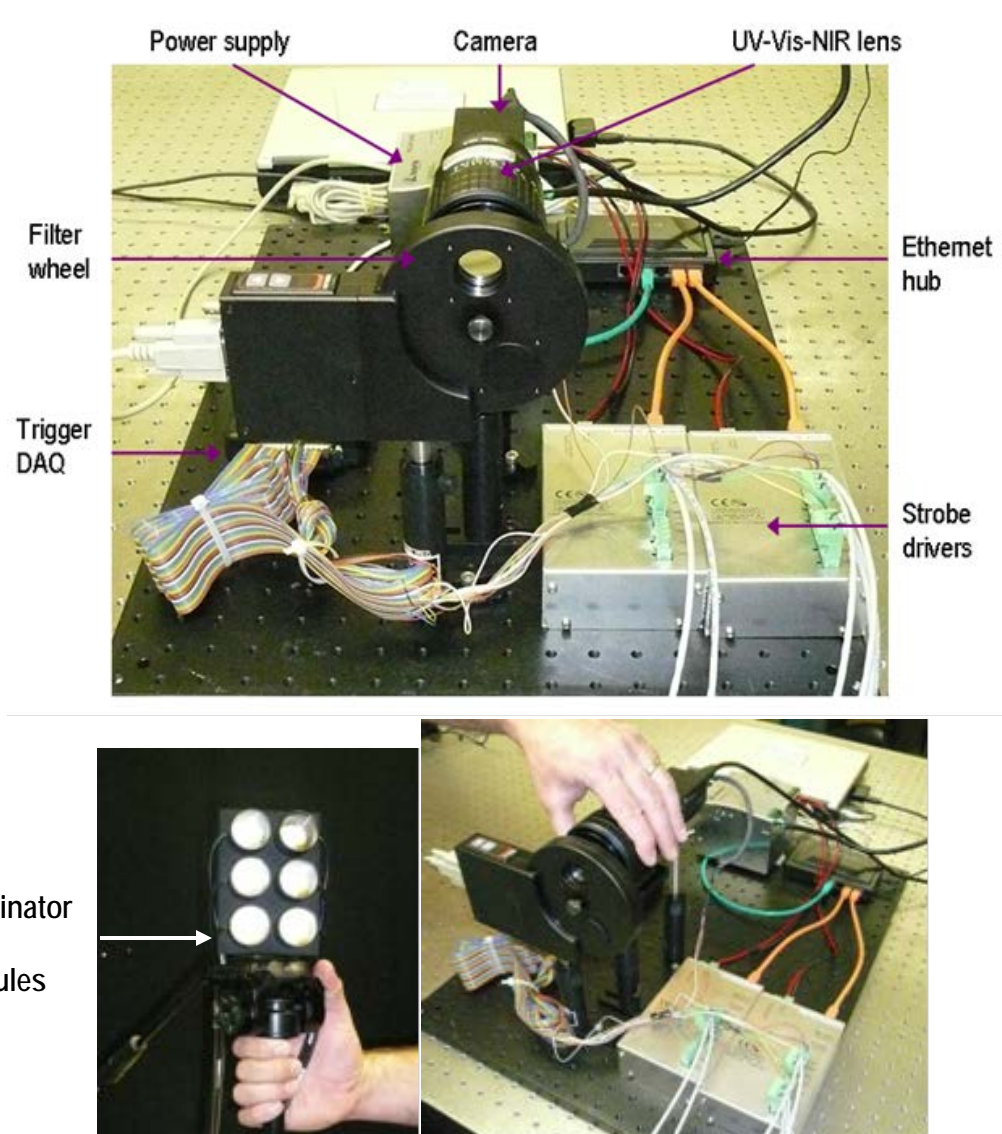


Figure 3 Breadboard imaging system: camera (top, bottom right) and illuminator (bottom left)

II.3.Experimental Procedure

We set up a test area in our laboratory, with the camera and controller electronics laid out on a compact optical breadboard. We mounted the illuminator LEDs on an aluminum plate tethered to the controllers via 3 meter long cords. This arrangement provided sufficient flexibility in varying the illumination angles. We prepared various test articles of interest (simulated targets) and placed them against a black cloth as the background.

In the following sections we present description for preparing the simulated targets, and document recipes for capturing breadboard camera imagery. Our presentation is chronological (the order in which we performed the experiments). We cover different classes of targets: document analysis (inks), latent prints, body fluids, and chemical residues (powder and stains).

The results are demonstrated with representative images from color digital image, raw single wavelength data, and algorithm enhanced and/or false color represented data. We summarize improvements in detection threshold and image contrast when compared with the naked eye or conventional color digital camera. For details on the enhancement algorithms we refer the reader to the next section, where we describe an array of digital enhancement and image rendering techniques, along with underlying mathematical expressions, illustrated with examples from the trade study experiments.

For the purpose of this report, we define multispectral mode as the procedure where we illuminate at all six wavelengths and acquire image using the bandpass filter corresponding to the illumination wavelength. We define UV/Fluorescence mode as the mode where we illuminate using 375 nm UV wavelength and image consecutively using bandpass filters at UV and the five longer wavelengths. In fluorescent mode when the illumination wavelength is the same as filter wavelength the received image is a mix of reflectance and fluorescence and likely to be dominated by reflectance. When the filter wavelength is different (longer) from the illumination wavelength, the signal is dominated by fluorescence. While, it is possible to acquire fluorescent images by illuminating with other LEDs, such variations were not performed.

In addition to laboratory imaging experiments, we examined blood and saliva samples in outdoors environment (clear day light, early afternoon with an open patio canopy providing makeshift shade). For outdoors experiments we captured images in both LED and background lighting and subtracted background from the LED lit images. There was sufficient light available in COTS illuminator for high SNR in multispectral mode. We integrated of multiple frames to improve SNR of the weaker fluorescent signal.

Table 2 shows a summary of targets and methods used for imaging and algorithm development and testing, along with conclusions.

Table 2 Summary of simulated targets, imaging methods, and conclusions

Targets	Methods	Conclusions
Latent prints on glossy surfaces viz. plastic and book cover	Multi-spectral, polarization	Ability to detect and capture "invisible" prints , successful in contrast enhancement, spectral signatures can detect trace material differences, additional enhancement can be achieved with polarization
Blood stains on red cloth, blue jeans	Multi-spectral, Fluorescence	Ability to detect "invisible" targets, successful in contrast enhancement, successfully tested indoors and outdoors
Solvents that leave residue viz. salt, pseudoephedrine	Multi-spectral	Ability to detect "invisible" targets, successful in contrast enhancement
Saliva stains on blue cloth	Multi-spectral, Fluorescence	Ability to detect "invisible" targets, successful in contrast enhancement, successfully tested indoors and outdoors
Inks, writing samples	Multi-spectral	Excellent ability to differentiate compositions, known, limited use in field, lab products are mature
Smoke damaged paper	Multi-spectral, fluorescence	Ability to read text underneath the soot deposits using NIR wavelengths, insufficient signal in fluorescent mode
Solvents that leave no residue	Multi-spectral	Texture analysis can greatly enhance contrast of target as well as background clutter, limited utility for detection

III. Results

III.1. First Multi-spectral Images

The first target comprised of red colored marks over red background. Three marks were created using red ink and the fourth was a stain of sterilized bovine blood. Figure 4 shows a color digital camera photograph of the target. The third ink mark (C-bottom right) appears completely blended with the background, and the blood spot has the similarly colored, but diluted appearance as the second ink mark (B). The top half of Figure 5 shows the target imaged in the second NIR channel and the red channel. The blood spot and two of the ink marks appear completely blended with the background.

The bottom half of Figure 5 shows the target images in blue and green channels. While these images do not show high reflectivity as evident from the grainy appearance, they contain the highest distinguishing features between the marks. For example the blood stain is visible in blue as well as green while the red mark (B) is visible in only the blue image. The mark (C) which was undetectable in either the conventional color photograph or the red and NIR channels, is easily detected in blue and green channels.

It is also interesting to note that two different black pens were used inadvertently to label the samples, and the multispectral images reveal that difference as well: One of the inks is invisible in blue and green images.

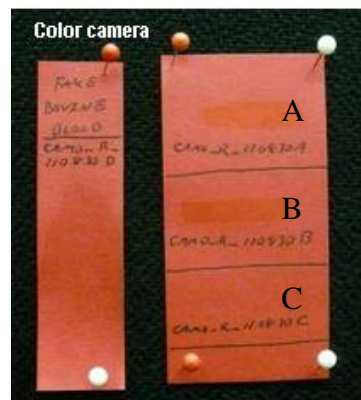


Figure 4 Red marks on red background

Left: bovine blood spot, Right: three different red ink spots (A,B,C)

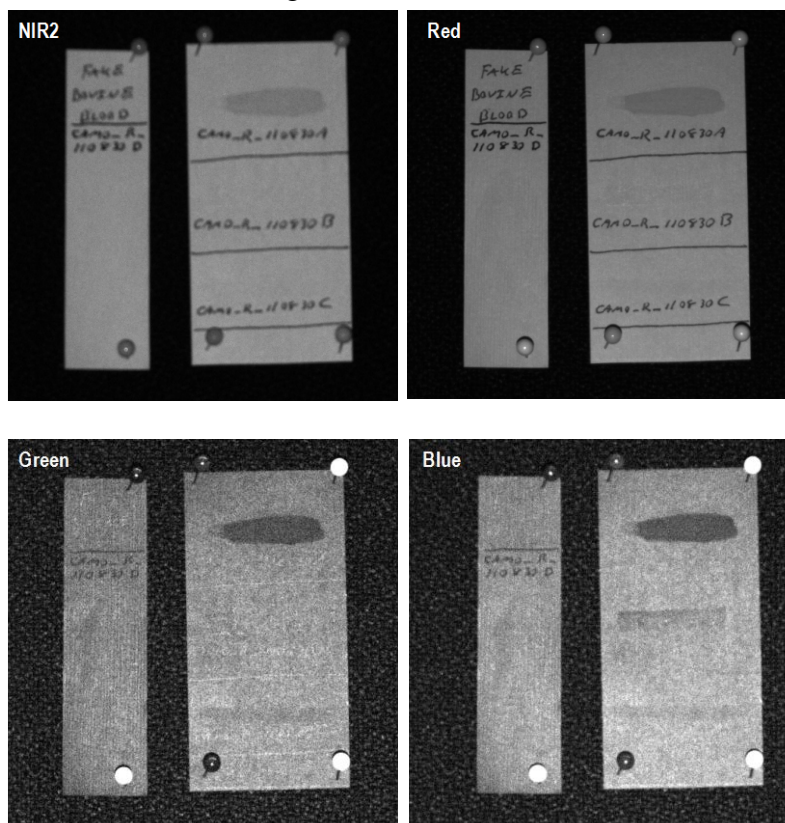


Figure 5 First multispectral images

Only spot (A) is clearly visible in NIR channels, while all four are visible in blue. It is clearly evident that the images can be used to detect and distinguish between four spots that are all red and are on the red background. Also note that one of the black inks is invisible in blue and green images

III.2. Multispectral Analysis of Ink Samples

We received some ink samples from George Reis of Imaging Forensics that he obtained from his contacts in the community. Per notes surrounding the sample writing, they had been previously analyzed using inspection microscope. Microscopic inspection reveals the different color pigments that are combined to make the desired color. These internal compositions can be used to distinguish two inks of the same visible color. The breadboard multi-spectral camera provides a different approach of a broad spectroscopic inspection. While it lacks the high magnification of the microscope to detect individual color pigments, it is still able to identify the composition differences by measuring bulk response of the pigments in spectral bands outside the visible region. The advantage is an ability to cover a large area in a short amount of time with a field of view that is orders of magnitude larger than that of an inspection microscope. Figure 6 shows a color digital camera photograph. Four black inks (BK1, BK2, BK3, and BK4) and four blue inks (BL1, BL2, BL3, and BL4) are pointed out to discuss use of multi spectral images for further differentiation.

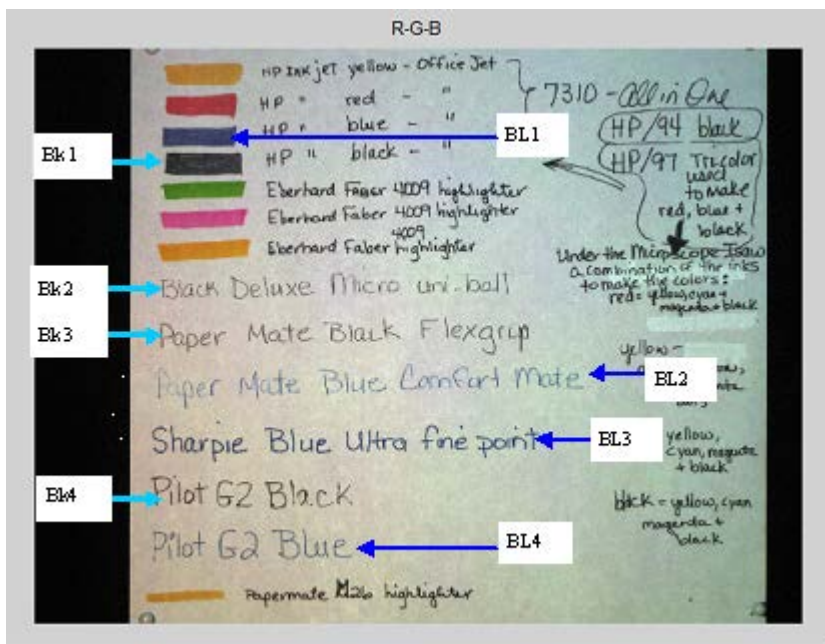
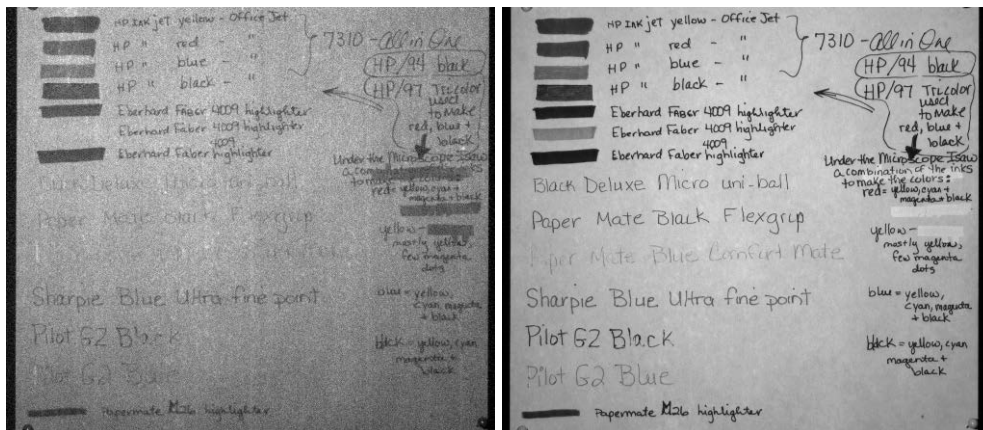


Figure 6 A color digital camera image of ink samples Black (Bk) and blue (BL) colors are pointed out to demonstrate use of multispectral analysis.

Figure 7 shows images in all six wavelength channels. The most interesting behavior was at red and NIR wavelengths. All the samples get progressively more reflective as the wavelength increases, but the trends are different for different inks. The ink becomes less and less “visible” as its reflectivity blends into the reflectivity of white background. While all the markings are visible in green wavelength (the center of the visible spectrum), some begin to disappear at red, a larger number blend into the background at NIR1 (740 nm), and about half of the writing and the majority of marker patches have blended in (except for one) at the longest wavelength used (NIR2-870 nm).

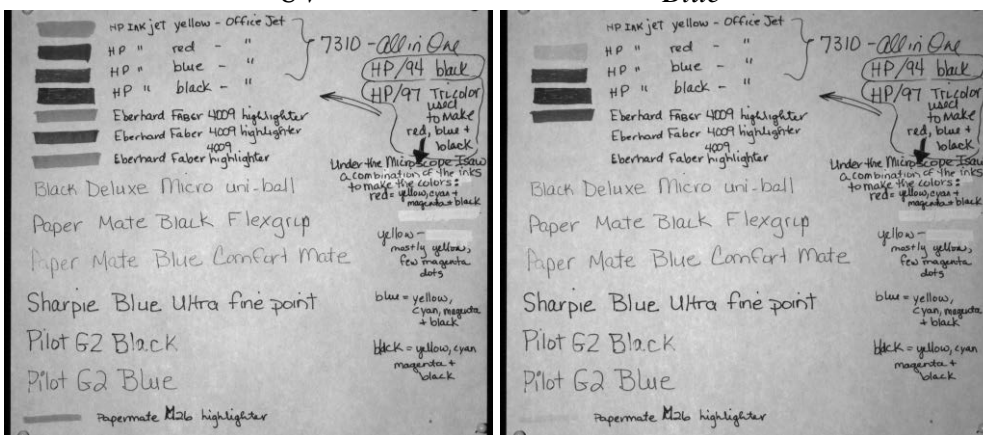
Figure 7 shows images in all six wavelength channels. The most interesting behavior was at red and NIR wavelengths. All the samples get progressively more reflective as the wavelength increases, but the trends are different for different inks. The ink becomes less and less “visible” as its reflectivity blends into the reflectivity of white background. While all the markings are visible in green wavelength (the center of the visible spectrum), some begin to disappear at red, a larger number blend into the background at NIR1 (740 nm), and about half of the writing and the majority of marker patches have blended in (except for one) at the longest wavelength used (NIR2-870 nm).

In Figure 8, we illustrate the images rendered using a false color map. We show NIR1-B-UV and NIR2-B-UV mapped into the R-G-B part of the spectra. A large number of them appear reddish as due to higher reflectivity in the NIR. Inks that appeared similar in color in the conventional color digital image now appear to be of different color, e.g. all black inks Bk1 through Bk4 now appear to have different colors whereas the blues, BL2 and BL4 also appear substantially different from BL1/BL3. The breadboard camera could not distinguish between BL1 and BL3. The compositions of these two inks have very similar response even outside the visible wavelengths.



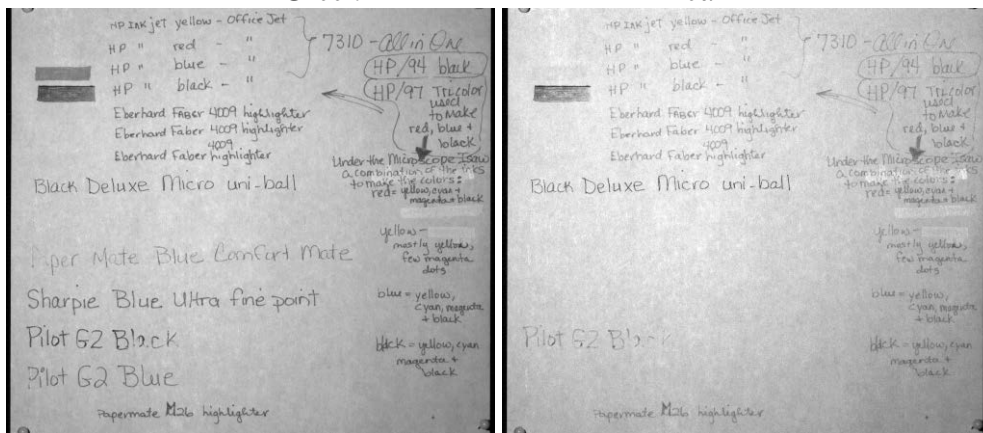
UV

Blue



Green

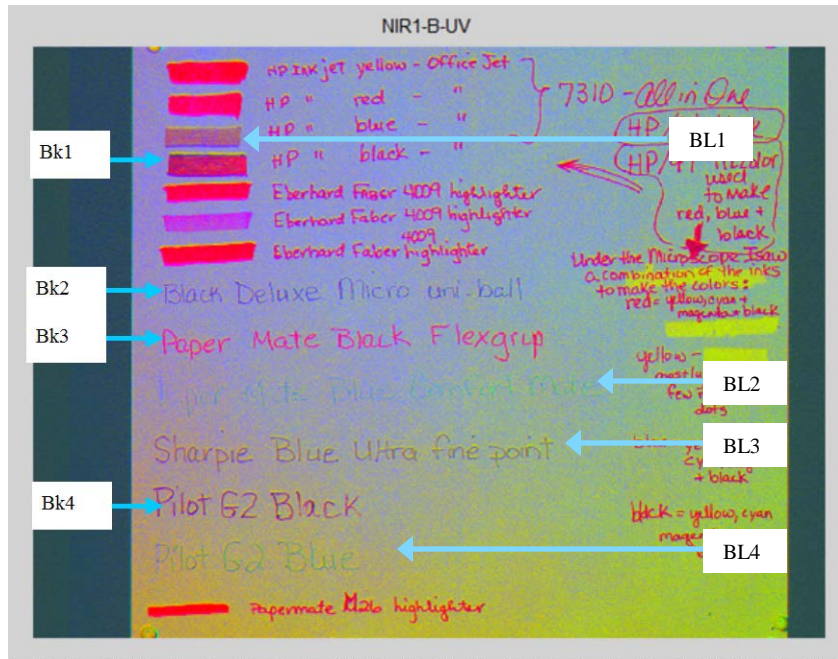
Red



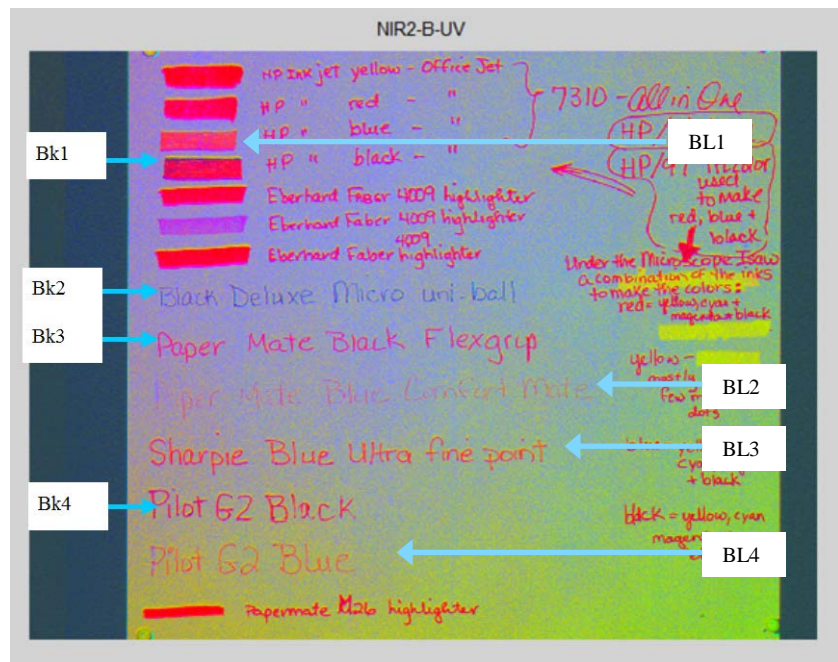
NIR1

NIR2

Figure 7 Ink images in all six wavelength channels
 The most interesting behavior was at red and NIR wavelengths. There is marked increase in reflectivity as wavelength increases and at some wavelengths the ink blends into the high reflectivity background. The wavelength at which this happens is different for different ink samples.



NIR1-B-UV False color map



NIR1-B-UV False color map

Figure 8 False color images of inks for ease of visualization
 Inks that appeared similar in color in the conventional color digital image now appear to be of different color, e.g. all black inks (Bk1 through Bk4) now appear to have different colors whereas two of the blues (BL2 and BL4) also appear substantially different from other blues (BL1/BL3). Multispectral imaging could not distinguish between BL1 and BL3.

III.3. Multispectral Analysis of Blood Stains on Cloth

We used two pieces of cloth for this experiment: One was an old, worn piece of Levis 509 Blue Jeans and the other was a new store bought red cloth (100% cotton). On each of these, we prepared three stains of sterilized bovine blood test soil, diluted with different amounts of de-ionized (DI) water namely:

Sample A - ACT 110913A 0.50g test soil in 9.5g DI water

Sample B - ACT 110913B 0.25g test soil in 9.75g DI water

Sample C - ACT 110913C 0.125g test soil in 9.875g DI water

We prepared the stains by releasing nominally 1 ml of solution on the cloth with a dropper. We placed the camera at 1.6 m normal incidence and Illuminator at 0.74 m and approximately 5° off axis. We collected six images in six different wavelength channels, and carried out algorithmic contrast enhancement.

Stains on blue jeans: All stains were visible to the eye and with a color digital camera, sample “A” being the most prominent and “C” being least. Figure 9 shows color digital camera photographs without and with flash. Brightness and contrast settings were optimized for the images.



Figure 9 Blood stain on blue jeans

Without flash (left) and with flash (right), simple brightness and contrast settings have already been optimized.

Next we imaged the target with the multispectral camera. A simple inspection of the individual channels revealed that the highest contrast information was at the shorter wavelength

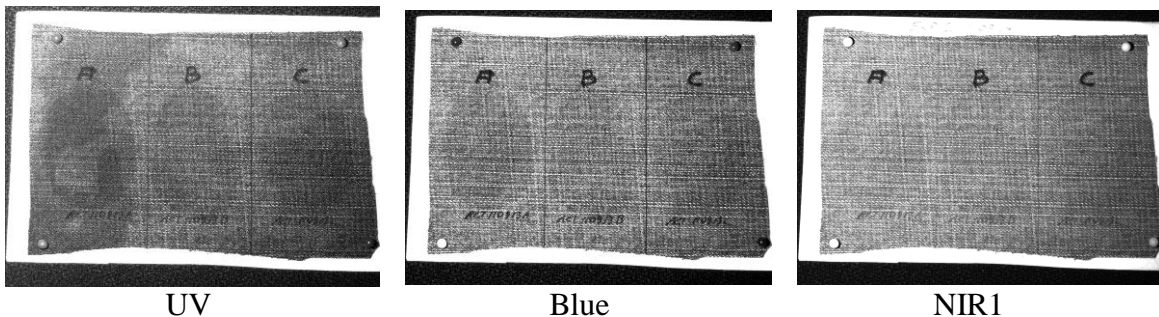


Figure 10 Blood stain on blue jeans: individual wavelength images.

UV image shows the highest contrast and an additional preexisting stain that is otherwise not visible. The contrast degrades at longer wavelengths; somewhat reduced in the blue image, and NIR1 image has very little contrast left. Single channel images at shorter wavelengths have higher contrast over conventional digital color photograph.

channels (UV and blue). UV image by itself has higher contrast than conventional digital image.

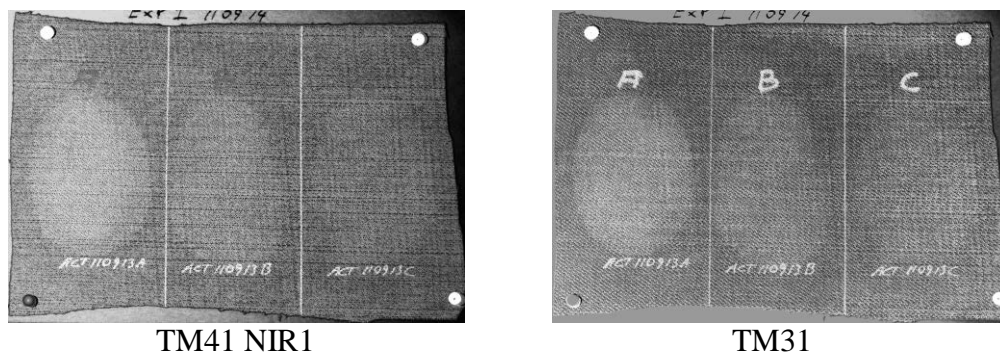


Figure 11 Enhancement through spectral measurements

The spot edges are better defined. See IV.4.1 for description of TM41 and TM31 algorithms.

Figure 11 and Figure 12 illustrate enhancement through spectral processing and false color rendering. Better definition of the spot edges is possible for higher concentration stains, and false color rendering can effectively draw the user's attention to the stain. The enhancements are described in more detail in section IV.3.

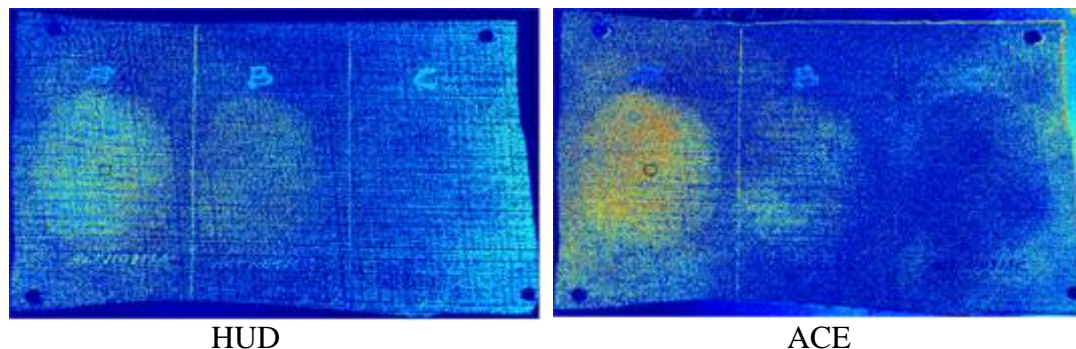


Figure 12 Spectral enhancement algorithm results: HUD and ACE with false color map
Spectral HUD (IV.5.3.4) and spectral ACE (IV.5.3.3) rendered in false color can make the stains really stand out, particularly for higher concentrations.

Stains on red cloth: We used a red cloth background to create a different type of challenging detection scenario. While blue jeans make a difficult target due to inherent texture and stains, red cloth does so through similarity of visible color with the stain. We used the same blood concentrations as used on the blue jeans. To an unaided eye and in a color digital camera photograph (passive, no flash), the highest concentration blood stain (A) was clearly visible, intermediate concentration stain (B) was only slightly visible, but the lowest concentration stain (C) was undetectable. We then took a picture with a flash despite having sufficient ambient illumination. The forced use of flash improved the contrast of stains A, and B, but stain C was still too close to detection threshold. See Figure 13.



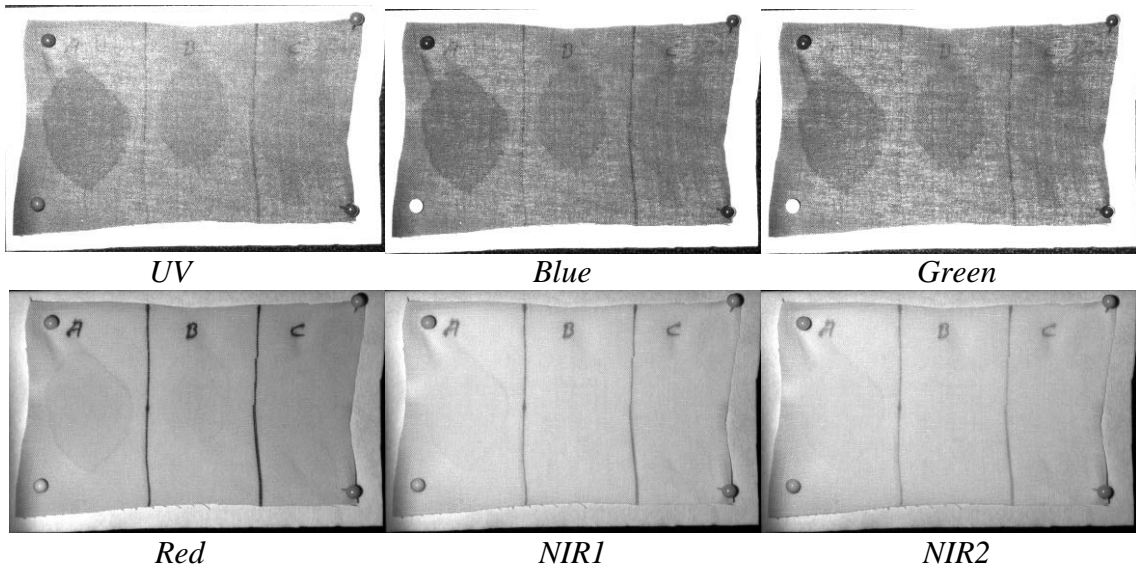
Passive

With forced flash

Figure 13 Blood stain on red cloth: color digital camera pictures

Spots A and B are detectable; C is undetectable in passive image and barely detectable when forced flash is used

Figure 14 shows the pictures in individual wavelengths. It is obvious that there is a higher contrast at short wavelengths, particularly UV and blue. The red through near infrared parts of the spectrum show very little contrast and only the highest concentration spot is visible. Visual comparison of lower wavelength images with Figure 13 shows that breadboard camera has enabled both better detection threshold and significant contrast enhancement even before post processing.



UV

Blue

Green

Red

NIR1

NIR2

Figure 14 Blood stain on red cloth: Individual wavelength images

Shorter wavelengths have significantly higher contrast compared to longer wavelengths

We were successful in further algorithmic enhancement by processing combinations of color channels. Figure 15 shows some examples. Contrast has been further increased for all three, particularly for the smallest concentration (C) and false color rendering provides a more effective visualization than gray scale.

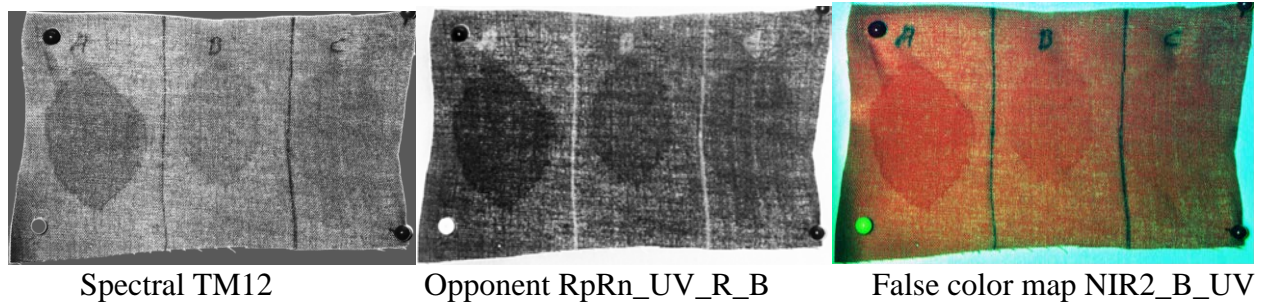


Figure 15 Bloodstains on red cloth: Enhanced using digital techniques Contrast is further improved compared to raw single wavelength images Figure 14; particularly noticeable for the least concentration sample C. False color rendering produced improved visualization. See section IV.4 for a description of spectral processing, and IV.2 for a description of opponent processing.

III.4. Evaporated Solvents

Encouraged by the success in detecting and enhancing the visibility of bloodstains on red cloth, we attempted detection of a laboratory solvent, a standard polyimide thinner (PI thinner). Solvent spills are potential evidence in an industrial setting or possibly in an illicit drug manufacturing location. We assumed that slowly evaporating solvents (low vapor pressure) such as typical polyimide thinners may leave behind a stronger signature compared to highly volatile solvents by inducing permanent texture changes. To prepare the imaging target, PI thinner was dropped on to two separate regions of the material. In the first region the PI thinner was evaporated off on a hotplate at 100°C while in the other region it was allowed to evaporate off under ambient laboratory conditions. Samples were prepared on blue jeans as well as on red cotton cloth.

On blue jeans, while wet, the stain was visible to the eye, and could be imaged and enhanced with the breadboard camera (we use it to illustrate some of the algorithms in the section on image processing). Upon complete drying, no signs of the stain could be identified on the blue jeans due to inherent texture of the material.

On the red cloth, however, at the drop locations; we could identify circular marks using texture analysis. It was not possible to identify any signs of the stains in single wavelength channels. See Figure 16.

Given the ultra-low contrast of the observation, we performed a blind test where more samples were prepared and the location of the stain was not revealed to persons algorithmically enhancing the image. They were not able to spot the location correctly. But when the location of the drop was revealed, it was possible for them to see obscure contrast differences.

We conclude that while it may be possible in certain conditions to observe stains left behind by an evaporated solvent, the resultant contrast, even after digital enhancement, is too low to be detected. Pushing enhancement algorithms to the limit also enhances other texture elements (clutter), and makes detection difficult and prone to errors, if not impossible.

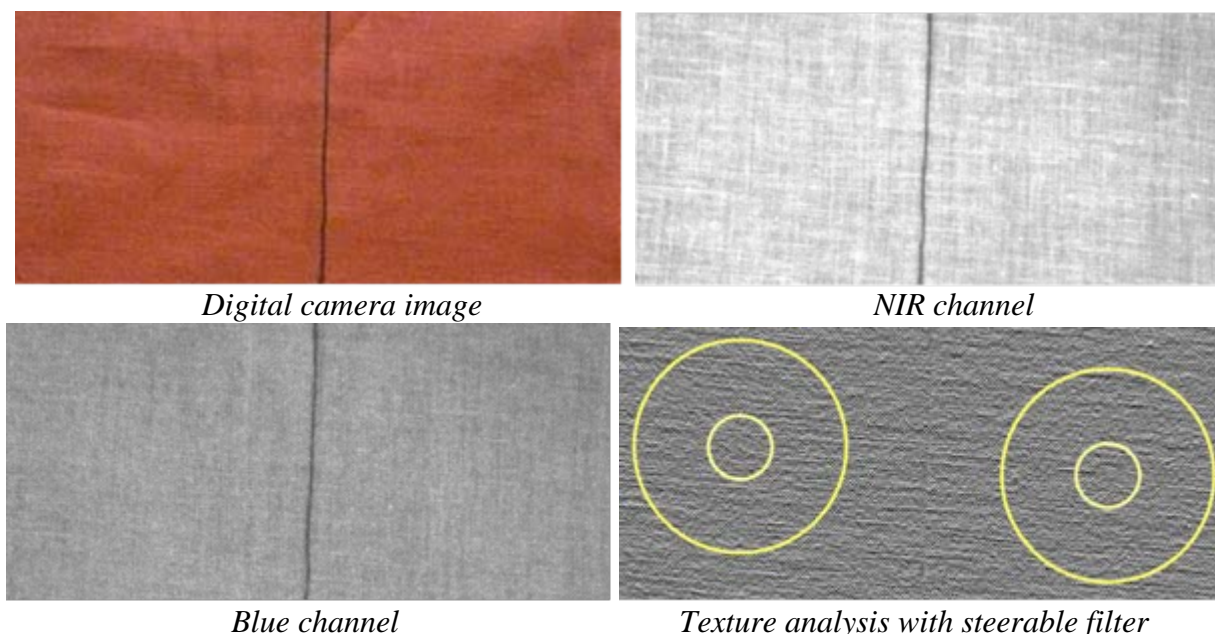


Figure 16 Polyimide thinner on red cloth

The locations where solvent was dropped and evaporated are inside yellow circles (bottom right). There is a dimple (inside the small yellow circle) and a faint circular region with slightly different texture surrounding it (inside the larger yellow circle)

III.5. Imaging Latent Prints

Hand and shoe prints on a transparent polycarbonate window: We created a footprint (shoe print) and handprint onto a transparent polycarbonate window. The prints were undetectable by the naked eye, except when viewed at extreme grazing angles. The illumination needed to be at extreme angle as well. A conventional digital camera could not image it at all, with or without flash (Figure 17). We took multispectral data with room lights ON, with nearly normal incidence geometry (camera at 2.2m distance, Illuminator at 1 meter and $\sim 5^\circ$ off axis. We observed that latent prints have the highest contrast under specular illumination. Also, the diminutive thickness



Without flash



With flash

Figure 17 Conventional camera cannot capture prints on reflective targets

of residual material produces high contrast under narrow-band illumination as opposed to broadband, and certain wavelengths yield higher contrast than others. The challenge is to balance the undesirable saturation from a specular reflection with the prints that are best visible directly around the saturated area. See Figure 18.

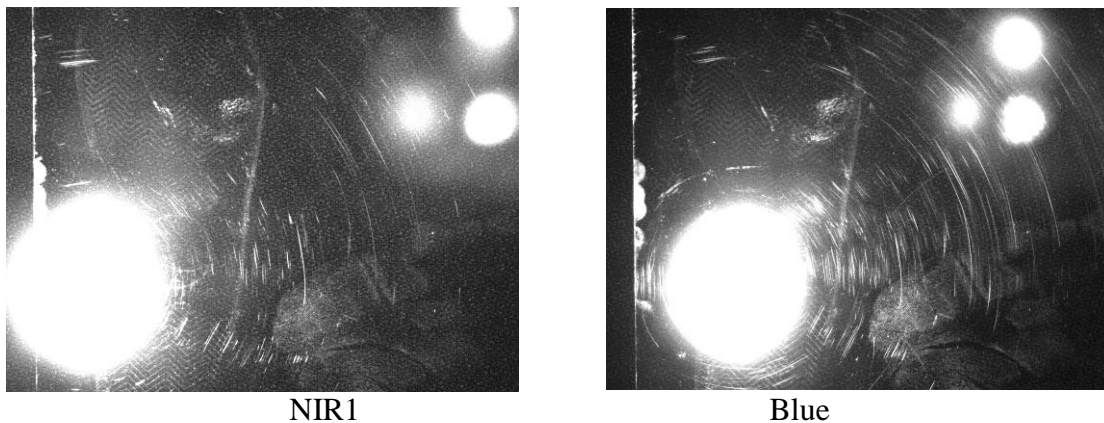


Figure 18 Raw images from NIR1 and Blue channels

Single channel images can pick up the prints. The contrast is the highest around the saturated specular return and slowly degrades as we move away from it (scattered return). Shoeprint is above the largest saturated region and the hand print is to the right of it.

Taking a simple minimum across the visible channels followed by a sigmoid contrast stretch proved to be very effective in capturing the maximum area of the prints, while reducing saturated unusable glint. See the digitally enhanced composite in Figure 19.

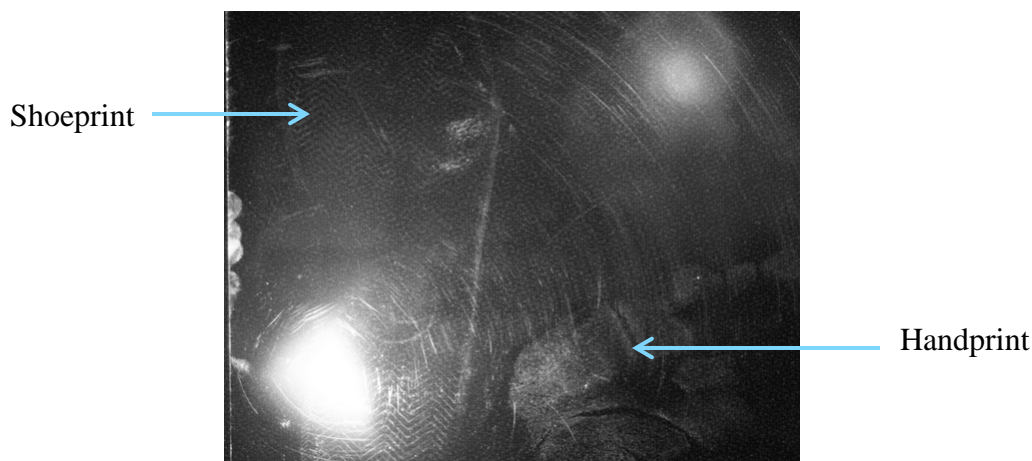


Figure 19 Enhanced images of prints on transparent polycarbonate window

Simple minimum across the visible channels shows a lot more of the prints and a lot less of the unusable saturated return.

Hand print on an opaque plastic sheet: We created handprint onto an opaque but smooth finished nylon polymer sheet. The image capture geometry was at normal incidence, with parameters identical to the previous case (transparent window). The print is very difficult to

detect by the naked eye, except at extremely oblique viewing angles, and impossible to detect from distance. The conventional digital camera is also unable to capture any prints with or without flash. See Figure 20.

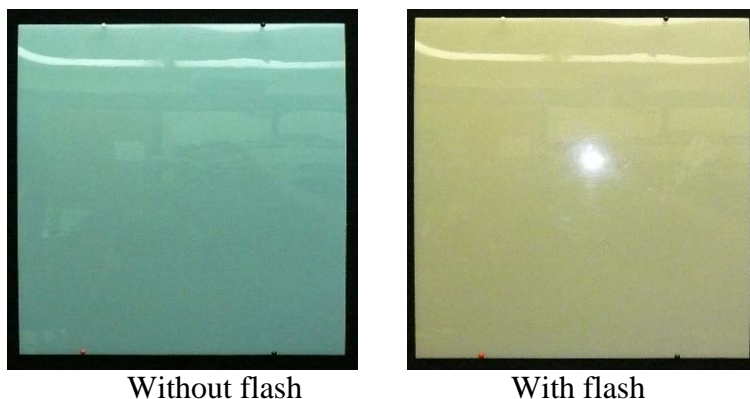
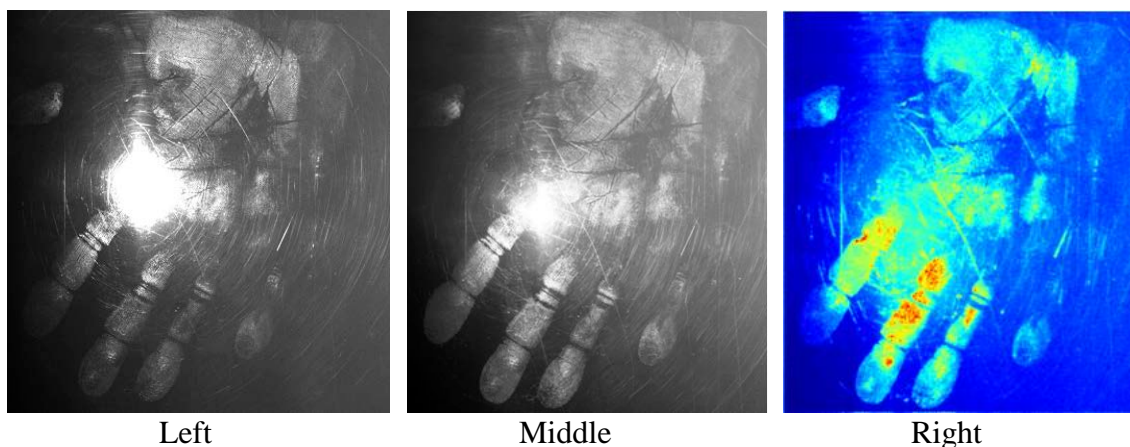


Figure 20 Conventional digital camera picture of a glossy opaque sheet with a handprint

The breadboard camera could easily detect the print in all wavelength channels. An enhanced composite using a simple minimum across visible channels (on a per pixel basis) followed by sigmoid contrast stretch was again very effective. In addition to contrast improvement, the result showed greatly diminished effect from the saturated returns from multiple LEDs. See Figure 21 (middle).

Handprints tend to have a periodic ridge texture. We used an algorithm (Oriented Pyramid) which uses spatial frequency analysis to detect the presence of such structure, and used false color to highlight these areas. The algorithm correctly highlighted the entire palm area. The central regions on the fingers, -where the parallel ridges are the most uniform- appear to be the brightest. The result is shown in Figure 21 (right).



*Figure 21 Breadboard camera image captures of handprints on opaque surface
The best contrast was in the red channel (left) A simple minimum across the visible followed by a sigmoidal stretch (Middle) was very effective.
Frequency analysis showing areas with periodic ridge pattern highlighted in false color (Right) also contrasted the region with hand print.*

In another interesting analysis, we used spectral processing. This process analyses a user selected point (in this case either a point on the palm or on the finger was used) and highlights regions that are spectrally (in wavelength) similar to that point. This procedure unexpectedly distinguished between the palm area and the fingers. The only difference between the two areas appeared to be related to handling of greasy food with the fingers before making the print. This ability to examine trace differences within latent prints through image processing could be a very valuable tool. See Figure 22.

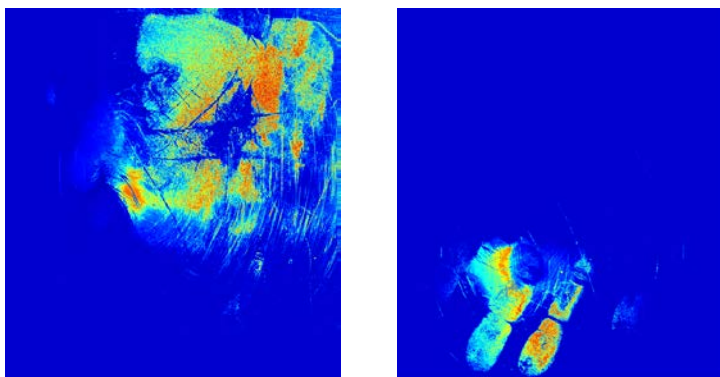


*Figure 22 Spectral processing identified difference between palm and finger print
The primary difference was that the fingers had handled greasy food prior to leaving the print*

We also analyzed the images using a Gabor filter to demonstrate that they are of sufficient quality to be able to match against a database. The details of that analysis are in the image processing section [IV.9]. This capability may allow standoff image based capture of prints without the need to use laborious and time consuming methods using powder and brushing (which are also intrusive).

III.6. Solvents that Leave Residue

Salt Solution: We placed 10mL of 15% salt (NaCl) solution on a white clean room cloth. The solution was evaporated off on a hotplate at 80°C. There was no visible stain on the cloth. There was a very small texture difference in the center. However, single wavelength active illumination at near normal incidence angle very clearly revealed the stain left behind, with longer wavelengths showing slightly higher contrast (Figure 23).

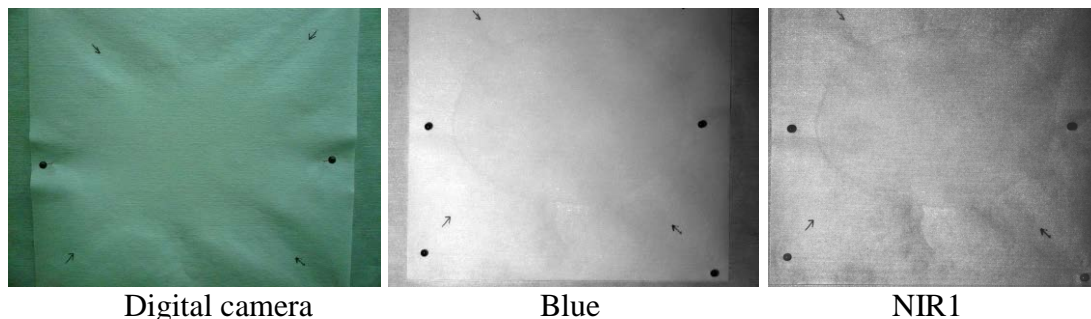
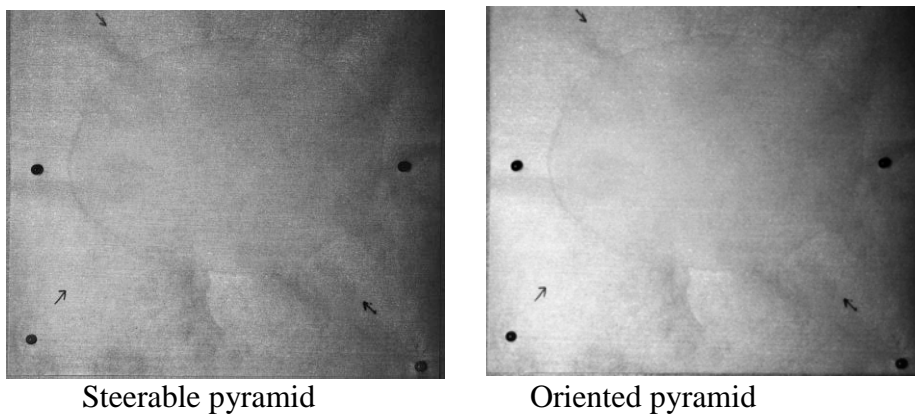


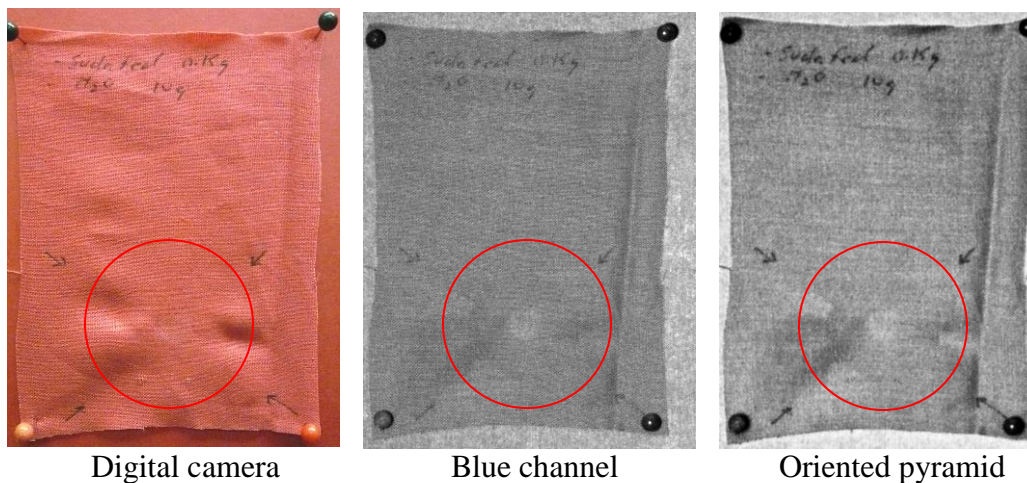
*Figure 23 Stain left behind by salt water
Single wavelength images reveal the outline of the stain*

Texture analysis algorithms were the most effective in processing the data to produce a high contrast image. They produced results that had slightly better contrast than the best contrast in the single wavelength channel (NIR1). See Figure 24.



Steerable pyramid Oriented pyramid
Figure 24 Texture analysis based enhancement of salt stain

Pseudoephedrine (Sudafed) Stain: We applied ~1mL of a 1.5% Pseudoephedrine solution to 100% cotton, red cloth. The drug can only be purchased in regulated quantities to combat illicit methamphetamine production. The solution was evaporated off using a hotplate at 80°C. A small (~1cm) circular area was slightly visible and appeared pale colored. The digital camera picture was very similar to the appearance to the naked eye, except the spot was even more obscure. When imaged with the breadboard camera, not only did it enhance the obscure spot but detected a larger circle circumscribing it that was not visible to the eye or in the digital camera image. Texture analysis using oriented pyramid again proved to be the most effective digital technique.



Digital camera Blue channel Oriented pyramid

Figure 25 Pseudoephedrine stain

Conventional digital image shows a barely visible small spot. The highest contrast raw image (in blue channel) shows the small spot and a larger concentric circle around it (both within the red circle). Texture analysis based oriented pyramid processing further enhanced the visibility of both these features.

III.7. Polarization Analysis of Prints

Ideal surfaces for capturing latent prints tend to be smooth, or in the optics terminology, glossy or specular. Off-axis specular reflections create a polarization signature due to either difference in reflection of p and s polarization components, or due to phase shift between them. The “p” component is the component of incident polarization parallel to the plane of incidence and “s” component is the component perpendicular to the plane of incidence. We experimented with lighting (polarization and incidence angle) and polarimetric analysis of the return that theoretically had the promise of contrast enhancement in the image.

Figure 26 shows two photographs of prints on a hardcover book taken in an off-axis imaging geometry. The polarized nature of specular reflection is obvious. The prints, which are contained almost entirely in the specular reflection part, are visible in one polarization state and invisible in the other. Unpolarized image (not shown) is essentially the sum of the two images and thus has reduced contrast compared to the polarized image.

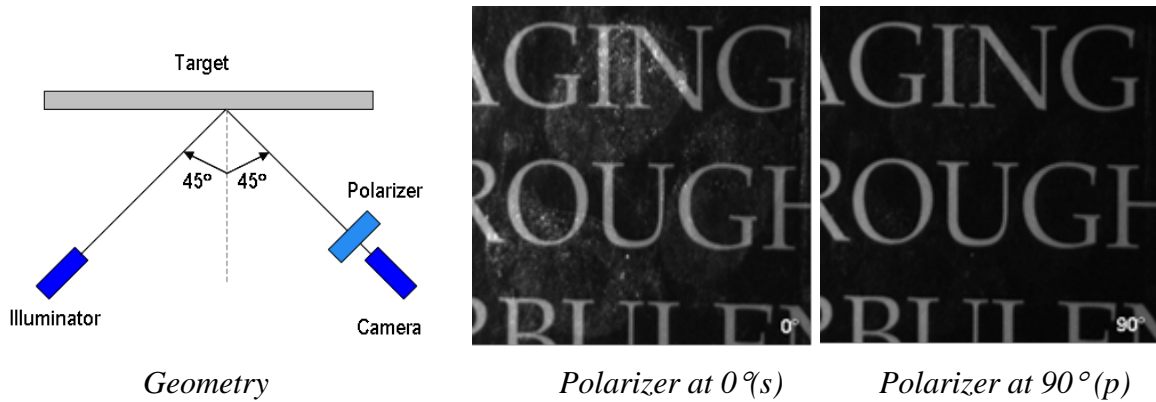


*Figure 26 Off axis imaging geometry and polarized images of prints
Polarized nature of the prints image can be clearly seen. This is expected since the prints are only visible in the specular parts of the image and specular reflection tends to get highly polarized near Brewster angle [12].*

We also collected polarized images by orienting the polarizer at 0°, 45°, 90°, and 135°. We then analyzed the degree of linear polarization (DOLP) and angle of polarization (AOP) of the image. The finger print information was entirely located in the DOLP image and had higher contrast compared to the intensity image (see Figure 27). Capturing the four polarization images and post processing the data can be seen as a “virtual polarizer”, where the user does not have to know or manually find the correct orientation of the polarizer to achieve the highest contrast. In a portable field camera, the four polarization images will be taken sequentially using a single fixed polarizer and an agile liquid crystal polarization rotator.



Intensity image

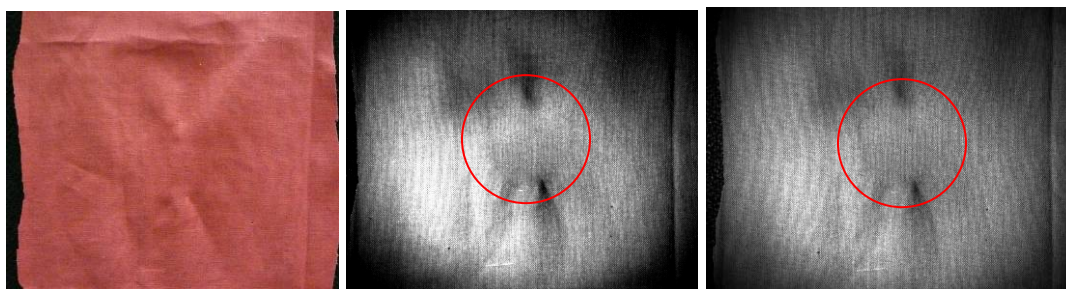
DOLP

AOP

Figure 27: Degree of linear polarization (DOLP) and angle of polarization (AOP) images. The thumbprint image is best visible in the DOLP image and has higher contrast compared to the intensity image.

III.8. UV/Fluorescence Imaging of Blood Stains

Blood stain on red cloth: We prepared a dilute (1% test soil by weight) solution of bovine blood sample and placed about 10 ml onto a red cotton cloth. The cloth was dried on a hotplate at 80°C. The stain was not visible to the eye or in a conventional digital camera image. We illuminated the sample with UV curing light (Filtered mercury arc lamp with spectral filter, primary illumination at 365 nm). Arc lamp was replaced with a dual LEDs added to the illuminator midway in the trade study [e.g. III.8] and produces equivalent results. The images were taken in all six channels resulting in one combined UV reflectance/fluorescence image in the UV channel (dominated by UV reflectance) and fluorescence images at longer wavelengths. The brightness progressively dropped as the wavelength increased and UV and blue channels contained the maximum information. See Figure 28. There was no detectable light at red or NIR wavelengths.



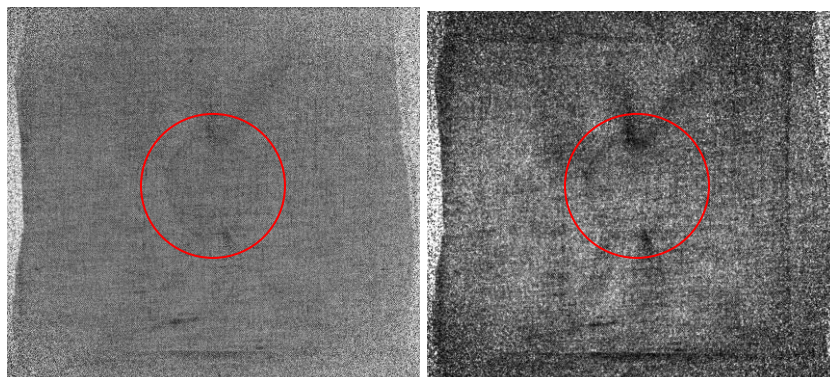
Color digital camera

UV

Blue

Figure 28 UV/Fluorescence images of blood stain on red cloth. The shorter wavelength channels resulted in images with sufficient brightness, and high contrast, UV and Blue channel images are shown: a stain boundary is visible in these images.

Spectral processing was successful in further enhancement, the stain boundaries are better visible (Figure 29). The result is particularly impressive given the density of residual material is $<5 \text{ mg/cm}^2$ but still can be detected through imaging from a distance.



TM14

ND32

Figure 29 Spectral processing to enhance the stain contrast; The stain boundary visibility is pronounced

III.9. UV/Fluorescence Imaging of Saliva

Saliva stain: The material used for this sample was 100% cotton dark blue used t-shirt cloth. We divided the sample vertically into two halves. We delivered human saliva onto each half with different concentrations. The left side was 20% saliva diluted in water and approximately 1.5 gm applied. The right side was pure, undiluted saliva and $\sim 1 \text{ gm}$. was applied onto the cloth. The aqueous portion of the saliva was allowed to evaporate in ambient conditions before final imaging. We used the UV curing source as an illuminator for this experiment as well. Both stains were virtually undetectable by the naked eye or in a conventional digital camera photograph.

However in UV/fluorescence mode both stains were clearly visible. Furthermore a concentric ring pattern inside the spots could also be identified (see Figure 30). The fluorescent light diminished as wavelength increased. The highest contrast was observed in UV channel followed by blue and green. The green channel was light starved but visible. In red and NIR channels there was not enough light emitted for meaningful imaging as the spectral separation of these wavelengths from the pump wavelength (UV) is too large.

Figure 31 shows the digital enhancement of UV channel and spectral opponent color processed image with green, blue and UV channels. There is subtle but unmistakable improvement in the visibility of the concentric structure in the stain on the left. There is better definition of the edges of the stains.

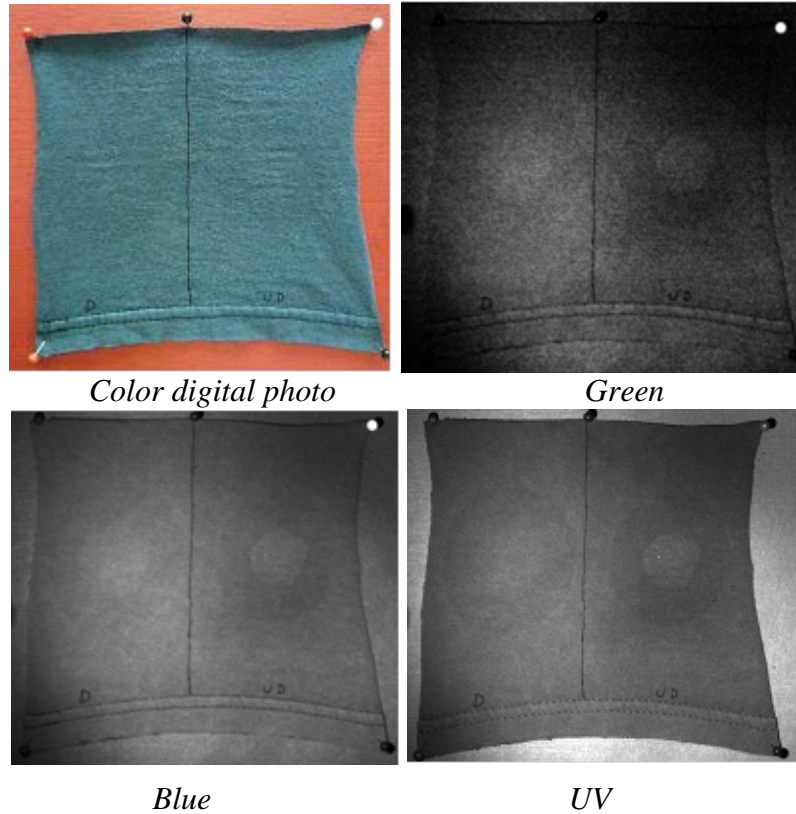


Figure 30 Color digital photo and UV/Fluorescence images of saliva stains on red cloth. The stains in both concentrations are virtually undetectable in the color digital photo, but clearly visible (including the concentric pattern in UV/fluorescence image). The highest contrast is in the UV channel, followed by blue and green. In the red and NIR channels there is not enough light available for imaging.

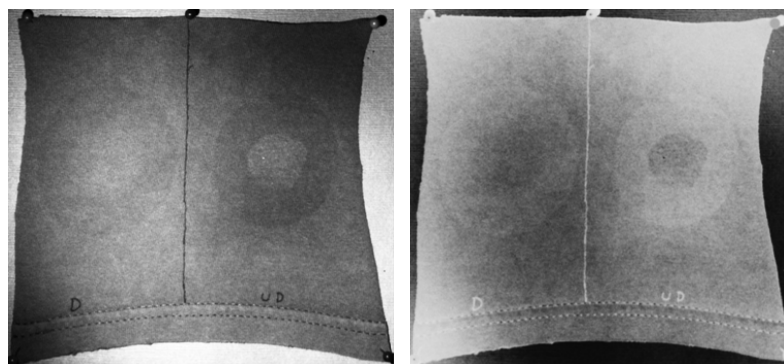
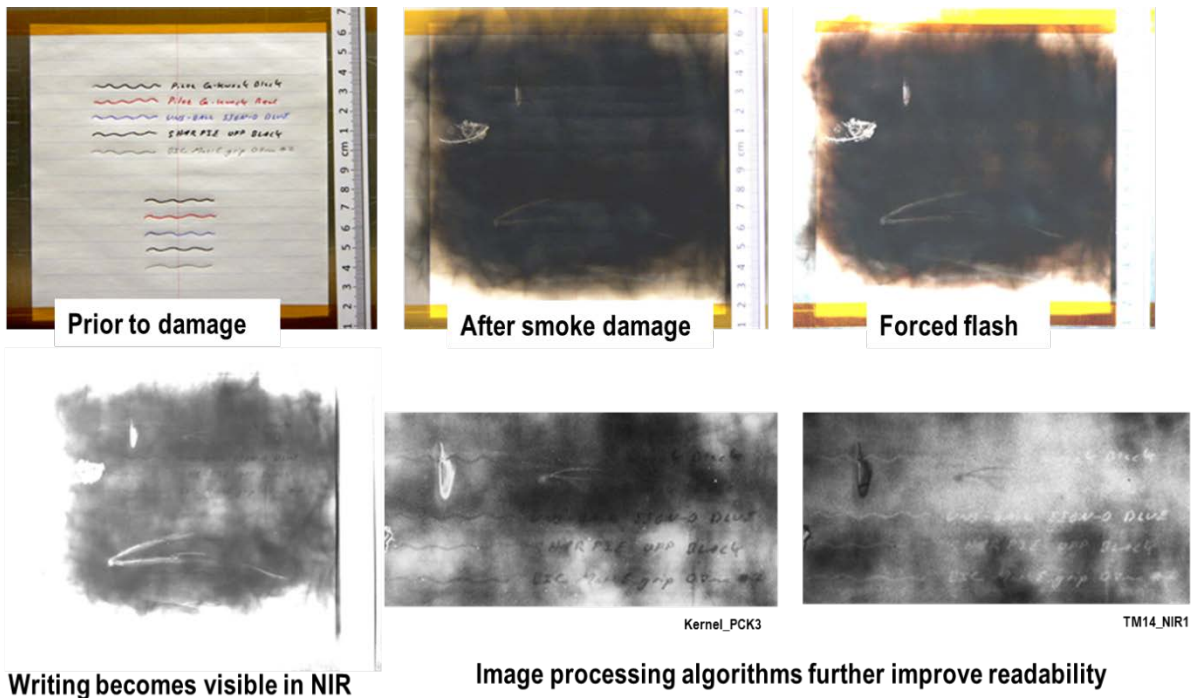


Figure 31 Enhanced UV/Fluorescence images of saliva stains on red cloth. Upon digital enhancement, the concentric structure of the stain on the left is more apparent and the definition of the edges of the stains is enhanced.

III.10. Soot Damaged Paper

Figure 32 shows some images of smoke damaged paper. The sample was prepared by writing with different inks on paper and then subjecting it to a coating of soot created using a candle. The text was invisible to naked eye or the color digital camera. Forced flash indicated presence of texture and writing underneath, but it was long wavelength channel images that produced the clearest pictures. Ability of long wavelengths to penetrate thin layers is known [13] and the results were in line with the expectations. Image processing algorithms that exploit spectral measurements were successful in contrast enhancements making it easier to read the text.



*Figure 32 Imaging smoke damaged paper
Longer wavelengths, particularly NIR1 was the most effective in penetrating the soot layer to reveal the detail underneath*

III.11. Experiments in Outdoor Environment

We imaged two samples in outdoor environment to test the ability of the camera to operate without the need for darkened scene (Figure 33). The samples imaged were synthetic bovine blood (described in section III.3) and saliva (described in section III.9). The distances were similar to the ones used inside the laboratory i.e. camera at normal to the sample at 1.7 m distance and illuminator at slightly off normal (5°) at 0.8 m for multispectral mode and 0.5 m for fluorescence mode. Figure 33 shows the imaging setup on the patio under an 8 feet tall cloth canopy with open sides. The experiments were performed on a clear day in the afternoon with background irradiance of 45 W/m^2 , which is ~ 19 times higher than that of the measured indoor setting (2.4 W/cm^2). We mounted the breadboard camera alongside a color digital camera. We collected two images for each wavelength channel; one with the LED strobe illuminator on, and the other (background) with the illuminator off. We then subtracted the background from the LED illuminated image.

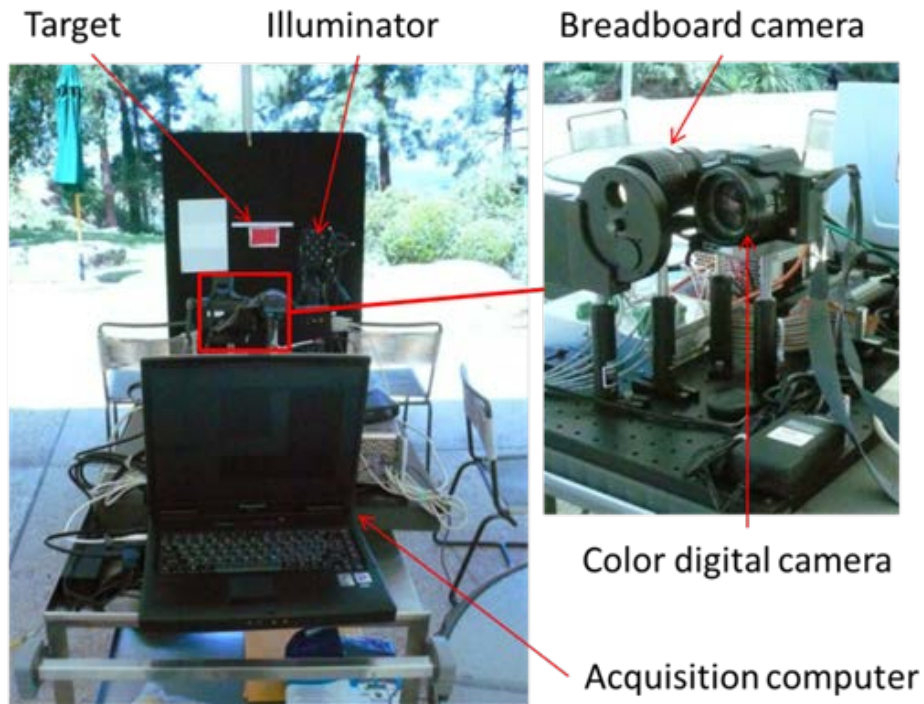


Figure 33 Imaging in outdoor environment

The image collection for sterilized bovine blood stains on red cloth (A, B and C in decreasing order of concentration, C is barely visible to the eye or in color camera image) produced results very similar to the experiment performed indoors. Shorter wavelength images had the highest contrast while the stains were barely visible in the red and in NIR wavelengths. Figure 34 shows the images acquired in the blue wavelength namely LED illuminated image, background image and background subtracted image. It can be clearly seen that LED illumination is significantly stronger than the background. The figure also shows comparison of background subtracted blue image with an indoors blue image. The stains have comparable contrast. The white paper behind the cloth is saturated in both LED lit and background imaging and subtraction results in a black background instead of white.

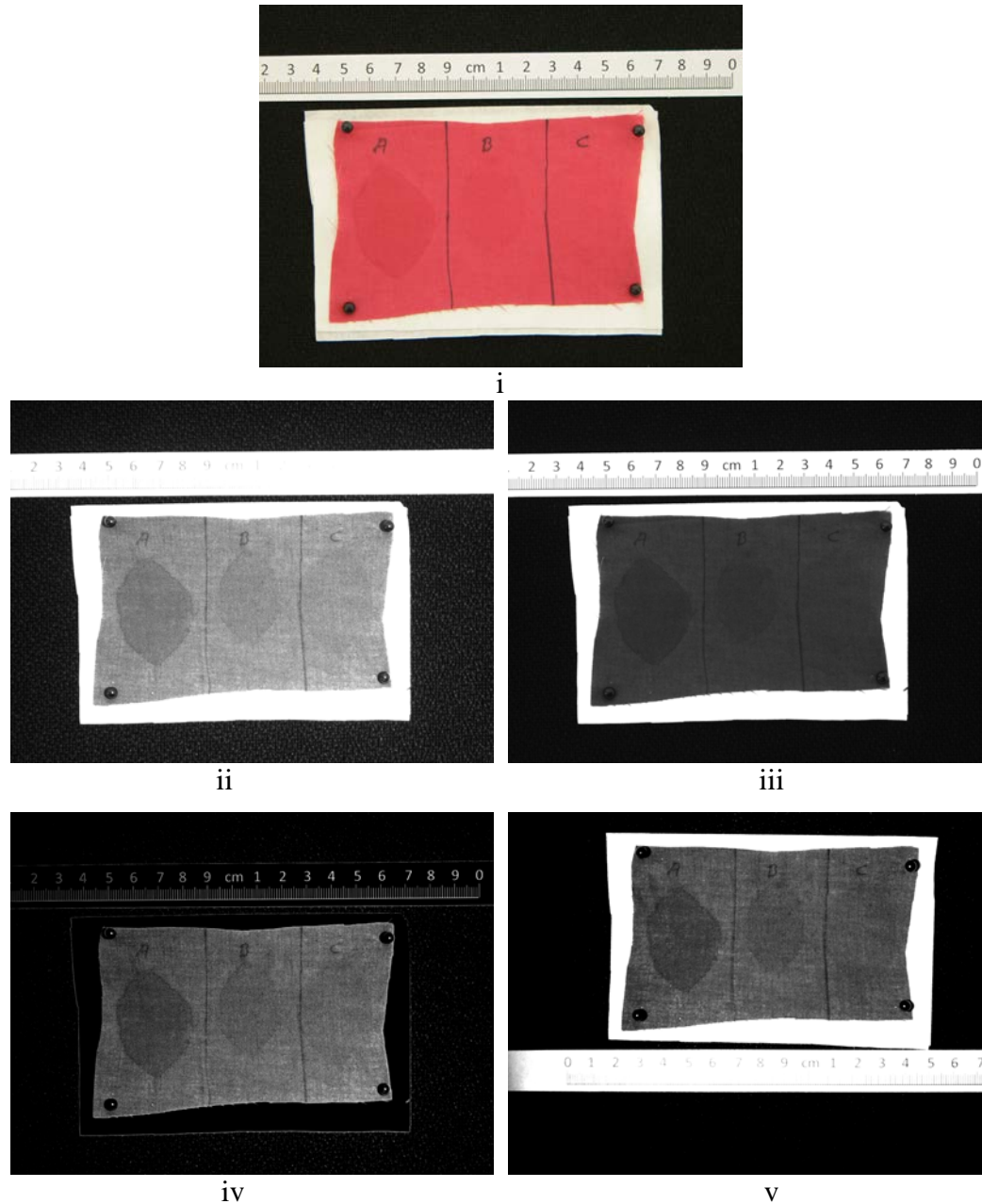
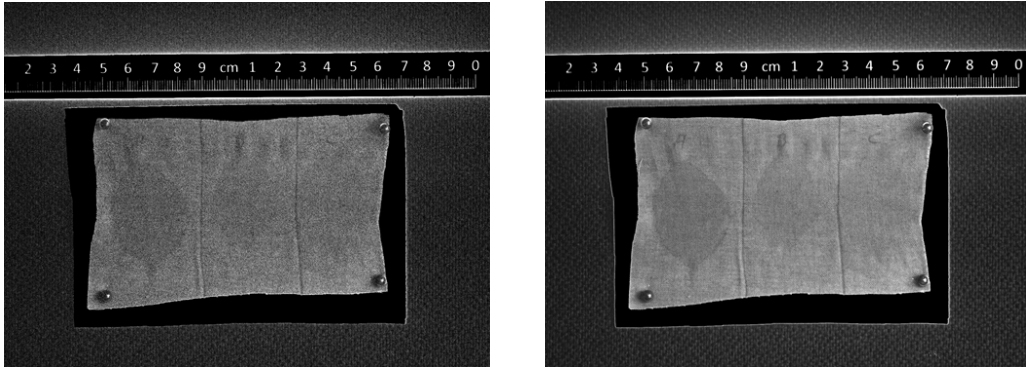


Figure 34 Multispectral imaging in outdoor environment. Color digital photo (i) and blue channel images collected in outdoors with LED on (ii), background image with LED off (iii) and background subtracted image (iv). The contrast of background subtracted outdoors image is similar to that of the indoor image (v).

Fluorescence mode is more susceptible to being suppressed by the background compared to multispectral mode, due to significantly weaker fluorescent emission than diffuse reflectance. Figure 35 and Figure 36 show images of blood stains and saliva targets in the fluorescence mode where the illumination was UV and the imaging wavelength was blue. We obtained a background image with LED turned off after every single image. A single background subtracted image has a grainy appearance due to light starved imaging conditions. To improve the image quality, we acquired ten images and corresponding backgrounds in fluorescent mode. We

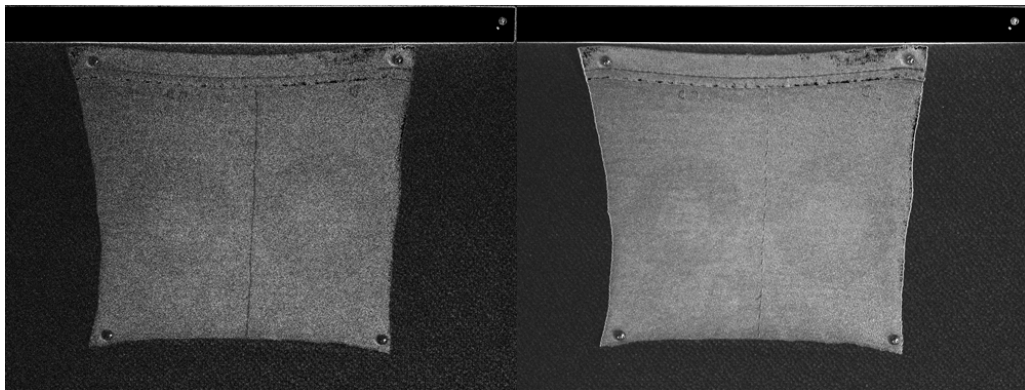


*Figure 35 Fluorescence imaging in outdoor environment
UV fluorescence mode images with UV illumination and blue receive wavelength. Image to the left has low SNR, image to the right which is a sum of 10 images has significantly improved SNR.*

subtracted background from each of the images and summed all ten for improved image SNR. This demonstrated ability to acquire fluorescence image in presence of bright sunlit environment is extremely valuable for a field portable device.



A



B

C

*Figure 36 Fluorescence imaging in outdoor environment
Color digital camera image and UV fluorescence mode images of saliva stains with UV illumination and blue receive wavelength. Image to the left has low SNR, image to the right which is a sum of 10 images has significantly improved SNR.*

IV. Description of Image Processing Algorithms

IV.1. Contrast Enhancement

To improve image contrast, we applied our Adaptive Dynamic Range Compression (ADRC) algorithm [14] to the different spectral images obtained with the breadboard camera (described in section III.6). ADRC is based on biological principles of signal interaction in the retinal circuits that enhance contrast and provide the necessary adaptation to local and global varying light levels. The underlying computational model of this process is based on the feed-forward center-surround shunting neural network of Grossberg [14]. The center-surround neurodynamics is described at pixel ij by the following differential equation [14].

$$\frac{dE_{ij}}{dt} = -AE_{ij} + (1 - E_{ij})[CI_C]_{ij} - (1 + E_{ij})[G_S * I_S]_{ij} \quad (1)$$

In equilibrium, this equation yields

$$E_{ij} = \frac{[CI_C - G_S * I_S]_{ij}}{A + [CI_C + G_S * I_S]_{ij}} \quad (2)$$

where E is the opponent processed enhanced image, I_C is the image that excites the pixel centered on the receptive field, and I_S is the image that inhibits the Gaussian surround G_S of the receptive field, A is the decay rate, and C is the excitatory rate[14]. When imagery feeding the center and G_S is from the same input image, the numerator equates to a difference-of-Gaussian (DoG) filter. When $C > 1$, it enhances high spatial frequencies superimposed on the background. The denominator adaptively normalizes contrast-enhanced imagery via the local mean.

Figure 37 and Figure 38 provide examples of ‘before’ and ‘after’ contrast enhancement results.

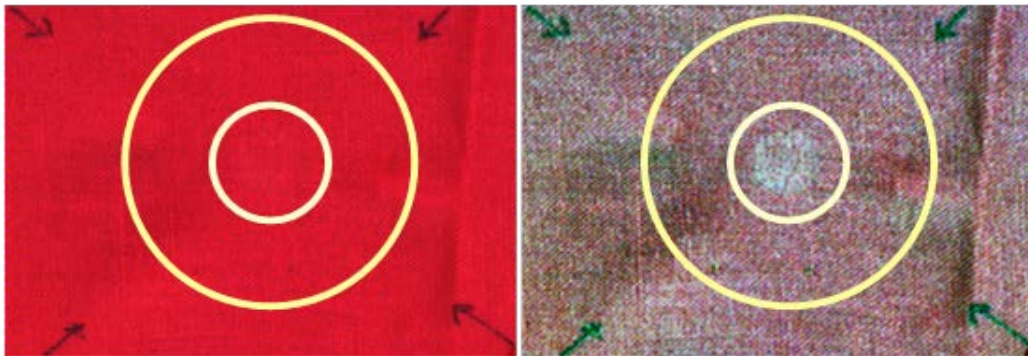


Figure 37: Results of contrast enhancement for RGB spectral images of Sudafed solution. Approximately 1mL of a 1.5% Sudafed solution was applied on a red, 100% cotton cloth and evaporated on a hotplate at 80° C. The stain was barely visible by the unaided eye. A small circular region (about 1 cm diameter) is clearly visible in the enhanced RGB image (right) but is barely visible in the unenhanced image (left). In addition, a larger, dark red, circular region that circumscribes the smaller white region is also visible in the enhanced RGB image yet undetectable in the unenhanced image.

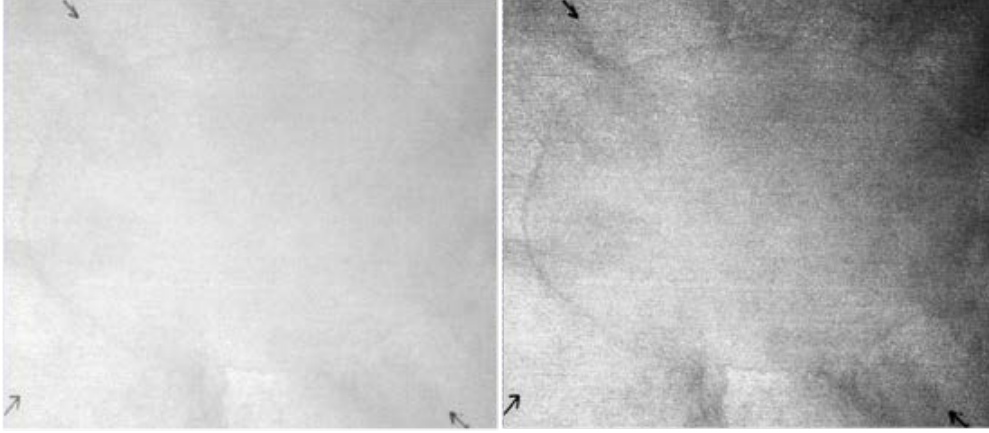


Figure 38: Results of contrast enhancement for NIR-1 spectral image of NaCl solution. Approximately 10mL of a 15% NaCl solution was placed on a white, clean room cloth and evaporated on a hotplate at 80° C. The stain was not visible to the unaided eye. The stain is clearly visible in the enhanced NIR-1 spectral image (right) while barely visible in the unenhanced image (left).

IV.2. Color Opponent Processing

Color opponency refers to the fact that the pairs red and green, yellow and blue, and white and black antagonize each other to contribute to color perception and color contrast [16]. Our color opponent model is based on biological principles of color vision and spectral enhancement in the human retinal and lateral geniculate nuclei (LGN) receptive fields. The underlying computational model is based on the feed-forward center-surround shunting competitive interactions between opponent color pairs: red-green or blue-yellow. The organization of the center-surround (denoted by concentric-circles icon in Figure 41 and Figure 42) is such that a cell that is excited by one of the antagonistic color pairs (e.g., red/blue) in the center of its receptive field will be inhibited by the other color (e.g., green/yellow) in the annulus surrounding the excitatory center [17]. If both opponent colors stimulate the center-surround in a balanced form, the output “activity” of the cell vanishes. Receptive field cell structures under investigation in this effort to evaluate their ability to enhance color contrast include: concentric single-opponent and spatially-opponent.

The center-surround operator is described at pixel ij by the following differential equation [17]:

$$\frac{dx_{ij}}{dt} = -Ax_{ij} + (B - x_{ij}) \sum_{k,l} I_{kl}^c * G_{klj}^c - (D + x_{ij}) \sum_{k,l} I_{kl}^s * G_{klj}^s \quad (3)$$

In equilibrium, this equation yields

$$x_{ij} = \frac{B \sum_{k,l} I_{kl}^c * G_{klj}^c - D \sum_{k,l} I_{kl}^s * G_{klj}^s}{A + \sum_{k,l} I_{kl}^c * G_{klj}^c + \sum_{k,l} I_{kl}^s * G_{klj}^s} \quad (4)$$

where x_{ij} is the opponent processed color image, I^c and I^s represent the antagonist color signals with I^c exciting the pixel centered on the receptive field and I^s inhibiting the surround of the receptive field, G^c and G^s are center and surround Gaussian filters, A is the decay rate, and B

and D are the excitatory rates [17]. This receptive field has contrast-enhancement and brightness constancy properties, which improve the SNR and eliminate variable illumination.

Opponent receptive field results for a laboratory solvent used as a polyimide thinner (section III.4), are shown in Figure 41 through Figure 44. For this image sample, one drop of PI thinner was placed on a swatch of Levis 509 denim blue jeans and allowed to evaporate under ambient laboratory conditions. Six spectral images of the PI thinner specimen were obtained using our breadboard camera and are displayed in Figure 39. Three of the six spectral images were combined to form a RGB pseudo color image; for the results presented below, UV, red, and blue spectral images were selected. To improve the SNR and to allow for a biologically plausible color map, the RGB image was transformed into the YCbCr color space. This transformation process is illustrated in Figure 40.

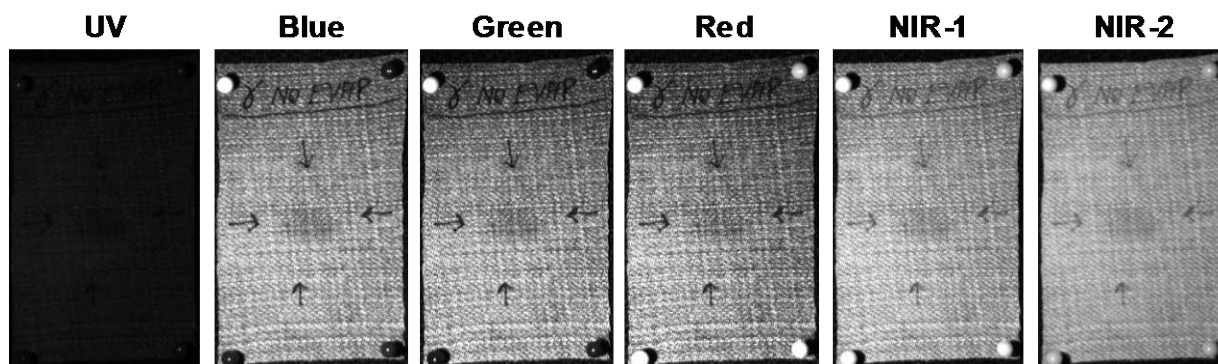


Figure 39: Spectral images of PI thinner.

A drop of PI thinner was placed on a swatch of Levis 509 denim blue jeans and evaporated under ambient laboratory conditions.

The YCbCr color image was then analyzed with our concentric single-opponent and spatially opponent receptive field models. To accomplish this, we mapped the Y (luminance) channel to the blue signal and the two color channels, Cb and Cr, to the red and green signals, respectively. The yellow signal was generated from a linear combination of the red and green signals. For the red-green concentric single-opponent receptive field models in Figure 41, the center-surround operator R^+G^+ and its complement R^-G^- provided the most favorable results. Correspondingly, the R^+R^- center-surround operator and its complement R^-R^+ produced optimal results for the red-green spatially opponent receptive field models in Figure 42. For the blue-yellow concentric single-opponent receptive field models in Figure 43, the best results were obtained from the center-surround operator Y^+B^- and its complement Y^-B^+ . The blue-yellow spatially opponent receptive field models shown in Figure 44 provided only marginal results.

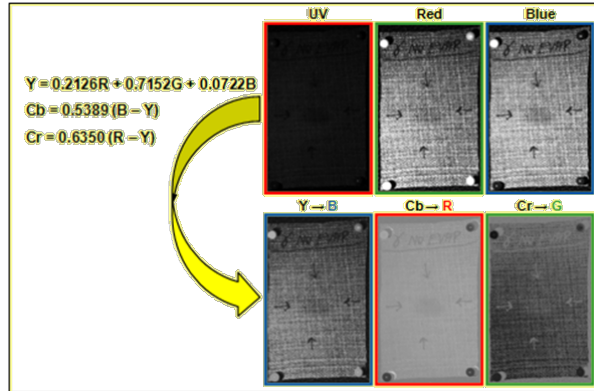


Figure 40: Illustration of RGB to YCbCr color space conversion. The top row represents the spectral band image mapping to RGB image channels. The bottom row shows the YCbCr color space transformation results.

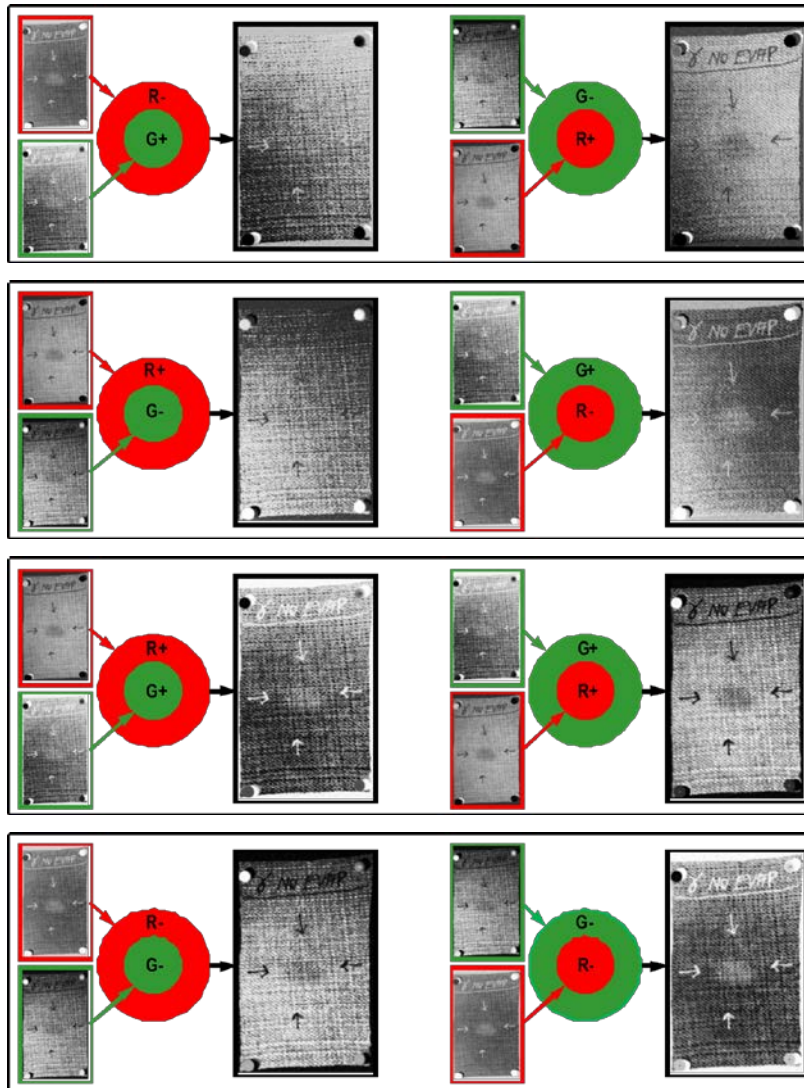


Figure 41: Concentric single-opponent receptive field structures for red-green color signals.

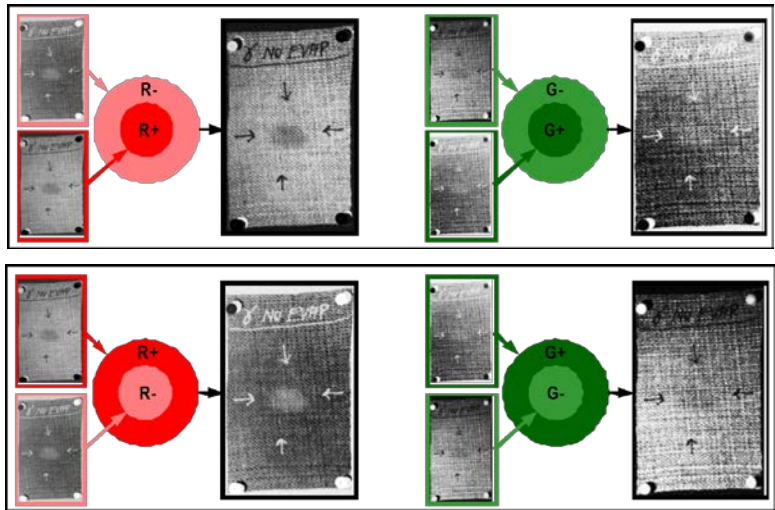


Figure 42: Spatially opponent receptive field structures for red-green color signals.

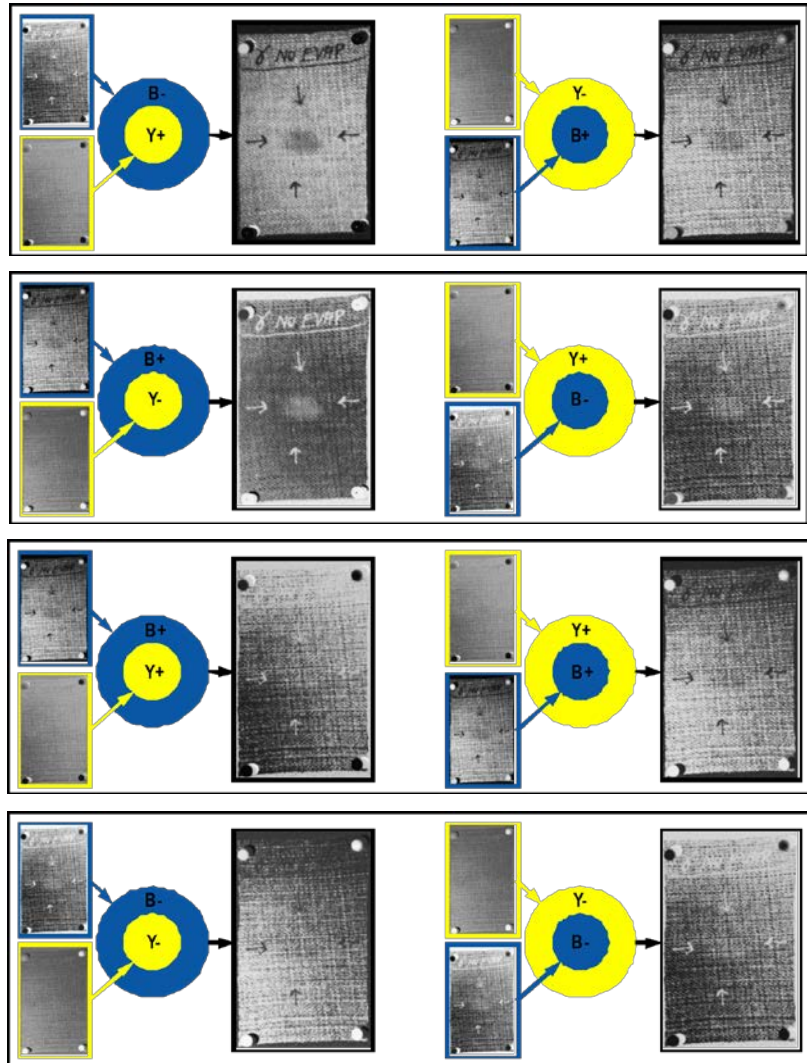


Figure 43: Concentric single-opponent receptive field structures for blue-yellow color signals.

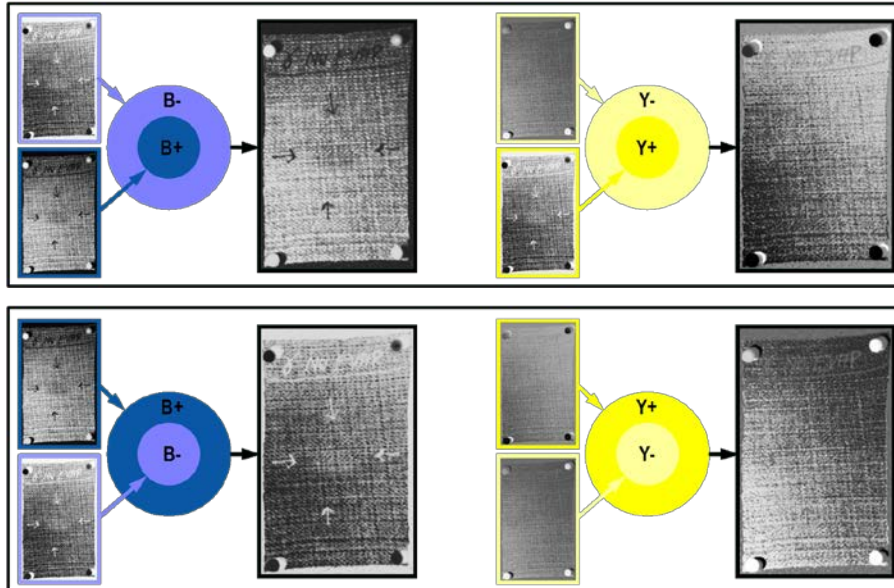


Figure 44: Spatially opponent receptive field structures for blue-yellow color signals.

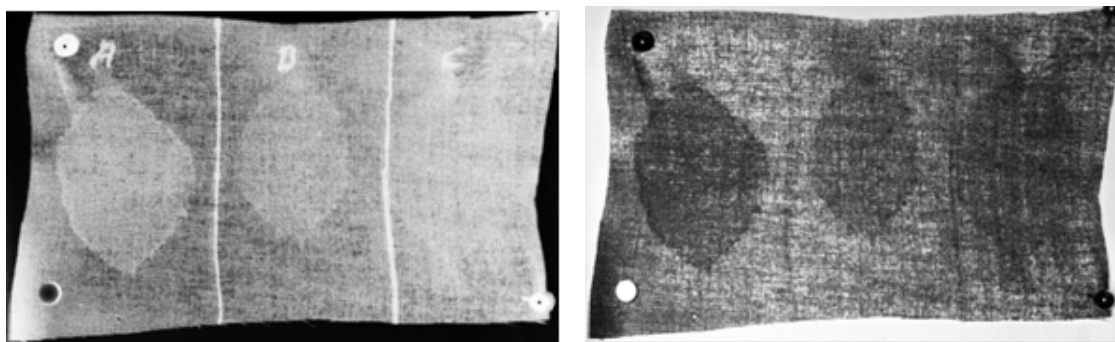


Figure 45: Opponent process applied to bovine blood sample placed on red cotton cloth for UV, Red, and Blue wavelength images: $B+Y-$ (left) and $R+G+$ (right).

IV.3. Three Channel False Color

The human eye is capable of sensing three different primary colors: red, green, and blue. When working with multispectral data, we can take advantage of this capability by treating other spectral bands similarly. That is to say, we can generate false color images to simultaneously display information from three different wavelengths. By combining the spectral signatures into a single image, we can observe differences between spectral bands more easily. Furthermore, we can extend this concept so that false color images represent measurements like the difference in intensity between two or more spectral bands or even the ratio of one spectral band to another.

“False color” generally refers to any image which uses color to represent something other than what would be perceived by an unaided human eye, and comes in many forms [18]. One common method is to pick three different bands of the spectrum, and "map" them to red, green, and blue, in order of descending wavelength (corresponding to the wavelengths relative positions on the electromagnetic spectrum) [19]. There is no “right” or “wrong” way to assign these colors; however, this is considered the most intuitive way to represent the data while maximizing the amount of information conveyed by a single image. When assigning colors, it is important to note that the human eye is not equally sensitive to all three colors; our eyes are most sensitive to green followed by red and then blue. Therefore, for example, slight intensity differences may be more observable when mapped to the green channel as opposed to the blue.

Figure 46 and Figure 47 show results obtained for some of the false color techniques we investigated. Nomenclature used for representing the various false color images is “NIR-R-G” which indicates that the red channel carries the near infrared spectral image, the green channel contains the red spectral image, and the blue channel holds the green spectral image.

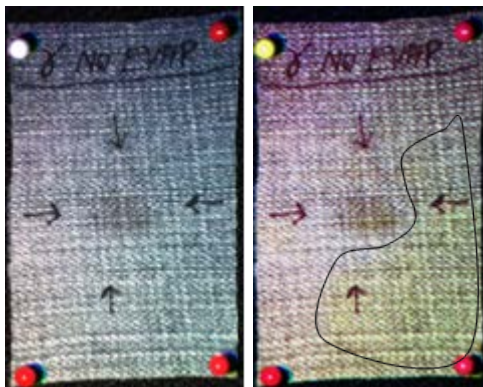


Figure 46: Example of false color image of PI thinner stain on Levis 509 denim blue jeans (III.4. Left image shows the standard R-G-B image. Right image shows the NIR1-R-G false color image. Also notice how the false color image also identifies an additional unknown stain (outlined).

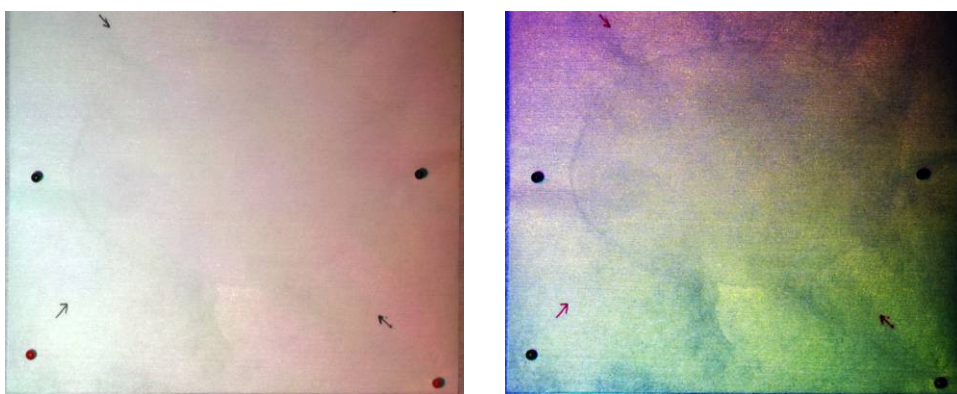


Figure 47: Example of false color image of NaCl stain on a white, clean room cloth. Left image shows the standard R-G-B image. Right image shows the NIR2-R-UV false color image. The outline of the stain is more clearly visible.

IV.4. Spectral Measurements

Multispectral imaging increases our ability to determine the properties of what we see at a distance. It provides a continuous graph of the electromagnetic emission or absorption of materials across different ranges of the electromagnetic spectrum [19]. Each part of the electromagnetic spectrum has its own applications. Because of the proximity of ultraviolet and near infrared spectra to the three primary visible spectra (i.e., blue, green, and red), they can be used to enhance images or provide additional information [19]. For the purposes of this project, we focused our investigation on the utility of using UV (375 nm), blue (470 nm), green (525 nm), red (630 nm), NIR-1 (740 nm), and NIR-2 (870 nm) spectral imagery as a tool for analyzing forensic crime scenes.

The “normalized difference” formula is the basis of an entire branch of the satellite mapping and remote sensing applications in which the amount and/or health of local vegetation or other aspects of the terrain is measured [20]. The normalized difference is calculated between two different spectral bands as:

$$ND(a,b) = \frac{(a - b)}{(a + b)}, \quad (5)$$

Where zero is treated as a threshold with negative values being discarded [20].

Over the years, numerous variations of this equation have been developed and used to detect other environmental characteristics, such as distinguishing between land and water or determining the amount of sediment present in a body of water [20]. The remainder of this section presents some of the standard spectral measurements derived from the normalized difference formula that we investigated.

IV.4.1. TM14 and TM41

TM14 was originally used as a spectral index to calculate variations between different types of rocks and soils [20]. It is defined as the quotient of the blue spectral image divided by the NIR spectral image [20], i.e., $TM14 = blue/NIR$, where division is performed pixel-by-pixel over the entire image. TM41 is the reciprocal of TM14, i.e., $TM41 = NIR/blue$. It was originally used as a spectral index for measuring variations in vegetation and water bodies [20]. Figure 48 shows result of applying TM14 and TM41 to blood samples. Notice how the boundaries of the stains are fairly well defined after applying TM14 and TM41 measures.

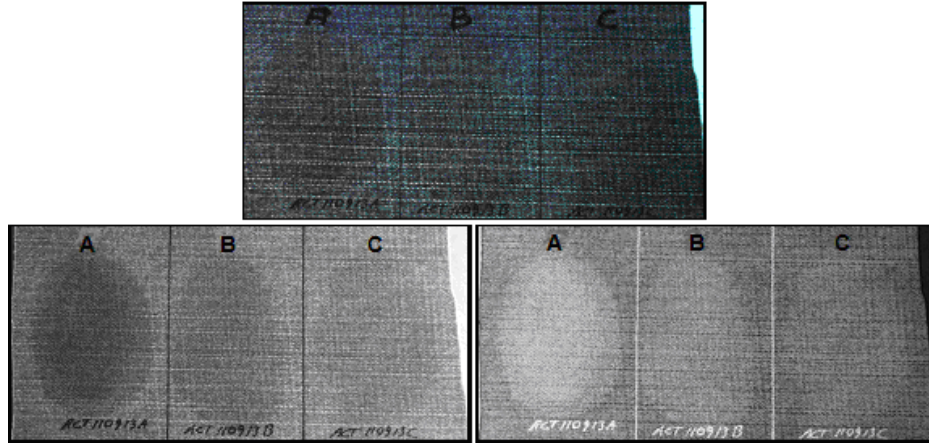


Figure 48: TM14 (bottom left) and TM41 (bottom right) using the NIR-1 spectral image. Bovine blood was placed on a swatch of Levis 509 denim blue jeans at progressively lower concentrations (A, B, and C). Sample A was plainly visible by the unaided eye while samples B and C were only partially visible (top). Notice how the boundaries of the stains are fairly well defined after applying TM14 and TM41 measures.

IV.4.2. ARVI and ASVI

Atmospherically Resistant Vegetation Index (ARVI) and Atmospheric and Soil Vegetation Index (ASVI) are spectral measures originally used to estimate the biomass of successional and mature forests. They are computed as follows [20]:

$$ARVI = \frac{(NIR - 2red + blue)}{(NIR + 2red + blue)} \quad (6)$$

and

$$ASVI = 0.5 + NIR - 0.5\sqrt{(2NIR + 1)^2 - 8(NIR - 2red + blue)} \quad (7)$$

Figure 49 shows the results of applying ARVI and ASVI to a blood sample placed on a swatch of cotton cloth. Notice how the circular pattern of the blood stain's boundary is more pronounced

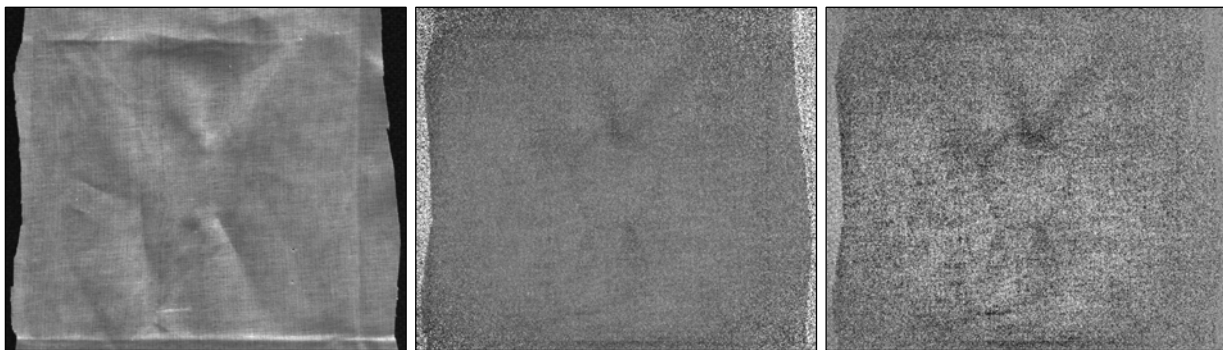


Figure 49: ARVI (middle) and ASVI (right) on the NIR-1 spectral image (left). Sterilized bovine blood was placed on a piece of red cotton cloth. UV was used for illumination. The original sample was difficult to see by the unaided eye (left). Notice how the circular pattern of the blood stain's boundary is more pronounced after applying ARVI and ASVI measures.

after applying ARVI and ASVI measures.

IV.4.3. GEMI and MSAVI

Global Environmental Monitoring Index (GEMI) and Modified Soil-Adjusted Vegetation Index (MSAVI) are spectral measures originally used to estimate the biomass of successional and mature forests. They are computed as follows [20]:

$$GEMI = X_i(1 - 0.25X_i) - \frac{red - 0.125}{1 - red}, \quad (8)$$

where

$$X_i = \frac{2(NIR^2 - red^2) + 1.5NIR + 0.5red}{0.5 + NIR + red} \quad (9)$$

and

$$MSAVI = 0.5 + NIR - 0.5((2NIR + 1)^2 - 8(NIR - 2red)). \quad (10)$$

Figure 50 shows the results of applying GEMI and MSAVI to a sample of NaCl placed on a clean room cloth. Notice how the boundary of the NaCl stain is more visible after applying the GEMI and MSAVI spectral measures.



Figure 50: GEMI (middle) and MSAVI (right) on the NIR-1 spectral band image (left). NaCl solution was placed on a white, clean room cloth and evaporated on a hotplate at 80° C. The stain was not visible by the eye or the digital camera (left). Notice how the boundary of the NaCl stain becomes sharper after applying the GEMI and MSAVI spectral measures.

IV.5. Multispectral Analysis

Spectral imaging can be used to simultaneously image the contents of a crime scene and detect exogenous substances deposited on objects being examined. Under this effort, spectral anomaly detection algorithms were evaluated for their ability and efficiency in finding specific substances deposited on various materials and substrates including latent fingerprints. Anomaly detection is defined as the detection of pixels whose spectral signatures differ significantly from those of the background [21]. The detection algorithms we assessed using data collected with our breadboard camera included: Constrained Energy Minimization (CEM), Generalized Likelihood Ratio Test (GLRT), Adaptive Coherence Estimator (ACE), and Hybrid Unstructured Detector (HUD). The majority of these algorithms are founded in second-order statistics and based on

linear operators such as Fourier analysis, autocorrelation, or power spectrum. Detailed descriptions of additional anomaly detection algorithms can be found in [21], [22], [23] and [24].

IV.5.1. Data Cube and Spectral Vectors

For each data sample under investigation, the six spectral images obtained with the breadboard camera were stacked sequentially in ascending order according to wavelength to form a three-dimensional (3D) data cube consisting of spatial-spatial-spectral dimensions (see Figure 51). This data cube forms a set of spectral vectors, one for each pixel, defined by $\mathbf{x} = [x_1, x_2, \dots, x_K]^T$, where K is the number of spectral bands and T denotes matrix transformation. This set of spectral vectors is then analyzed using the anomaly detection algorithms referred to in the previous paragraph.

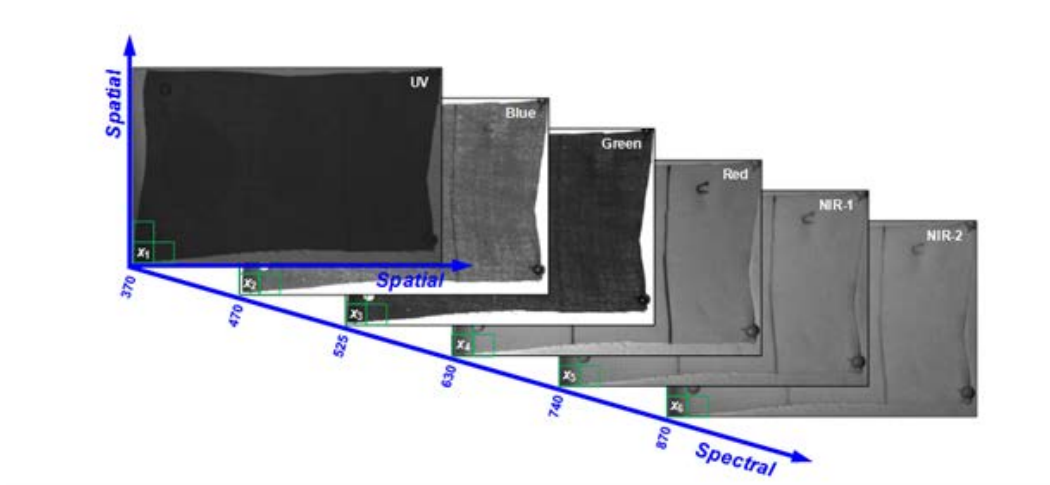


Figure 51: Illustration of spectral data cube and pixel vector.

IV.5.2. Spectral Target Samples

Remote sensing relies on spectral library for description of target of interest. Since spectral libraries were not available, sample spectra were extracted from the data cube to represent target signatures of interest. For each target class, a 10x10 region of pixels were extracted from a data cube and averaged to generate a representative class signature. These signatures were then used in the anomaly detection algorithms to build target models.

Figure 52 shows the location of target samples selected for three different concentrations of bovine blood (left) and two different regions of a latent print (right). Plots illustrating the variability of spectral signatures for target classes across spectral wavelengths are shown in Figure 53 and Figure 54. In these plots, magenta lines represent spectra curves for each sample pixel. Red dashed lines indicate minimum spectra intensities. Blue dash-dot lines symbolize maximum spectra intensities. Black dotted lines represent average spectra values while green lines signify median values. These measurements are shown to illustrate the variability of the spectral signatures. The mean spectral values (black dotted line) of the selected pixels are used to represent the “target pixel”.

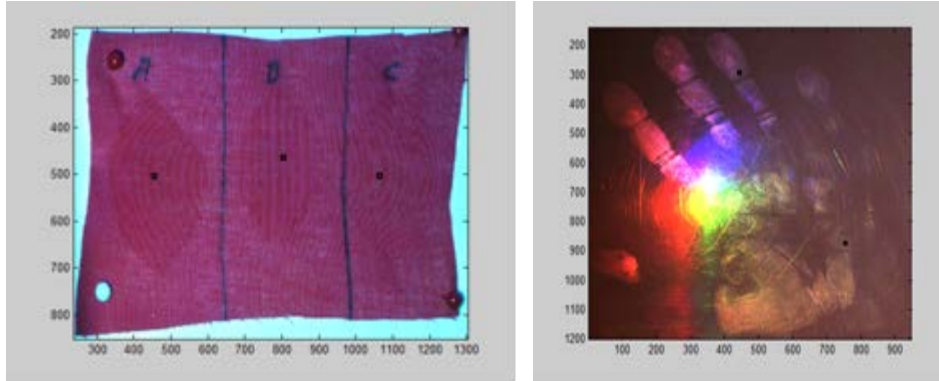


Figure 52: Locations of sample spectra for target classes, indicated by the black dots. Left image shows the location of samples for three different concentrations of bovine blood placed on red cotton material. Right image shows the location of samples for palm and fingerprints transferred onto an opaque nylon polymer sheet.

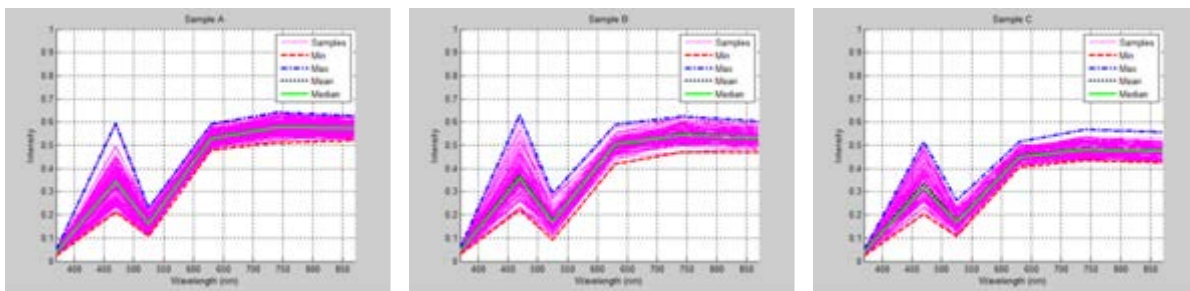


Figure 53: Example plots illustrating spectral signature variability for blood samples across all wavelengths
Sample A (left), Sample B (center), and Sample C (right).

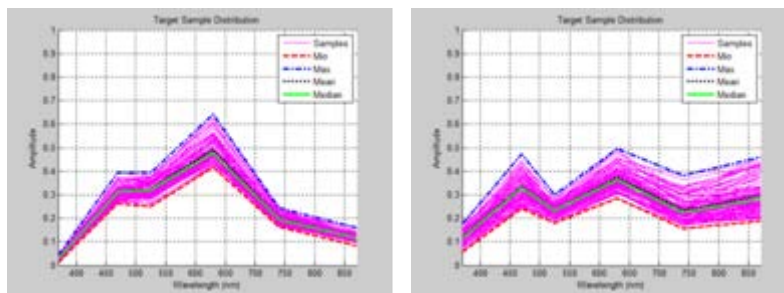


Figure 54: Example plots illustrating spectral signature variability for latent print samples across all wavelengths.
Left plot represents samples taken from the palm region. Right plot shows the distribution of samples taken from a fingerprint region that was laced with potato chip oil from handling the chips by the fingers.

IV.5.3. Anomaly Detection Algorithms

Using the target signatures presented in Section IV.5.2, we evaluated several anomaly detection algorithms to determine their effectiveness in isolating similar signatures within

imagery collected with our breadboard camera. The following subsections provide a brief description of each algorithm and presents detection results (spectral measurement spaces) obtained for blood and latent prints.

IV.5.3.1. Constrained Energy Minimization (CEM)

Constrained Energy Minimization (CEM) is designed as a finite impulse response filter that allows the desired target to pass through while minimizing its output energy resulting from background other than the desired targets [25]. A correlation or covariance matrix is used to characterize the composite unknown background. This technique maximizes the response of the known signature and suppresses the response to the composite unknown background, thus matching the known target signature. The CEM detector is expressed as:

$$CEM(x) = \frac{d^T R^{-1} x}{d^T R^{-1} d}, \quad (11)$$

where d is the target spectrum, x is the pixel spectrum, and R is the background correlation or covariance matrix. Note, that for demeaned data, the correlation matrix is the same as the covariance matrix.

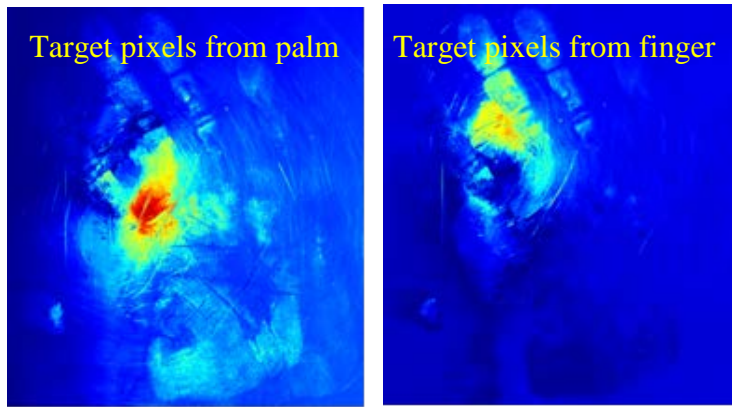


Figure 55: CEM spectral measurement space for latent palm and fingerprints. Left image was obtained using target pixels from the palm region. Right image was obtained using target pixels from finger region. The spectral differences in the signature were identified by CEM. In this case, the fingers had oil from handling food which may have resulted in some spectral differences.

IV.5.3.2. Generalized Likelihood Ratio Test (GLRT)

The Generalized Likelihood Ratio Test (GLRT) is used in many anomaly detection algorithms as local normal, normal mixture, and joint exploitation models. The decision rule is based on a generalized maximum likelihood ratio test where conditional densities that constitute the likelihood ratio are maximized over unknown parameters [26]. The unknown parameters are estimated from test and reference data. GLRT postulates a reference data set modeled as a normal distribution of mean μ and covariance Σ :

$$\begin{aligned} H_0 : x &= N(\mu, \Sigma_x) \\ H_1 : x &= N(\mu_s, \Sigma_x) \end{aligned} \quad (12)$$

such that μ_s and Σ_x are unknown and x is the observation vector under test. The GLRT is then defined as:

$$GLRT(x) = (x - \mu)^T \left(\frac{N}{N+1} \Sigma_x + \frac{1}{N+1} (x - \mu)(x - \mu)^T \right)^{-1} \times (x - \mu) \underset{H_0}{\overset{H_1}{>}} \eta, \quad (13)$$

where $(\cdot)^T$ represents the transpose, N is the number of samples, $\Sigma_x = \frac{1}{N} \sum_{j=1}^N (v_j - \mu)(v_j - \mu)^T$ is the sample covariance matrix of the reference data, and η is a threshold [26].

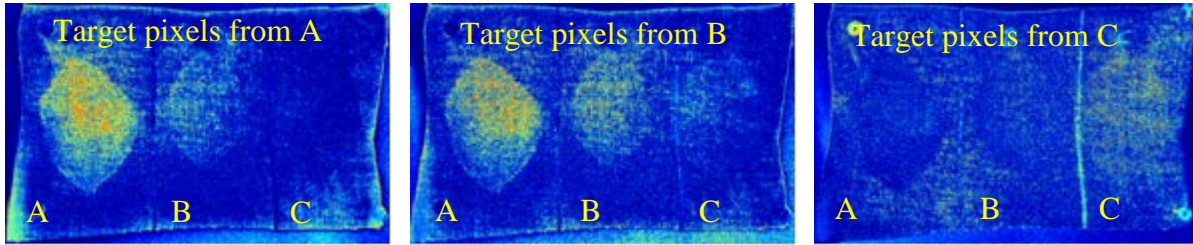


Figure 56: GLRT spectral measurement space for blood samples on red cloth (III.3). Left image was obtained using sample A target pixels. Center image was obtained using sample B target pixels. Right Image was obtained using sample C target pixels. Note that when sample A pixels and sample C pixels were used only like pixels were enhanced. However, when sample B pixels were used as target pixels, both B and A pixels were enhanced. Although GLRT was not able to accurately distinguish between blood samples A and B, it was able to distinguish between A/B and C as well as blood from non-blood pixels.

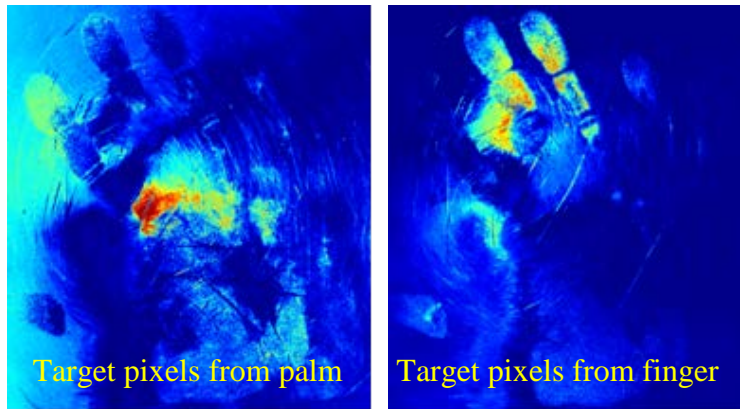


Figure 57: GLRT spectral measurement space for latent palm and fingerprints. GLRT also identified spectral differences between palm and fingers

IV.5.3.3. Adaptive Coherence Estimator (ACE)

The Adaptive Coherence Estimator (ACE) detector is derived from the Generalized Likelihood Ratio (GLR) detector, and is defined as:

$$ACE(x) = \frac{(d^T \Sigma^{-1} x)^2}{(d^T \Sigma^{-1} d)(x^T \Sigma^{-1} x)}, \quad (14)$$

where d is the target spectrum, x is the pixel spectrum, and Σ is the background covariance matrix. ACE is invariant to relative scaling of test and training data and has a Constant False Alarm Rate (CFAR) with respect to such scaling [27]. ACE uses a different method to stretch the detection statistic and achieve greater target to background separation. Similar to CEM, ACE provides a rapid means of detecting a specific target signature based on matches to library or image endmember spectra and does not require knowledge of all the endmembers within an image scene.

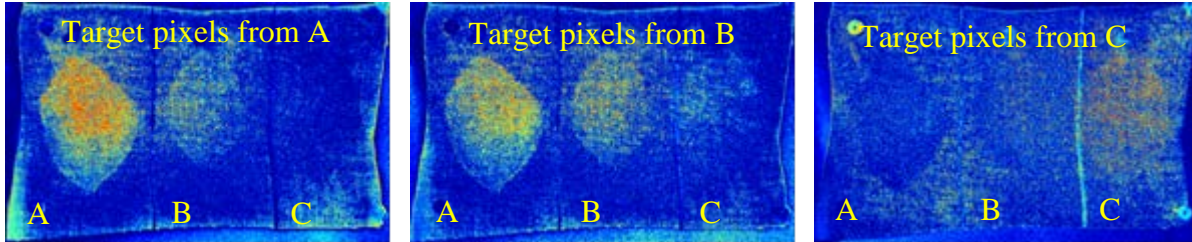


Figure 58: ACE spectral measurement space for blood samples. As in GLRT, when sample A and C pixels are used as target pixels only like pixels are enhanced but when sample B pixels were used as target pixels, both B and A pixels were enhanced. ACE was not able to accurately distinguish the two highest concentration stains A and B, it was able to distinguish them from the least concentration C as well as from non-blood stain pixels.

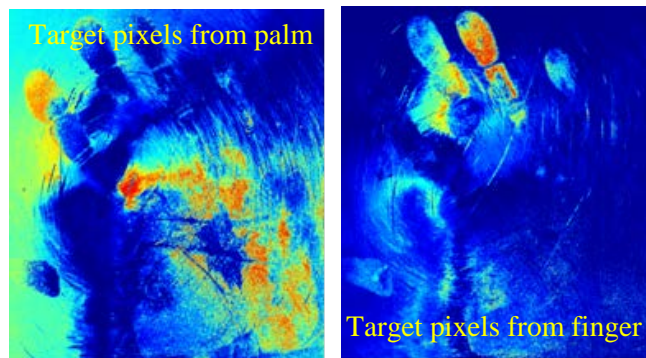


Figure 59: ACE spectral measurement space for latent palm and fingerprints. ACE produced results similar to other spectral analyses

IV.5.3.4. Hybrid Unstructured Detector (HUD)

The Hybrid Unstructured Detector (HUD) models the background as a multivariate normal distribution similar to ACE, and is defined as:

$$HUD(x) = \frac{x^T \Sigma^{-1} Sa}{x^T \Sigma^{-1} x} \quad (15)$$

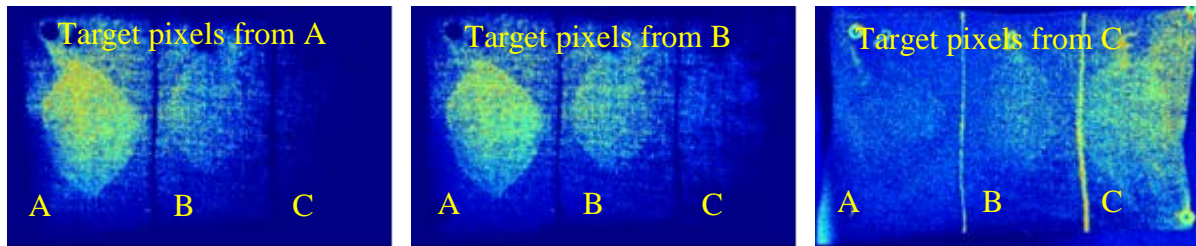


Figure 60: HUD spectral measurement space for blood samples. As in other multispectral analyses, HUD was not able to accurately distinguish the two highest concentration stains A and B, it was able to distinguish them from the least concentration C as well as from non-blood stain pixels.

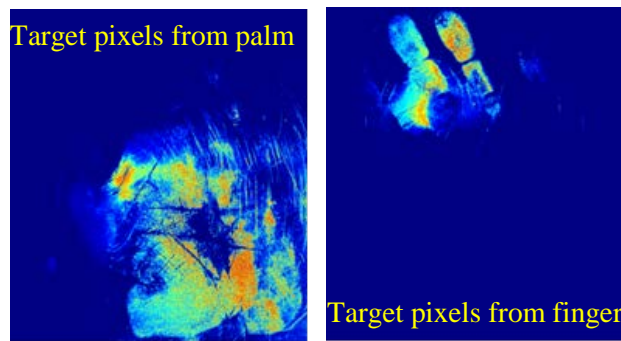


Figure 61: HUD spectral measurement space for latent palm and fingerprints. HUD produced the most enhanced images of spectral differences between palm and fingers

IV.6. Frequency Subband Filtering

To improve ridge information contained in fingerprint images, we investigated texture features founded in the frequency domain. The frequency domain analysis can provide a useful source of information with respect to texture granularity and directionality, both of which are common traits associated with ridge and valley structures present in fingerprints. Characteristics such as these can be described by the output of subband filters that vary in terms of center-frequency, bandwidth, and orientation.

The principle behind subband filtering is that certain characteristics of signals in the spatial domain such as periodicity are quite distinctive in the frequency or Fourier domain. Fingerprint images containing texture information varying in orientation and frequency will contain different amounts of energy for certain subband filters. Wilson and Spann [28,29] proposed a set of operations, *quadrant* and *center-surround*, to subdivide the frequency domain of an image into smaller regions, which span the whole frequency spectrum. The quadrant operator divides the frequency domain into four quadrants while the center-surround operator splits it into an inner square region and a surrounding annulus as shown in Figure 62. These operators are combined to construct different tessellations of the frequency space whereby forming a Second Orientation Pyramid (SOP) illustrated in Figure 62. A description of SOP subband filtering process follows.

A spectral data volume, V , whose centered Fourier transform is $V_\omega = \mathfrak{F}[V]$ is subdivided into a set of i regions $L_r^i \times L_c^i \times L_d^i$, where $L_r^i = \{r, r+1, \dots, r+N_r^i\}$, $1 \leq r \leq N_r - N_r^i$, $L_c^i = \{c, c+1, \dots, c+N_c^i\}$, $1 \leq c \leq N_c - N_c^i$, and $L_d^i = \{d, d+1, \dots, d+N_d^i\}$, $1 \leq d \leq N_d - N_d^i$, which follow the conditions:

$$L_r^i \subset L_r, \sum_i N_r^i = N_r,$$

$$L_c^i \subset L_c, \sum_i N_c^i = N_c,$$

$$L_d^i \subset L_d, \sum_i N_d^i = N_d,$$

$$(L_r^i \times L_c^i \times L_d^i) \cap (L_r^j \times L_c^j \times L_d^j) = \{\phi\}, i \neq j.$$

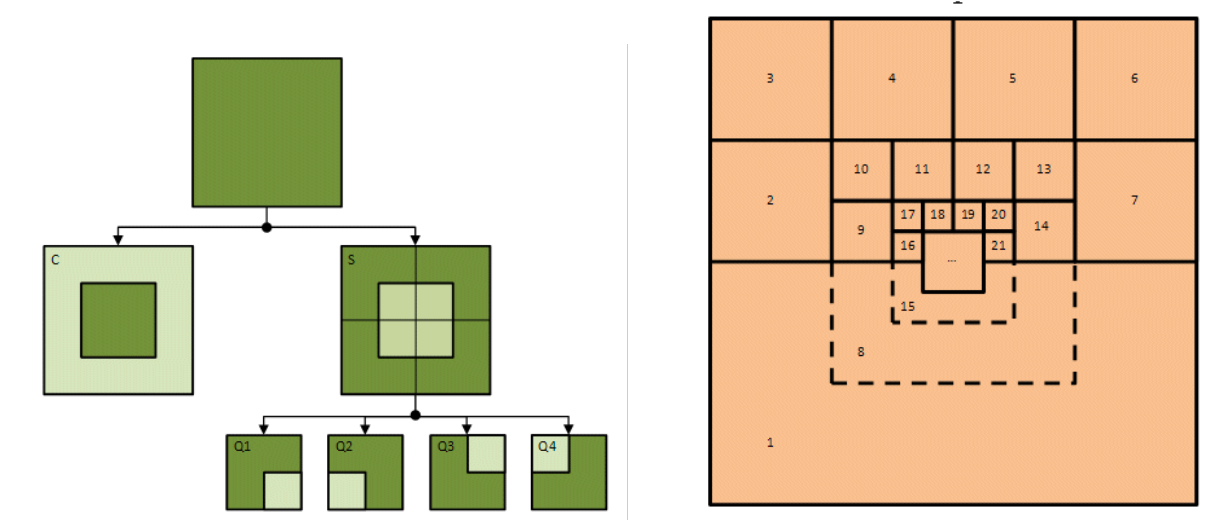


Figure 62: Second orientation pyramid
 Quadrant and center-surround tessellation operators (left). Third order Second Orientation Pyramid structure for a 2D image (right).

The SOP tessellation process involves a set of 7 filters in 2D: one for the low pass region and 6 high pass regions. In 3D, the tessellation consists of a total of 29 filters: 28 for the high pass regions and one for the low pass region. In the Fourier domain, the i -th filter, F_ω^i , is related to the i -th subdivision of the frequency domain as:

$$F_{\omega}^i = \begin{cases} L_r^i \times L_c^i \times L_d^i & \rightarrow G(\mu^i, \Sigma^i) \\ (L_r^i \times L_c^i \times L_d^i)^c & \rightarrow 0 \end{cases} \quad \forall i \in SOP, \quad (16)$$

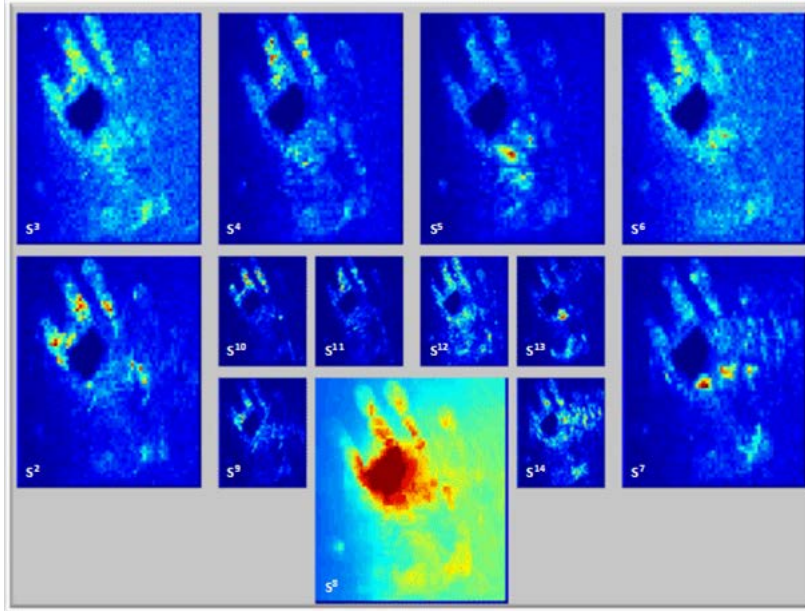
where G is a band-limited Gaussian function (filter) with parameters μ^i the center of region i and Σ^i the co-variance matrix. For the first order of the SOP, one of the filters will contain the low pass or *center* of the region being analyzed, V_{ω} , and the other six (2D) or twenty-eight (3D) remaining filters will subdivide the high pass bands of the *surround* of the region. As an example for the 2D case, this would be:

$$\text{Center } F^1 : L_r^1 = \left\{ \frac{N_r}{4} + 1, \dots, \frac{3N_r}{4} \right\}, L_c^1 = \left\{ \frac{N_c}{4} + 1, \dots, \frac{3N_c}{4} \right\}$$

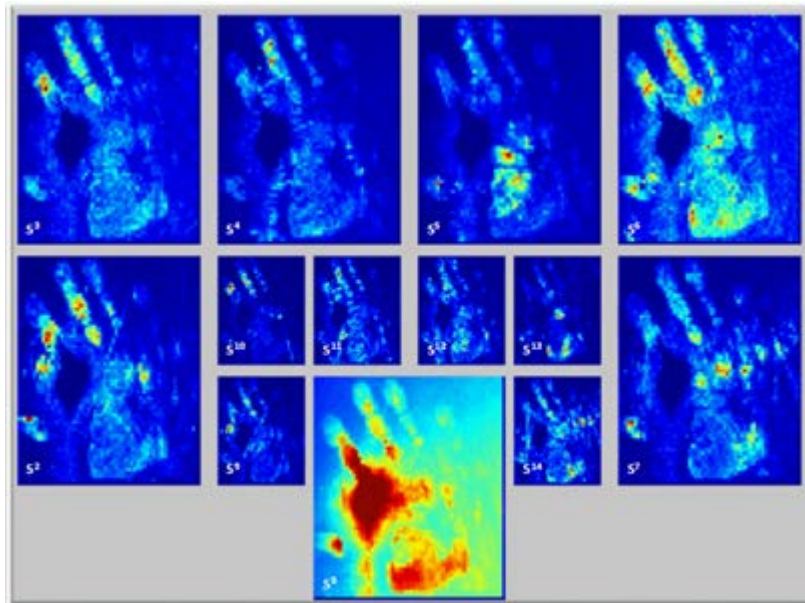
$$\begin{aligned} \text{Surround } F^{2-7} : L_r^{3,4,5,6} &= \left\{ 1, \dots, \frac{N_r}{4} \right\}, L_r^{2,7} = \left\{ \frac{N_r}{4} + 1, \dots, \frac{N_r}{2} \right\}, \\ L_c^{2,3} &= \left\{ 1, \dots, \frac{N_c}{4} \right\}, L_c^4 = \left\{ \frac{N_c}{4} + 1, \dots, \frac{N_c}{2} \right\}, L_c^5 = \left\{ \frac{N_c}{2} + 1, \dots, \frac{3N_c}{4} \right\} \\ L_c^{6,7} &= \left\{ \frac{3N_c}{4} + 1, \dots, N_c \right\} \end{aligned}$$

At the next level, the region to be subdivided will be the center region of order 1 with coordinates $(L_r^1(1) \times L_c^1(1) \times L_d^1(1))$ which will then become $(L_r(2) \times L_c(2) \times L_d(2))$ with dimensions $N_r(2) = N_r(1)/2$, $N_c(2) = N_c(1)/2$, and $N_d(2) = N_d(1)/2$ or in general for any order o $N_{r,c,d}(o+1) = N_{r,c,d}(o)/2$. It is assumed that $N_r(1) = 2^a$, $N_c(1) = 2^b$, and $N_d(1) = 2^c$ so that the results of the divisions are always integer values. The next set of filters is calculated recursively. For the 2D case, this would be: $L_r^8(1) = L_r^1(2)$, $L_c^8(1) = L_c^1(2)$, $L_r^9(1) = L_r^2(2)$, etc.

The measurement space generated by each filter contains the same number of pixels as the original image and thus can be used as features for texture analysis and classification tasks. An example of the measurement space of the first two orders of the SOP for blue (470 nm wavelength) and red (630 nm wavelength) spectral band images of latent handprints that were applied onto an opaque nylon polymer sheet are given in Figure 63. In this example, notice the high pass nature present in all orientations for random noise-like patterns while oriented patterns concentrate their energy in only some regions, mainly lower frequencies.



(a) Blue spectral band image.



(b) Red spectral band image.

Figure 63: SOP first and second order measurement spaces for blue and red spectral band images of latent handprints.

Each measurement space, S_i , is placed in the position corresponding to its filter, F_i . Notice how certain textures are highlighted in different frequency sub bands.

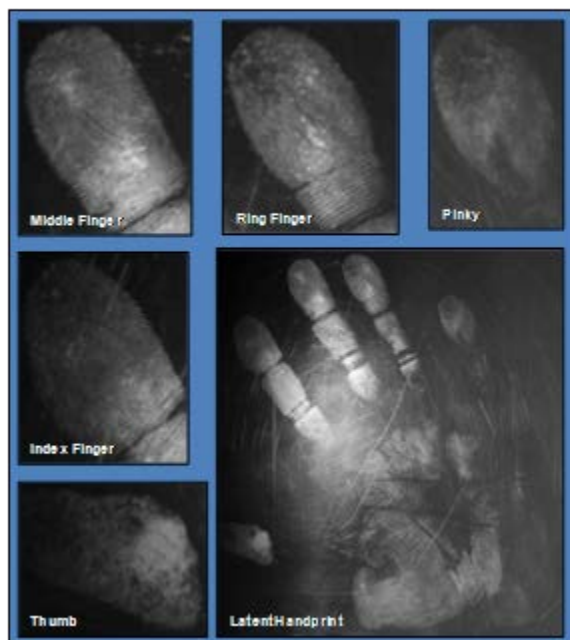


Figure 64: Image generated from accumulating the SOP first and second order measurement spaces of all six spectral images

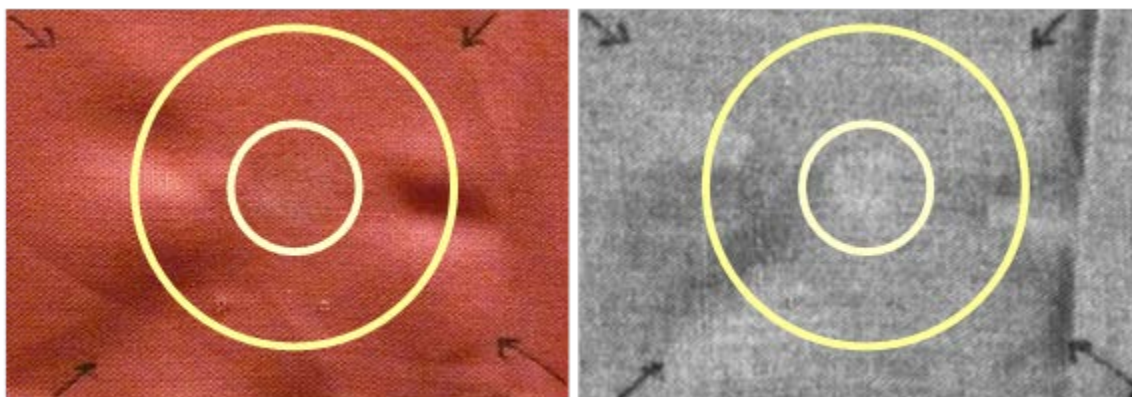


Figure 65: SOP result for Sudafed solution.

1mL of a 1.5% Sudafed solution was on a red cotton cloth evaporated using a hotplate. A small (about 1 cm diameter) circular region is clearly visible in the accumulated 2nd order SOP across all six spectral images (right) but only slightly visible in the ground truth color photo (left). In addition, a larger circular region that circumscribes the smaller one is slightly visible SOP image yet invisible in the color photo.

IV.7. Steerable Filter

In many computer vision and image processing tasks, such as texture analysis, edge detection, and image enhancement, it is often useful to apply oriented filters and then examine the filter output as a function of orientation (angle) and phase. Steerable filters are an adaptive technique used to efficiently generate arbitrary oriented filters by applying a small number of

filters corresponding to a few angles and then interpolating between the responses. More specifically, the term “steerable filter” is used to describe a class of filters in which a filter of arbitrary orientation and phase is synthesized as a linear combination of a set of “basis filters” [30]. Given the correct filter set and interpolation rule, we can determine the response of the arbitrarily oriented filter without actually applying the filter, and then use its response to evaluate the directional derivatives of latent fingerprints.

For our implementation, consider the two-dimensional, circularly symmetric Gaussian function G defined as:

$$G(x, y) = \frac{1}{\sqrt{2\pi}} e^{-\frac{1}{2}\left(\frac{x^2}{\sigma_x^2} + \frac{y^2}{\sigma_y^2}\right)}. \quad (17)$$

Let G_n represent the n th derivative of a Gaussian in the x direction. Now, Let $(\cdot)^\theta$ represent the rotation operator for any function $f(x, y)$, such that $f(x, y)^\theta$ is $f(x, y)$ rotated through an angle θ about the origin. The first x derivative of a Gaussian $G_1^{0^\circ}$ is then defined as:

$$G_1^{0^\circ} = \frac{\partial}{\partial x} \frac{1}{\sqrt{2\pi}} e^{-\frac{1}{2}\left(\frac{x^2}{\sigma_x^2} + \frac{y^2}{\sigma_y^2}\right)} = -\frac{1}{\sigma_x^2 \sqrt{2\pi}} x e^{-\frac{1}{2}\left(\frac{x^2}{\sigma_x^2} + \frac{y^2}{\sigma_y^2}\right)}. \quad (18)$$

The same function rotated 90° is

$$G_1^{90^\circ} = \frac{\partial}{\partial y} \frac{1}{\sqrt{2\pi}} e^{-\frac{1}{2}\left(\frac{x^2}{\sigma_x^2} + \frac{y^2}{\sigma_y^2}\right)} = -\frac{1}{\sigma_y^2 \sqrt{2\pi}} y e^{-\frac{1}{2}\left(\frac{x^2}{\sigma_x^2} + \frac{y^2}{\sigma_y^2}\right)}. \quad (19)$$

A G_1 filter for an arbitrary orientation θ is then synthesized by taking a linear combination of $G_1^{0^\circ}$ and $G_1^{90^\circ}$ (i.e., sum of rotated versions of itself) as follows:

$$G_1^\theta = G_1^{0^\circ} \cos(\theta) + G_1^{90^\circ} \sin(\theta). \quad (20)$$

Since $G_1^{0^\circ}$ and $G_1^{90^\circ}$ span the set of G_1^θ filters, they are called basis filters for G_1^θ , and the $\cos(\theta)$ and $\sin(\theta)$ terms are the interpolation functions for the basis filters.

Figure 66 shows an example of applying the steerable filter defined above on an image of a latent handprint that was transferred onto an opaque nylon polymer sheet. For this example, we obtained a linear combination of steerable filter responses for $\theta = \{0, 3, \dots, 180\}$ and $\sigma_x = \sigma_y = 0.5$ for each of the spectral band images: UV (375 nm), blue (470 nm), green (525 nm), red (630 nm), NIR-1 (740 nm), and NIR-2 (870 nm). Notice the enhanced detail of the fingerprints provided by the steerable filters.

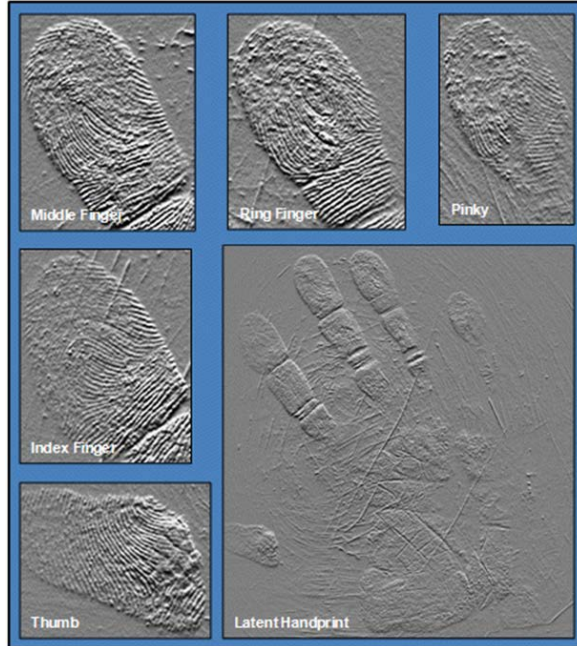


Figure 66: Image generated from combining steerable filter (multi-orientation) We obtained a linear combination of steerable filter responses for $\theta = \{0^\circ, 3^\circ, \dots, 180^\circ\}$ and $\sigma_x = \sigma_y = 0.5$ for each of the spectral band images: UV (375 nm), blue (470 nm), green (525 nm), red (630 nm), NIR-1 (740 nm), and NIR-2 (870 nm). Notice the enhanced detail provided by the steerable filters of the zoomed in regions of the fingerprints.

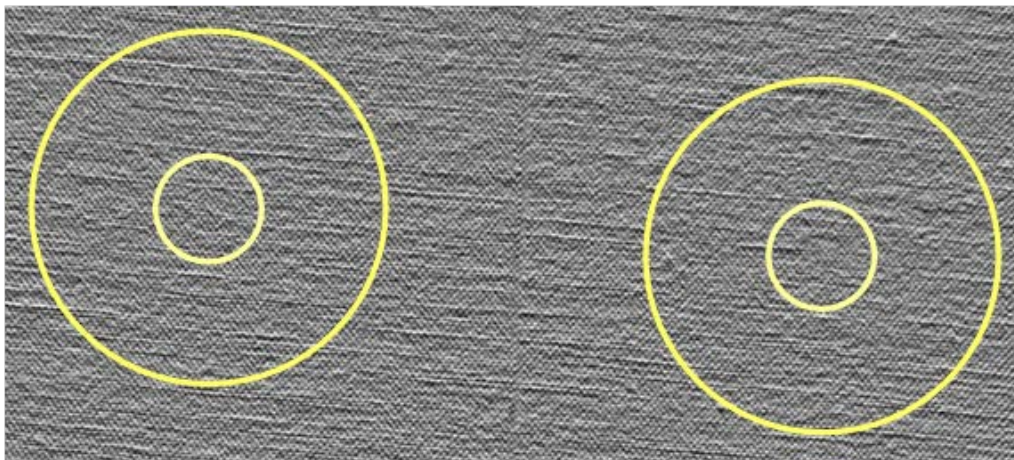


Figure 67: Steerable filter results for PI thinner.

A drop of PI thinner was placed onto two separate regions of a swatch of red, 100% cotton cloth. On the left, the PI thinner was evaporated using a hotplate at 100° C. On the right, the PI thinner was allowed to evaporate under ambient laboratory conditions. Neither stain was visible to the unaided eye. The steerable filter image was obtained by accumulating results across all six spectral bands: UV, blue, green, red, NIR-1, and NIR-2. Notice how the steerable filters were able to enhance the imprint that resulted from the impact of the drop on the cotton cloth for both samples. These regions are annotated by the small yellow circles. The large circles show the vaguely perceived outer boundary of the stain.

IV.8. Fusion via Multi-scale, Multi-orientation Steerable Pyramid

During the course of this project, we investigated the utility of Teledyne’s multi-resolution image fusion approach previously developed for hyperspectral data enhancement and information reduction applications. Our fusion algorithm extracts and combines complementary information from different spectral wavelengths to form a single composite image by means of a steerable pyramid [31] and saliency and match measures introduced by Burt et al. [32] The steerable pyramid provides a multi-scale, multi-orientation architecture for image enhancement while saliency and match measures provide the mechanisms for information extraction and fusion.

Our multi-scale, multi-orientation fusion approach decomposes each spectral source image into a multi-level pyramid via steerable pyramid decomposition, where a filter enhanced and recursively subsampled version of the original image resides at each level. Pattern selection is performed at each decomposition level to select and combine complementary information from the source images to form a composite pyramid. The value at a given position within the pyramid is assigned the value of the corresponding enhanced and subsampled source image that has the highest “saliency”. This enables the pattern selection process to choose the more structurally, well-defined source to build the composite image. Upon completion of the composite pyramid, an inverse pyramid transform is then performed to reconstruct a single composite spectral image.

Figure 68 illustrates how image fusion can be used to aid latent print analysis specifically in situations where varying signatures are detectable at different spectral wavelengths. In this

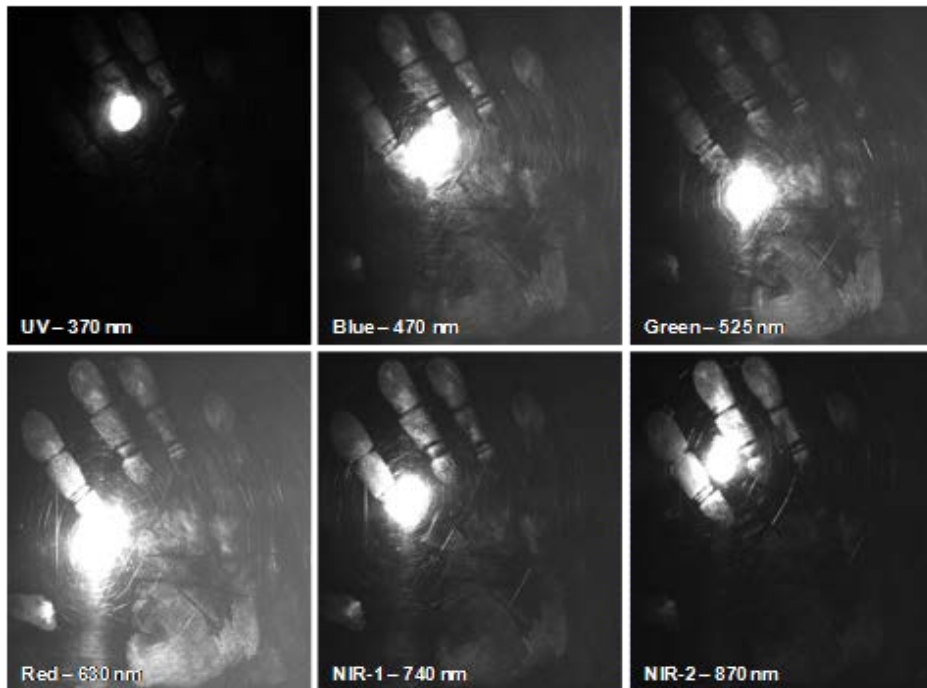


Figure 68: Example of how information can vary across spectral wavelengths.

example, an individual handled potato chips with his fingertips prior to touching an opaque nylon polymer sheet. Notice how the various spectral wavelengths highlight or detect different regions of the latent handprint. By applying our image fusion algorithm, we can obtain a single image that contains the most salient information from each of the six spectral images whereby allowing us to focus our analysis on a single image as opposed to six individual images.

Figure 69 shows the composite image obtained from our multi-scale, multi-orientation, steerable pyramid fusion process applied to UV, Blue, Green, Red, NIR-1, and NIR-2 spectral images of a latent handprint. Notice how the detail of the fingerprints in the fused image is significantly enhanced when compared to a simple summation of the individual spectral images.

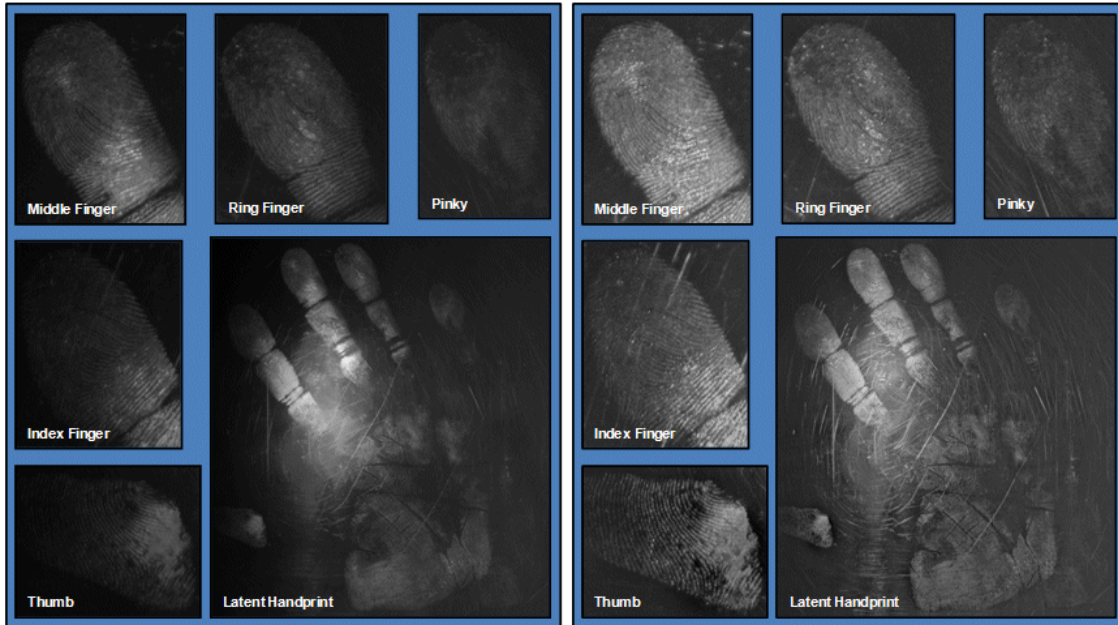


Figure 69: Composite image generated via the multi-scale, multi-orientation steerable pyramid fusion of six spectral bands.

The image on the left was generated via a pixel-by-pixel summation of all six spectral band images. The right image is the multi-resolution fused image. Notice how the steerable pyramid fusion process significantly enhanced fingerprint details.

IV.8.1. Steerable Pyramid

The steerable pyramid is a multi-scale, multi-orientation image decomposition that linearly subdivides an image into a collection of subbands localized in both scale and orientation. Scale and orientation are tuned by a set of directional derivative basis functions. The number of orientations is adjusted by changing the derivative order (e.g., first derivatives yield two orientations). A polar-separable decomposition performed in the frequency domain provides an independent representation of scale and orientation that is also translation and rotation invariant.

Figure 71 shows the system diagram of the recursive construction of the steerable pyramid. First, the source image is separated into lowpass and highpass subbands via lowpass and highpass filters in preparation for the recursion process. Next, the lowpass subband image is divided into a set of oriented bandpass subbands and a lower-pass subband using steerable bandpass filters. The magnitude of the i^{th} oriented bandpass filter is defined as:

$$B_i(\vec{\omega}) = A(\theta - \theta_i)B(\omega) , \quad (21)$$

where $B(\omega)$ is the decomposition radial function, $A(\theta)$ is the decomposition angular function determined by the derivative order, $\theta = \tan^{-1}(\omega_y / \omega_x)$, $\theta_i = 2\pi / k$, and $\omega = |\vec{\omega}|$. The lower-pass subband images are then subsampled by a factor of two in both the x and y directions. The recursive construction of the steerable pyramid is achieved by inserting a copy of the lower-pass subband image at its corresponding level in the pyramid (denoted by the solid circle in Figure 71). Figure 70 illustrates the idealized frequency response of a steerable pyramid with three scale levels and three basis orientations (i.e., $k = 3$).

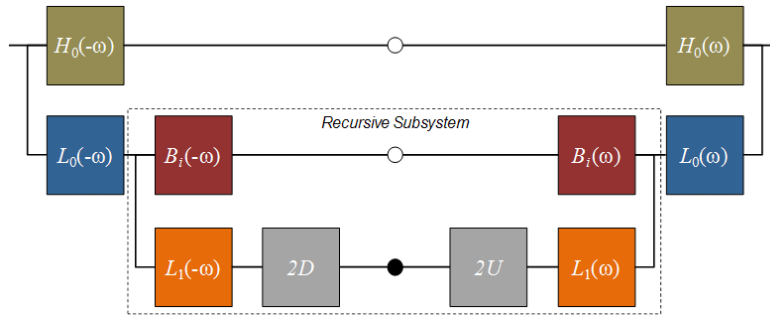


Figure 70: System diagram illustrating the filtering and sampling operations and recursive construction of the steerable pyramid.

Boxes labeled $2D$ and $2U$ correspond to downsampling and upsampling by a factor of 2. The circles correspond to the transform coefficients. The solid circle represents the recursive construction of the pyramid.

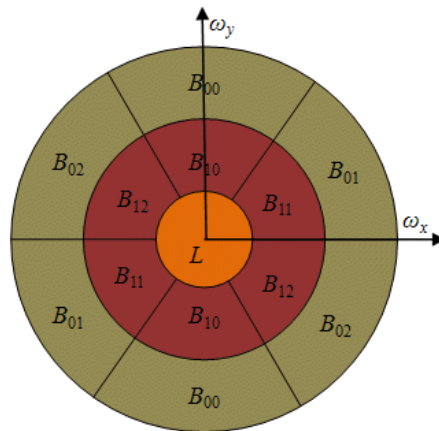


Figure 71: Idealized frequency response of the decomposition into scale and orientation subbands for a 3-level, 3-direction steerable pyramid.

The basis functions are related by translations, dilations, and rotations.

IV.8.2. Image Fusion

The image fusion process is guided by two measures: 1) a salience measure that decides which source pixel is picked during the selection process, and 2) a match measure that determines whether selection or averaging is used to insert source pixels into the composite pyramid. We define salience at a pixel (m,n) within a neighborhood p as:

$$S(m,n) = \sum_{m,n \in p(m,n)} C_I^2(m+m',n+n') , \quad (22)$$

where D_I is the steerable pyramid transform of the image $I(m,n)$ and C_I is the local energy or variance within a pixel neighborhood of D_I . Similarly, we define the match measure as the local zero-mean normalized cross correlation within a pixel neighborhood:

$$M_{AB}(m,n) = \frac{\sum_{m,n \in p(m,n)} D_A^2(m+m',n+n') D_B^2(m+m',n+n')}{\sqrt{S_A(m,n) S_B(m,n)} + \varepsilon} . \quad (23)$$

If a match measure between images is low for a given position, then the pixel value from the source pyramid with the highest salience is inserted into the composite pyramid. If the match measure is high, then the source values are averaged as follows:

$$D_C(m,n) = w_A(m,n) D_A(m,n) + w_B(m,n) D_B(m,n) , \quad (24)$$

Where w_A and w_B are assigned weights determined by the value of M_{AB} . At each pixel (m,n) , if $M_{AB} \leq \alpha$, then $w_{\min} = 0$ and $w_{\max} = 1$, else if $M_{AB} \geq \alpha$, then

$$w_{\min} = \frac{1}{2} - \frac{1}{2} \left(\frac{1 - M_{AB}}{1 - \alpha} \right) \text{ and } w_{\max} = 1 - w_{\min} . \quad (25)$$

In addition, the source image to which the weights are assigned is dependent on the image with the largest salience. If $S_A > S_B$, then $w_A = w_{\max}$ and $w_B = w_{\min}$, else $w_A = w_{\min}$ and $w_B = w_{\max}$.

IV.9. Gabor Filter Based Fingerprint Enhancement

Using the results from the steerable pyramid as the starting point, we studied Gabor filter based fingerprint image enhancement method proposed by Hong [33]. To improve the ridge and valley structure, the method estimates the local ridge orientation and frequency, and then applies a Gabor filter of proper frequency and orientation to the image.

It first applies a gradient operator on the image and then estimates the local orientation on a small window using Rao's method [34]. The local ridge orientation at pixel location (i,j) , $\theta(i,j)$, is estimated using Equation 26 through 28, in which hw is half of the window size, and $\partial_x(u,v), \partial_y(u,v)$ represent the gradient in the x, y direction respectively. This estimated orientation value is further smoothed in a larger window to filter noisy estimation.

$$V_x(i,j) = \sum_{u=i-hw}^{i+hw} \sum_{v=j-hw}^{j+hw} 2\partial_x(u,v)\partial_y(u,v) \quad (26)$$

$$V_y(i,j) = \sum_{u=i-hw}^{i+hw} \sum_{v=j-hw}^{j+hw} 2\partial_x^2(u,v)\partial_y^2(u,v) \quad (27)$$

$$\theta(i, j) = \frac{1}{2} \tan^{-1} \left(\frac{V_y(i, j)}{V_x(i, j)} \right) \quad (28)$$

Secondly, the local frequency is estimated as well by rotating the small image in the window for the angle of the estimated local orientation so that the local ridge is in the y direction in the new image. An x-signature is obtained by calculating the average value of each column. Figure 72 shows the original small image along with a rotated and cropped version of the image. Figure 73 illustrates the x-signature obtained from the rotated image.

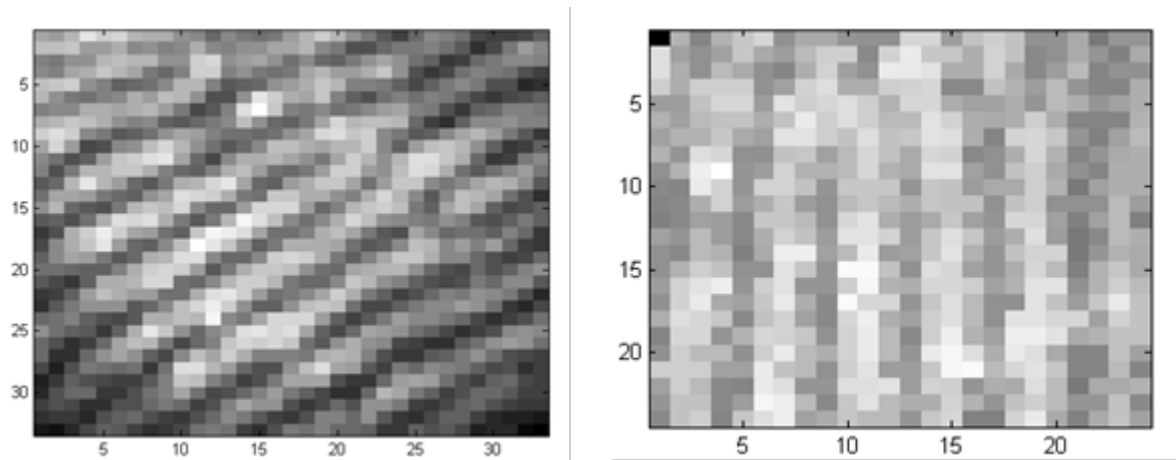


Figure 72: A small window of the original image (left) and its rotated, cropped version (right).

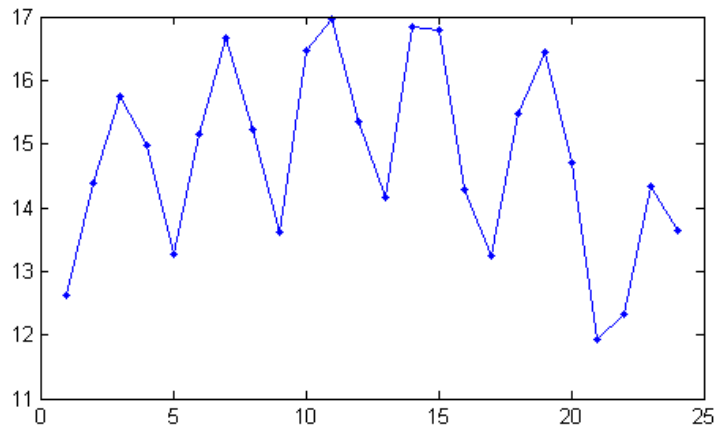


Figure 73: x-signature obtained from the rotated and cropped image from Figure 72

The local frequency is estimated by finding the average number of pixels (λ) between consecutive peaks in the x-signature, and calculating the reverse of it ($f=1/\lambda$). The final step of the enhancement process is applying the proper Gabor filter described in the following equation according to the estimated orientation θ and frequency (f). The standard deviation values δ_x, δ_y are chosen based on empirical data.

$$h(x, y, \theta, f) = \exp\left(\frac{1}{2}\left[\frac{x_\theta^2}{\delta_x^2} + \frac{y_\theta^2}{\delta_y^2}\right]\right) \cos(2\pi f x_\theta) \quad (29)$$

$$x_\theta = x \cos \theta + y \sin \theta \quad (30)$$

$$y_\theta = -x \sin \theta + y \cos \theta \quad (31)$$

Figure 74 shows an example of a processed fingerprint image along with the original image.

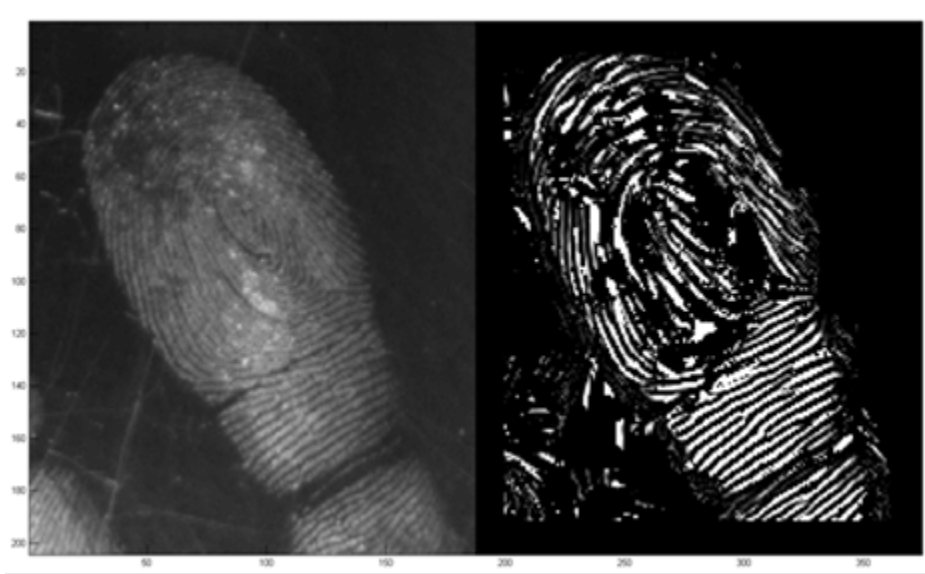


Figure 74: An example of a processed fingerprint image (right) and the original image (left).

IV.10. Polarization Analysis

While spectral measurements convey information about materials, polarization measurements reveal information about surface features, shape, shading, and roughness. Furthermore, polarization tends to provide information that is largely uncorrelated with spectral and intensity images, and thus has the potential to enhance the understanding of crime scenes. More specifically, Lin et al.[35] utilized differences in optical polarization and/or reflection to digitally enhance and lift latent fingerprints from smooth, pliable dielectric surfaces. In this section, we present a set of definitions and computations for polarimetric measurements applicable to the imaging and lifting of latent fingerprints and offer our assessment of the utility of polarization.

IV.10.1. Stokes Parameter Images

For our polarization analysis, images were taken with a linear polarizer mounted in front of the breadboard camera lens and oriented at four different angles: 0° , 45° , 90° , and 135° . At each polarizer position, the camera captured an image, acquiring a total of four polarization state images: I_0 , I_{45} , I_{90} , and I_{135} . To characterize polarimetric signatures, we calculated the Stokes parameters by combining the intensity values over all 1200×1600 pixels in the polarization state images as follows:

$$S_0 = \frac{1}{2}(I_0 + I_{45} + I_{90} + I_{135}) \quad (32)$$

$$S_1 = I_0 - I_{90} \quad (33)$$

$$S_2 = I_{45} - I_{135} \quad (34)$$

Where S_0 is the incident irradiance, S_1 describes horizontal polarization, and S_2 describes polarization at 45° to horizontal. Figure 76 illustrates the Stokes parameter images computed for the NIR-1 spectral image shown in Figure 75.



Figure 75: NIR-1 polarization state images of a fingerprint on a book cover: I_0 , I_{45} , I_{90} , and I_{135} .



Figure 76: Example of Stokes parameter images for the NIR-1 spectral image in Figure 75: S_0 (left), S_1 (middle), and S_2 (right).

IV.10.2. Contrast Enhancement via Virtual Polarizer

By varying the angle of light shining onto a surface, we can potentially locate latent fingerprints that are otherwise difficult to observe. Latent fingerprints generally consist of tiny ridges of skin residue that contain transparent dielectric materials such as sweat, grease, and lipids [35]. Since specularly reflected light from dielectrics is partially polarized at certain

viewing angles, we can exploit the optical properties of polarization to improve contrast between the fingerprint and its background thereby improving the detectability of latent prints.

The general expression for the observed intensity of partially polarized light I as a function of polarization orientation is defined as:

$$I(\theta) = I_0 \cos^2 \theta + (I_{45} - I_{135}) \sin \theta \cos \theta + I_{90} \sin^2 \theta , \quad (35)$$

where θ is the angle of orientation of the polarization analyzer and I_0 , I_{45} , I_{90} , and I_{135} are polarization state images [36]. With this polarization technique, we can extract purely specular reflection components from the surface to obtain a substantial contrast between the fingerprint residue pattern and the background surface in between.

Figure 77 shows the results obtained using our polarization enhancement technique. In this example, nine intensity images were formed using Equation 35 where θ was varied from 5° to 45° in increments of 5° . The resulting intensity images were then combined, using the image fusion method described in Section IV.8.2, to form the observed intensity image displayed in Figure 77. We generated nine intensity images, one for each angle 5° , 10° , ..., 45° then combined the intensity images via multi-scale image fusion. Adding angles greater than 45° did not appear to improve results – based on visual observations only. Notice the improved detail of the latent thumbprint in the intensity image generated from the polarized images (right) as compared to the non-polarized image (left). An enlarged region of the top most latent thumbprint of Figure 77 is shown in Figure 78. Notice how polarization makes the thumbprint ridges visible over the lettering.

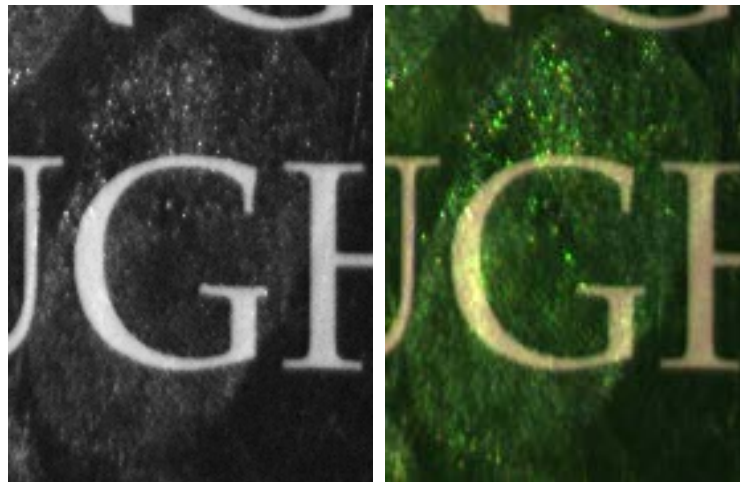


Figure 77: Contrast enhanced thumbprint on the cover of a textbook. The non-polarized image (left) has lower contrast for the fingerprint compared to the polarized image (right).



*Figure 78: Enlarged region of the top most thumbprint
Notice the improved detail of the ridge patterns in the polarized image (right) as compared to the non-polarized image (left).*

Further enhancements to the latent prints were obtained by fusing complementary wavelength images. Figure 79 shows the results of applying three channel false color to virtual polarization enhanced Red, Blue, and NIR-1 wavelength images. This example shows a false color RGB image of an enlarged region of the left most latent thumbprint shown in Figure 77. Notice the improved detail of the ridge patterns across the letter G in the enhanced Red-Blue-NIR-1 false color image (right) as compared to the virtual polarization enhanced NIR-1 image (left).



*Figure 79: False color image generated from virtual polarization enhanced Red, Blue, and NIR-1 wavelength images.
Enlarged region of the leftmost latent thumbprint: Left image is the virtual polarization enhanced NIR-1 image. Right image is the enhanced Red-Blue-NIR-1 false color image. Notice the improved detail of the ridge patterns across the letter G in the right image*

IV.10.3. Degree of Linear Polarization and Angle of Polarization

Two polarization features we investigated for forensic applications are the degree of linear polarization, DOLP, and the angle of polarization, AOP. DOLP is the fraction of the intensity attributable to linear polarized light states whereas AOP is the angle of the major axis of the polarization ellipse with respect to the x axis [37]. These measurements are mathematically defined in terms of the Stokes-vector elements as:

$$DOLP = \frac{\sqrt{S_1^2 + S_2^2}}{S_0} \quad (36)$$

and

$$AOP = \frac{1}{2} \tan^{-1} \left(\frac{S_2}{S_1} \right). \quad (37)$$

We selected these features due to their ability to predict object properties. DOLP yields information about the roughness and material composition of an object's surface while AOP describes the shape of an object's surface elements (facets) [38]. In addition, DOLP can enhance details in shadows [39]. Examples of DOLP and AOP are shown in Figure 80.



Figure 80: Degree of linear polarization and angle of polarization images. Here we show the DOLP (center) and AOP (right) images compared to the Stokes S_0 image (left). Notice the increased SNR and information provided by DOLP in the center image.

IV.11. Contextual Rank Ordering

Contextual rank ordering utilizes a combination of image quality metrics to prioritize images from most informative to least informative by measuring image characteristics such as edge

content, phase symmetry, and contrast. The assigned rank that is computed from the metrics can then be used as a qualitative measure to determine which individual spectral images (e.g., UV, blue, green, red, NIR-1, NIR-2) are displayed to the field analyst. Furthermore, the assigned ranks can be integrated into an automated image selection process for data analysis algorithms such as color opponent processing, three-channel false color processing, and various texture and spectral analysis algorithms. Finally, contextual rank ordering can also be applied to processed images for a prioritized presentation of results, i.e., processed images are ordered according to information content and then queued for the image analyst to review.

In the image processing community, there is no standard quantitative metric defined for measuring the quantity of improvement one enhancement algorithm offers over another. Numerous metrics have been published in the literature; however, there is no general consensus in the community as to which metric more accurately measures true enhancement. Furthermore, the consistency across different metrics varies depending on the exact characteristic being measured – one metric may rate Algorithm A high while another metric will rate it low. Based on this, we developed our contextual rank ordering process which is derived from several published metrics.

IV.11.1. Rank Order Metric

Five individual measures are combined to obtain an overall image quality measure: edge strength [40], corner strength [40], phase congruency [41], phase symmetry [41] and histogram spread [42]. This quality measure is then transformed to a rank order score via a nonlinear regression function which is averaged over the entire image to produce the final metric.

$$Q(x, y) = E_s(x, y) + C_s(x, y) + P_c(x, y) + P_s(x, y) + H_s(x, y) \quad (38)$$

$$R_s(\tau, x, y) = \frac{1}{2} - \frac{1}{1 + e^{\tau Q(x, y)}} \quad (39)$$

$$R_m = \frac{1}{MN} \sum_{y=1}^N \sum_{x=1}^M R_s(\tau, x, y) \quad (40)$$

Edges characterize the intensity discontinuity of an image. Corners are defined as points where slope changes abruptly. Phase congruency models patterns of order in the phase component of the image and is used as an illumination and contrast invariant measure. Phase symmetry indicates the invariance of objects under some geometrical transforms. Contrast can have a significant visual impact on an image by emphasizing texture.

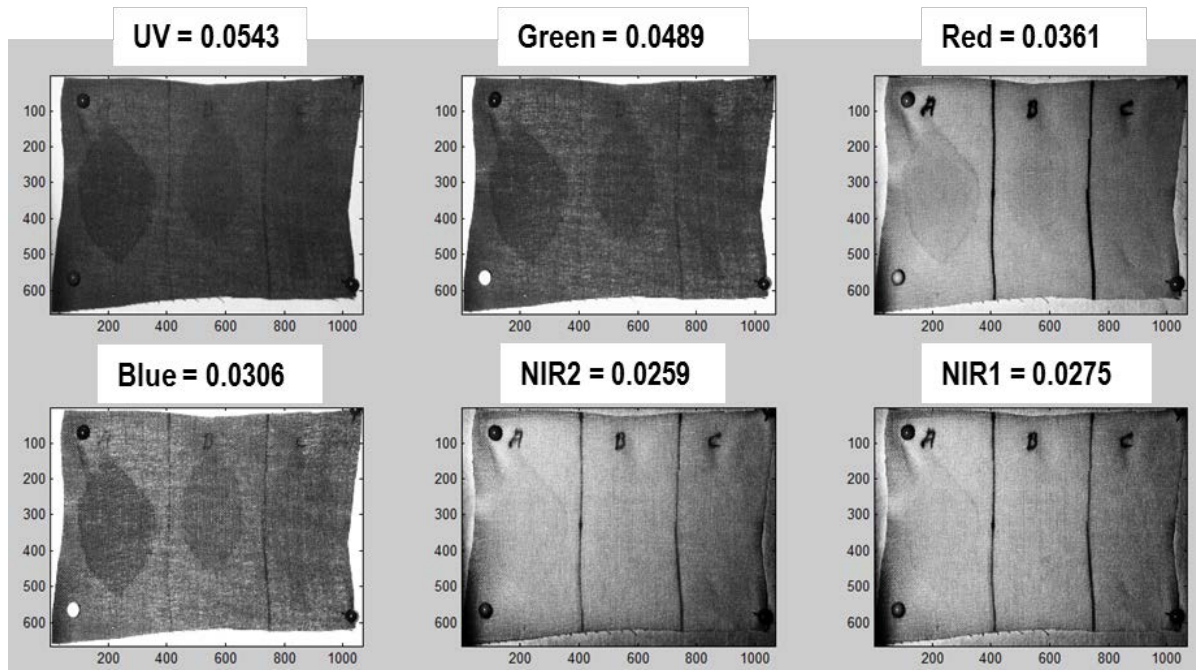


Figure 81: Edge, corner, symmetry quality measure for the blood stains on red cloth images Rank ordering algorithms can measure the information content of images and prioritize them for post processing and presentation to the viewer. A larger metric number indicates higher information content.

IV.12. A Note on Processing Platform Requirement

Our adaptive dynamic range compression (ADRC) algorithm has been successfully implemented on an FPGA and used in real-time enhancement of visible and MWIR images for image enhancement and fusion processes for surveillance applications. Although default parameter settings are provided, user adjustments are expected from time-to-time depending on temporal and environmental changes. Similarly, our color opponent processing algorithm has been successfully implemented on a real-time system for object classification applications.

We envision nearly real time operation (~1 second processing time after acquisition and not processing at video rate) which is quite feasible with modern FPGAs or board level computers.

V. LED Pulsed Illumination and Radiometric Considerations

The ability to operate in the presence of ambient lighting is a key goal for the proposed camera. In this section we describe the optical properties of the Commercial off-the-shelf (COTS) LED sources that we used in our experiments, to ascertain that a design based on these LEDs can provide sufficient light to contrast against ambient light in common lighting scenarios, such as inside an office and within a shadow under direct sun light.

We first list the manufacturer supplied specs of these LEDs for continuous operation; then present our measurement results by overdriving the operating currents in pulsed (strobe) mode; and finally compare the output power of the LEDs with typical ambient lighting.

V.1. Optical Characteristics as Specified by the Manufacture

Table 3 summarizes the manufacturer-supplied optical characteristics of the LED sources that we used in our experiments. Notice that the operation current, also referred to as 100% current, is rated for continuous operation of the LEDs.

Table 3 Optical characteristics of the LEDs

Peak Wavelength (nm)	374	467	473	517	629	736	860
Spectral Width(FWHM) (nm)	13	31	25	34	15	27	31
Operation Current (mA)	200	200	200	200	200	200	200
*Output Power Density (Wm^{-2})	11.8	9.55	30.5	11	38.2	17.8	20.3

* Measured at 250 mm from the front of the module into a 10 mm circular aperture at the center of the optical output.

V.2. Overdriving

In pulsed mode, the LED forward current can be driven to a much higher value than its rating, but only for short periods and at low duty cycles, so that the LED does not overheat and get damaged. The limit of this scheme depends on the material properties of the particular LED. A practical method to determine how high the current can be overdriven without affecting the LEDs adversely is to measure the output power as a function of the driving current. Typically the output power of the LED increases as the driving current increases and gradually levels off. It is in general safe to overdrive the LED before the level off point, beyond which most of the additional energy put in, is dissipated in the form of heat.

Figure 82 illustrates the setup we used to characterize the LEDs. A Gardasoft RT420 LED Lighting Controller is used to control the driving current and pulse width of the LEDs. A Thorlabs photo detector, equipped with a high speed Si PIN photodiode, converts the light output from the LED to electrical signal, and sends it to a Tektronix TDS 3034B digital Oscilloscope for measurement. The distance from the LED and the photo detector is kept constant for each LED, so that the measured value is proportional to the output optical power.

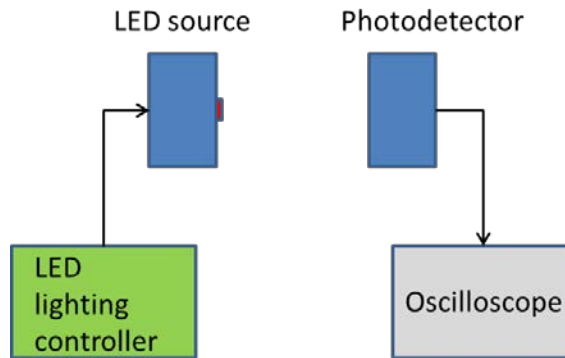


Figure 82 Schematic of the LED characterization measurement.

Figure 83 shows a typical waveform of a LED output in the pulse mode, where in this case the LED has a central wavelength of 629 nm, and is driven at the rated current with a pulse width of 1 ms. The near perfect square edges indicate that the response time of the LED is significantly faster than a millisecond.

Figure 84 shows the measured results for all the LEDs listed in Table 3, labeled by their central wavelength. For each LED, the relative output light intensity (normalized to the value at the rated current) is plotted against the relative driving current (with 100% being the rated current). Pulses of different widths are tested for comparison. The “linear” line indicates the output intensity if the LED would respond linearly with the driving current. As a precautionary measure to protect the LEDs, only for 1 ms pulse is the current overdriven to 1000% (10X), which is the reason why not all cases have data points for higher current values.

It’s evident that all the LEDs can emit pulsed light powers significantly higher than the rating by overdriving the current. The pulse width does not seem to affect the power response of the LEDs. The capability of overdriving varies between LEDs. Among the tested units, the red (630 nm) LED shows the least capability in terms of overdriving (~2.8X). The IR (740 nm and 870 nm) shows the greatest potential of overdriving, with no sign of leveling off even at 1000% driving current.

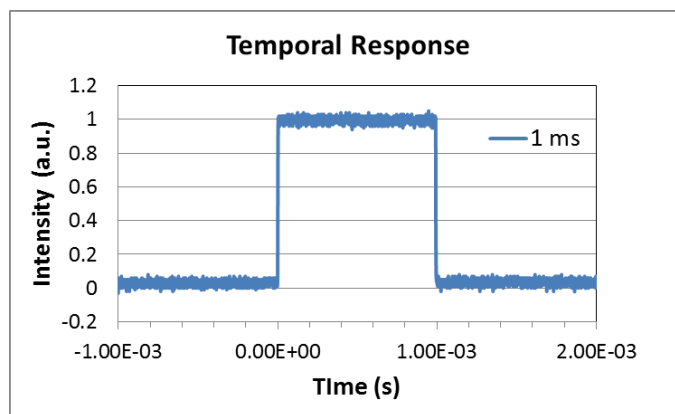


Figure 83 Typical waveform of a LED output pulse.

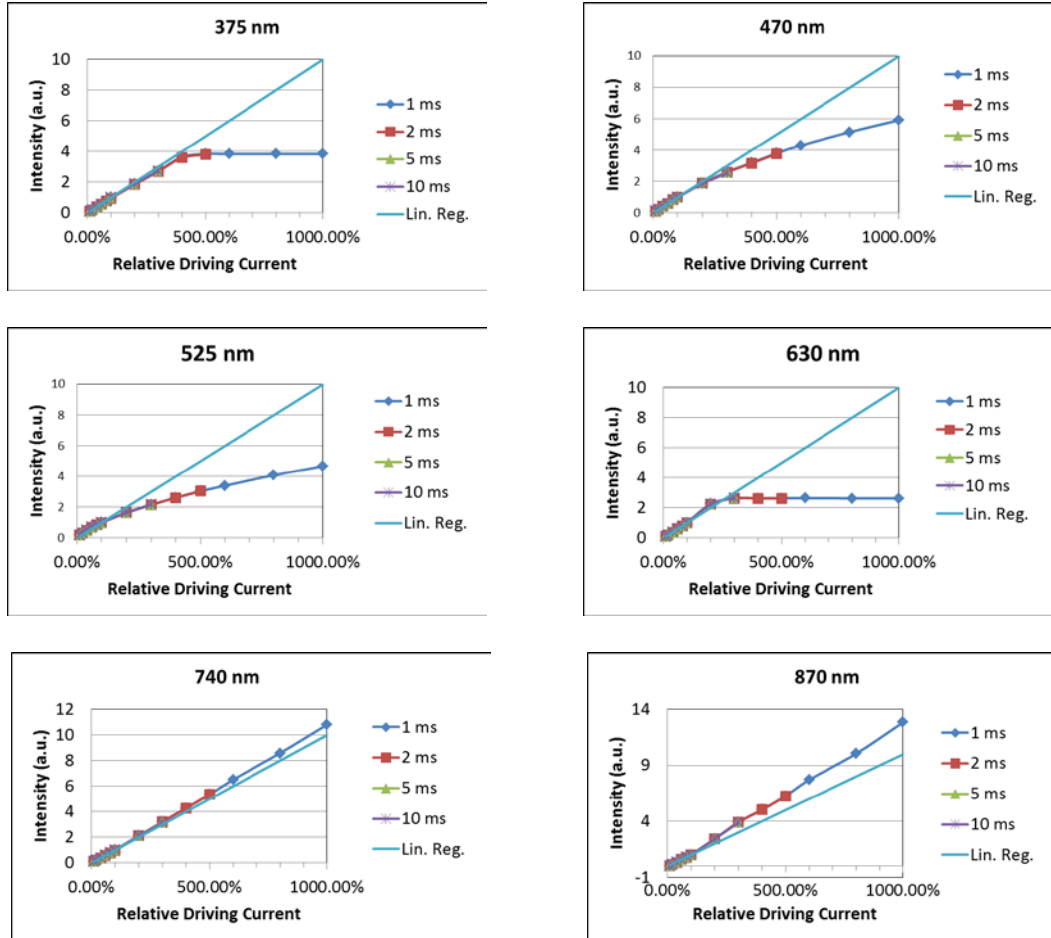


Figure 84 Output light intensity (normalized to level at the rated current), vs. driving current (relative to the rated (100%) current) for the LEDs
Pulses of different widths are tested for comparison. “Linear” indicates the output intensity if the LED responds linearly with the driving current.

To get the absolute power level the LEDs can output, we use the output power density data in Table 3 as reference and calibrate the measured overdriving data. The results are summarized in Table 4.

Table 4 Maximum output power obtained with current overdriving

Peak Wavelength (nm, nominal)	375	470	525	630	740	870
Spectral Width(FWHM) (nm)	13	31	34	15	27	31
Overdriving Current (%)	500	1000	1000	300	1000	1000
*Output Power Density (W/m ²)	44.84	57.3	52.8	106.96	195.8	263.9

*At 250 mm from the front of the module into a 10 mm circular aperture at the center of the optical output.

V.3. Typical Lighting Conditions

With a radiometer (International Light Technologies, ILT1700 SED033/F/W) we measured the irradiance level under several typical lighting conditions, as summarized in Table 5.

Table 5 Measured surface irradiance under typical lighting conditions

	Office with fluorescence lights on ceiling	Outdoor, facing the sun	Outdoor, within shadow under direct sun (winter afternoon)
Irradiance (W/m ²)	2-4	840	5-30

These measured values are the total power spread over the spectrum of the corresponding light sources. Figure 85 and Figure 86 show the standard solar spectra (namely, Air mass (AM) 1.5 global, AM1.5 direct, and AM0) and the spectrum of a typical fluorescence lamp, respectively.

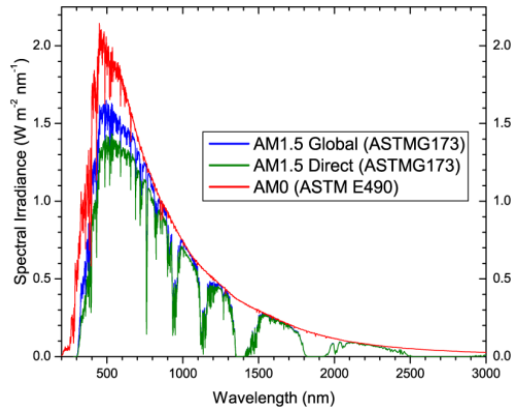


Figure 85 Standard solar irradiance spectra

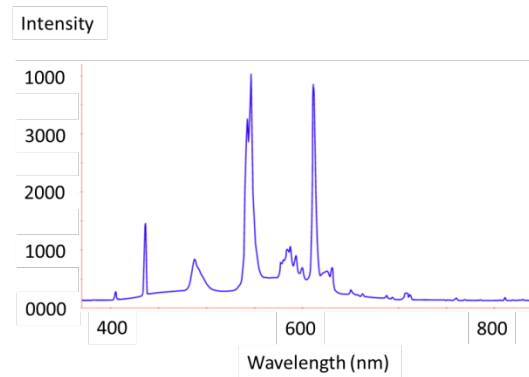


Figure 86 Spectrum of a fluorescence lamp

In our application, the image sensor collects light through a band pass filter. An ideal band pass filter would only transmit the wavelength within the pass band (in-band). In reality, some of the wavelengths outside of the pass band (out-of-band) also get transmitted due to non-zero transmittance in the blocking band. The physical sensor would not be able to distinguish whether the received light comes from in-band or out-of-band. Thus the received out-of-band light is the source of cross talk in a multispectral measurement. Even in-band light will make the system susceptible to variations in spectral characteristics of different ambient lighting. Two ways to suppress residual background influence are: 1) Higher power in band illumination, and 2) Capture a background image immediately before or after capturing an in-band image and subtract background from the in-band image.

The in-band and out-band power can be calculated given the light source's emission spectrum and the filter's transmission spectrum. Figure 88 shows the calculated results for those listed in Table 5. The transmission spectrums of the filters are provided by the manufacturer; for sunlight, the AM1.5 Global spectrum is used. The upper limits of the irradiance level in Table 5 are used where ever is applicable, so that the plotted out-band noise represent the worst scenario. Also shown for comparison are the irradiance levels from the LEDs at distances of 3m and 5m.

As shown in Figure 87, For an indoor florescence lamp, the LEDs power was at least two orders of magnitude higher than the out-band noise (except for the 740 nm filter, which will be discussed below). Outdoors, under shadow, the LEDs overpower the out-band noise by at least

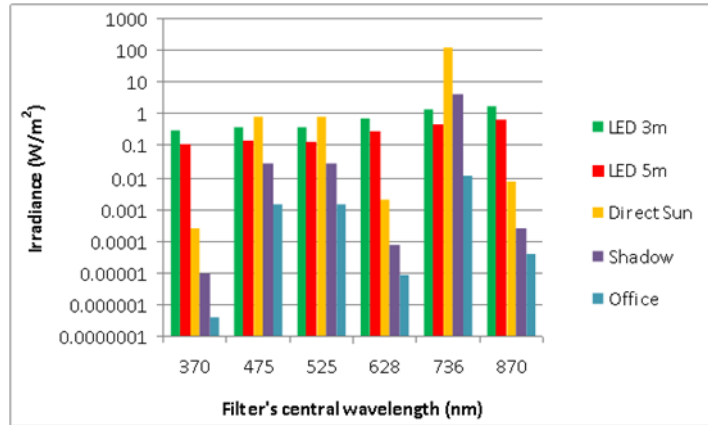


Figure 87 Comparison of radiance produced by LEDs at 3 m and 5 m with measured background strengths (logarithmic plot)

an order of magnitude (again except for the 740 nm filter). Facing direct sunlight, the LEDs provide less power than the out-band illumination for the 470 nm and 525 nm bands, but the levels are at the same order of magnitude. The 740 nm band was again an exception.

A review of the performance of the COTS 740 nm band pass filter (Figure 88) reveals that the filter did not provide sufficient attenuation over certain blocking bands, for example, around 400 nm. This explains why the 740 nm band in Figure 88 had exceptional high out-band noise. This can be avoided by using a filter having higher blocking band suppression.

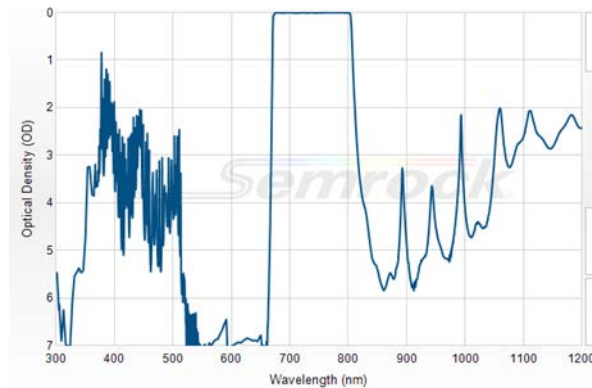


Figure 88 Transmission spectrum of the 740 nm band pass filter

There are a several ways to further improve the in-band to out-band ratio: 1. Multiple LEDs can be used together to increase the in-band light power; 2. the bandwidths of the filters can be tailored to the emission band width of the LEDs. The COTS filters we used in general had about twice the bandwidth than needed; 3. Filters of higher blocking band suppression can be used.

We believe that with a single LED per wavelength it is possible to produce illumination comparable to direct sunlight (within filter pass band) at 2 m, and in shadow, to well beyond 5 meters. Using multiple LEDs (particularly at blue and green wavelengths), custom filters, and by employing background subtraction, the effective range can be further extended. It should be noted that the actual performance limit is also influenced by the target reflectivity and the imaging mode, e.g. fluorescence mode will have shorter range than multispectral mode; for multi-spectral or polarization modes, at long ranges and with very low reflectivity targets, the read noise of the camera noise will limit the performance instead of background noise. It should also be noted that a makeshift shade is very easy to create and we do not expect that the camera will need to operate in direct sunlight, although in principle it should be able to do so at a limited range.

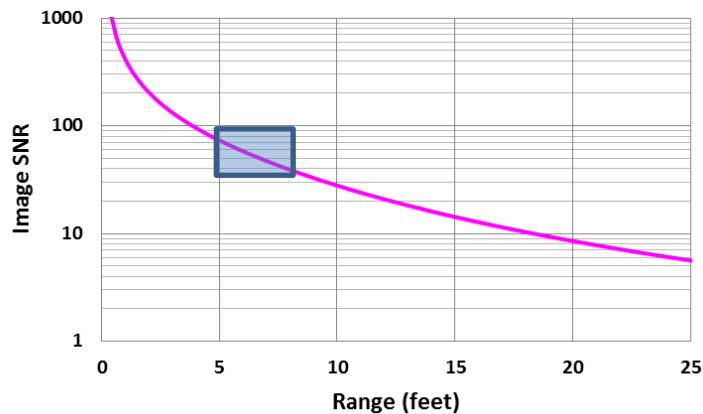


Figure 89 Calculated image SNR as a function of range for the proof of concept breadboard. We assumed indirect sunlit background and illuminator at 0.5X distance of the camera. A higher SNR is expected indoors. The bar shows the ranges used (indoors and outdoors) in this project. A custom illuminator design with multiple LEDs is expected to be ~18X brighter than the breadboard.

Figure 89 shows SNR calculations for the proof of concept breadboard. We typically placed illuminator at nearly half the distance from the target compared to the camera and that assumption was used. The shaded area shows the parameter space where the experiments were performed during this project. This geometry was used during the trade study to account for the large mismatch between the large FOV of the illuminator (50°) compared with a relatively narrow FOV of the camera (8.5°, set by COTS component choices). In a custom built system these FOVs will be better matched. A custom illuminator design with multiple LEDs is expected to be ~18X brighter than the breadboard to achieve high SNR at range >15 feet.

VI. Conclusions

The breadboard camera successfully collected a significantly greater amount of information than just the three color bands collected by a conventional digital camera. With its narrow, well defined, and multiple acquisition channels compared to color filters on the conventional camera, the breadboard camera was able to detect targets that were invisible to naked eye and in color digital camera images. In cases where the targets were visible but had little contrast to identify structural details and outlines, the breadboard camera (through software and hardware) was able to provide significantly higher contrast. The software enhancements were often subtle and generally related to fine detail. The effect of adaptive dynamic range compression and false color rendering to direct viewer's attention to high contrast features in images was substantial.

A majority of the experiments were performed indoors with ambient lighting where the background light levels were not particularly challenging. Two sets of experiments were performed outdoors to successfully push the illuminator to its limits and prove feasibility of outdoors operation. We used a radiometer to measure ambient light levels indoors as well as outdoors. The radiometric considerations convinced us that a combination of modern LEDs operating in pulsed mode along with spectral filters will be able to provide substantial operating range (15-25 feet) for most imaging modes even in an outdoors environment with a makeshift

shade to block direct sunlight. The camera can also operate in direct sunlight at shorter (~6 feet) ranges. Range is impacted by a wide range of target reflectivity encountered in the field. Fluorescence mode will have a shorter range than multispectral mode.

Looking beyond the current proof of concept, we need to focus on size, weight and power considerations for a field portable unit. An upgrade to a large (~12 MP) format camera is also a necessity based on subject matter expert feedback. Hardware improvements will likely also involve custom LED illumination optics, custom agile filter, and custom integrated hardware packaging. The testing so far has been in a controlled, clutter-free indoor/outdoor setting, and an extension of the trade study to more challenging field environment is required. More data with targets and backgrounds will also be useful. Another feedback was a desire to see a quantitative comparison with existing state of the art laboratory and field techniques and practices. Such a comparison should be possible with an upgraded custom hardware. Software user interface that maximizes the utility to the target end-user needs to be developed and tested.

The impact on the practice and policy of criminal justice, both at local and national level, has tremendous potential to be an overreaching one. The technology can answer the need for rapid crime scene scanning using multiple imaging modalities to identify targets of interest. Furthermore, it enables the first investigators on the scene to operate in ambient lighting. The technology can provide, in a small, rugged, affordable, and portable device some of the extensive capability currently available only in the laboratory. This will result in improved onsite presumptive analysis of forensic evidence at the crime scene. The advanced non labor-intensive capability to detect forensic evidence at a crime scene at a distance can also overcome scene hazards and prevent evidence contamination.

VII. Dissemination of Research Findings

The dissemination activities include a briefing at NIJ which was also attended by interested personnel from department of homeland security (DHS), and a teleconference (web based briefing) to Stockton police department. We participated in a panel presentation at 2012 NIJ conference and also presented a poster on the subject. We plan to present at a later date in a suitable conference meeting in the fields of optics/ optical engineering and forensic science.

VIII. References

1. G. Reis, "Photoshop CS3 for Forensics Professionals," Sybex 2007
2. J. Schneider, "Forensic imaging goes digital," Forensic magazine, Dec 2006 /Jan 2007
3. A. Lin, "Forensic Applications of Infrared Imaging for the Detection and Recording of Latent Evidence," Journal of Forensic Sciences, Vol. 52, 5, pp1148 (2007)
4. Product literature for FAL3000 Alternate Light Source Kit: <http://www.faurotforensics.com>
5. D. McGraw, "New LEDs Enable Innovations in Forensic Alternative Light Sources," Forensic magazine, Jun/Jul 2005
6. C. J. Guffey, "Laser Technology: Revolutionizing CSI Work," Forensic magazine, Oct/Nov 2007
7. Product literature for SceneScope Advanced RUVIS UV Imager: www.crimescope.com
8. S. Milutin, "Detection of Semen and Blood Stains Using Polilight as a Light Source," Forensic Science International, Vol. 51, p. 289 (1991)
9. N. Vandenberg, et al, "The Use of Polilight in the Detection of Seminal Fluid, Saliva, and Bloodstains and Comparison with Conventional Chemical-Based Screening Tests," Journal of Forensic Science JFSCA. Vol. 51, 2, pp 361 (2006)
10. Product literature for Crime-Lite 80L: www.fosterfreeman.com
11. S. Lin, et al, "Polarization- and Specular-Reflection-Based, Non-contact Latent Fingerprint Imaging and Lifting," Journal of the Optical Society of America A, Vol. 23, 9, pp. 2137 (2006)
12. Hecht E., Optics, Addison Wesley, fourth edition, p. 348.
13. Duncan C., Advanced Crime Scene Photography, CRC Press 2010
14. Aguilar, M., Grater, J., Tarquini, R. and Johnson, J., "Enhancement, Fusion, and Visualization of Third Generation FPA Imagery." In Proc. of the Meeting of the Military Sensing Symposia (MSS), Specialty Group on Passive Sensors. Orlando, Florida, 13-17 February 2006.
15. Ellias S.A. and Grossberg S., "Pattern Formation, Contrast Control, and Oscillations in the Short-Term Memory of Shunting On-Center Off-Surround Networks," Biol. Cybernetics 20(2), pp 69-98 (1975).
16. Rolls, E.T., and Deco, G., "Computational Neuroscience of Vision," Oxford University Press, pp. 61-65, 2002.
17. Diaz-Pernas, F., "A Dynamic Network Model of the Color Visual Pathways for Attentive Recognition," Neural Processing Letters, Vol. 7, pp. 27-36, 1998.
18. Lincoln, B., "Three-Channel False Color," Beneath the Waves, http://www.beneaththewaves.net/Photography/Three-Channel_False_Colour.html.
19. Lincoln, B., "Uses of Multispectral Photography," Beneath the Waves, http://www.beneaththewaves.net/Photography/Uses_of_Multispectral_Photography.html.

20. Lincoln, B., "Calculated Greyscale Images," Beneath the Waves, http://www.beneaththewaves.net/Photography/Calculated_Greyscale_Images.html.
21. Manolakis, D. and Shaw, G., "Detection Algorithms for Hyperspectral Imaging Applications," *IEEE Signal Processing Magazine*, 19, 29-43 (2002).
22. Jin, X., Paswaters, S., and Cline, H., "A Comparative Study of Target Detection Algorithms for Hyperspectral Imagery," *Proc. SPIE Vol. 7334*, 1-12 (2009).
23. Manolakis, D., Marden, D., and Shaw, G., "Hyperspectral Image Processing for Automatic Target Detection Applications," *Lincoln Laboratory Journal*, 14(1), 79 -116 (2003).
24. Broadwater, J., and Chellappa, R., "Hybrid Detectors for Subpixel Targets," *IEEE Trans. on Pattern Analysis and Machine Intelligence*, 29(11), 1891-1903 (2007).
25. Chang, C.I., Liu, J.M., Chieu, B.C., Wang, C.M., Lo, C.S., Chung, P.C., Ren, H., Yang, C.W., and Ma, D.J., "A Generalized Constrained Energy Minimization Approach to Subpixel Target Detection from Multispectral Imagery," *Optical Engineering* 39(5), 1275-1281 (2000).
26. Stein, D., Beaven S., Hoff, L., Winter, E., Schaum, A., and Stocker, A., "Anomaly Detection from Hyperspectral Imagery," *IEEE Signal Processing Magazine*, pp 58-69, January 2002.
27. Kruat, S., Scharf, L.L., and Butler, R.W., "The Adaptive Coherence Estimator: a Uniformly Most-Powerful-Invariant Adaptive Detection Statistic," *IEEE Trans. on Signal Processing*, 53(2), 427-438 (2005).
28. R. Wilson and M. Spann, *Image Segmentation and Uncertainty*. New York: Wiley, 1988.
29. C. Aldasoro and A. Bhalerao, "Volumetric Texture Segmentation by Discriminant Feature Selection and Multiresolution Classification," *IEEE Trans. on Medical Imaging*, 26(1), 1-14 (2007).
30. Freeman, W.T., and Adelson, E.H., "The Design and Use of Steerable Filters," *IEEE Trans. on PAMI*, 13(9), 891-906 (1991).
31. Simoncelli, E. and Freeman, W., "The Steerable Pyramid: A Flexible Architecture for Multi-scale Derivative Computation", *IEEE Proceedings of the 2nd International Conference on Image Processing*, Washington DC. Vol. III, pp. 444-447, October, 1995.
32. Burt, P. and Kolczynski, R.J., "Enhanced Image Capture Through Fusion", *IEEE Proceedings of the 4th International Conference on Computer Vision*, pp. 173-182, May, 1993.
33. Hong, L., Wan, Y. & Jain, "A Fingerprint Image Enhancement: Algorithm and Performance Evaluation," *IEEE Transactions on Pattern Analysis and Machine Intelligence* 20: 777-789 (1998).
34. A. Rao, "A Taxonomy for Texture Description and Identification," New York, NY: Springer-Verlag, 1990.
35. Lin, S., Yemelyano, K., Pugh, E., Jr., Engheta, Nader, "Polarizaiton- and Specular-Reflection-Based, Non-contact Latent Fingerprint Imaging and Lifting," *Journal of Optical Society of America*, 23(9), 2137-2153 (2006).
36. Schott, J., *Fundamentals of Polarimetric Remote Sensing*, SPIE Press, Bellingham, Washington, 2009.

37. Tyo, J. S., Goldstein, D.L., Chenault, D.B., and Shaw, J.A., "Review of Passive Imaging Polarimetry for Remote Sensing Applications," *Applied Optics*, 45(22), 5453-5469 (2006).
38. Howe, J.D., Miller M.A., Blumer, R.V., Petty, T.E., Stevens, M.A., Taelle, D.M., and Smith, M.H., "Polarization Sensing for Target Acquisition and Mine Detection," in *Polarization Analysis, Measurement and Remote Sensing III*, Proc. SPIE, Vol. 4133 (2000).
39. Duggin, M. J., "Imaging Polarimetry in scene element discrimination," in *Polarization: Measurement, Analysis, and Remote Sensing II*, Proc. SPIE, Vol. 3754, pp 108-117 (1999).
40. Cui, L., and Allan, A., "An Image Quality Metric Based on Corner, Edge, and Symmetry Maps," Proc. of BMCV, 2008.
41. Kovese, P., "Phase Congruency Detects Corners and Edges," Proc. Australian Pattern Recognition Society Conference: DICTA, 2003.
42. Tripathi, A., Mukhopadhyay, S., and Dhara, A., "Performance Metrics for Image Contrast," IEEE Proc. of ICIP 2011.